

Abstract

Ultracapacitors, also called electrochemical double layer capacitors (EDLC) or supercapacitors, may improve the performance of conventional electrolytic capacitors in terms of specific energy, or improve the performance of rechargeable batteries in terms of specific power when combined with respective device. However, the application of ultracapacitors faces the problem of ageing – the deterioration of capacity and increase of equivalent series resistance of the system.

This thesis intends to elucidate ageing mechanisms of ultracapacitors based on activated carbon electrodes with tetrafluoroborate in acetonitrile as electrolyte.

Multi-method experimental investigations are presented which allow to obtain a comprehensive picture of ageing. Ultracapacitors were electrochemically aged under various conditions by applying voltages and temperatures close to the actual operation conditions. The influences of ageing on the electrodes were investigated by structural and chemical characterization. Gas volumetric measurement (porosimetry) and Raman spectroscopy were applied to follow the structural changes; elemental analysis, electron spectroscopy for chemical analysis (ESCA, XPS) and attenuated total reflection infrared spectroscopy (ATR-IR) were applied for chemical composition analysis.

It was found that the changes of both structure and chemical composition, which occur on aged anodes and cathodes, are asymmetric. Aged anodes showed more significant changes such as stronger decrease of pore volume and specific area, and more complex chemical species. Chemically bound nitrogen species were found only on aged anodes, but not on fresh electrodes and aged cathodes.

Based on the experimental results, several mechanisms for ageing are suggested. The functionalities in activated carbons play an important role for ageing. Various oxygen-containing functional groups can take part in the reactions. A higher amount of functionalities means that more electroactive sites can be found on the graphene sheets in activated carbons to promote electrochemical reactions. Thus one can assume that less functional groups in activate carbons would be preferable for the stability of ultracapacitors.

II

Ageing tests were carried out on individual components of the electrodes, mainly on activated carbon powders and conductive carbon additives. Observations are consistent with those on assembled electrodes. It turned out that the activated carbons from synthetic resin precursors, which have fewer oxygen functional groups, suffer less from ageing than those from natural precursors with more oxygen functional groups. A similar phenomenon was also observed on the conductive agents.

Zusammenfassung

Elektrische Doppelschichtkondensatoren, auch Ultracapacitors oder Supercapacitors genannt, sind eine elektrochemische Energiequelle mit hoher spezifischer Energie und hoher spezifischer Leistung. Jedoch steht die Anwendung von elektrischen Doppelschichtkondensatoren vor dem Problem der Alterung - die Verschlechterung der Kapazität und die Zunahme des gleichwertigen Reihenwiderstandes des Systems im Verlauf der Zeit.

Diese Doktorarbeit beabsichtigt die Alterungsmechanismen der elektrischen Doppelschichtkondensatoren mit Aktivkohlenelektroden und Tetrafluorborat im Acetonitril als Elektrolyt aufzuklären.

Es werden experimentelle Untersuchungen unter Verwendung verschiedener Methoden vorgestellt, die einen umfassenden Einblick der Änderungen durch Alterung geben. Elektrische Doppelschichtkondensatoren wurden unter verschiedenen Spannungen und Temperaturen, vergleichbar mit tatsächlichem Betrieb, gealtert. Die Einflüsse von der Alterung auf die Elektroden wurden durch strukturelle und chemische Charakterisierung erforscht. Die volumetrische Gasmessung (Porosimetrie) und die Ramanspektroskopie wurden verwendet um die Strukturveränderungen zu bestimmen; die Elementanalyse, die Elektronenspektroskopie für chemische Analyse (ESCA, XPS) und die verminderte Gesamtreflexioninfrarotspektroskopie (ATR-IR) wurden verwendet um die Änderungen der chemischen Komposition durch Alterung zur charakterisieren.

Es wurde heraus gefunden, dass die Änderungen der Struktur und der chemischen Komposition auf den gealterten Anoden und den gealterten Kathoden asymmetrisch sind. Gealterte Anoden zeigten bedeutendere Änderungen wie stärkere Abnahme des Porenvolumens und der spezifischen Oberfläche, und der komplizierteren chemischen Spezies. Stickstoff wurde nur auf gealterten Anoden, aber nicht auf neuen Elektroden und gealterten Kathoden, gefunden.

Aufbauend auf diesen experimentellen Resultaten konnte einige Mechanismen für die Alterung vorgeschlagen werden. Die Funktionalitäten in Aktivkohle spielen eine wichtige Rolle für die Alterung. Verschiedene Sauerstofffunktionsgruppen können an den Reaktionen teilnehmen. Eine grössere Anzahl Sauerstofffunktionsgruppen bedeutet, dass mehr electroaktive Teile in Aktivkohle gefunden werden können, um

IV

elektrochemische Reaktionen zu foerdern. Man kann annehmen, dass weniger Sauerstofffunktionsgruppen für die Stabilität von elektrischen Doppelschichtkondensatoren vorzuziehend sein würden.

Alterungsuntersuchungen wurden auf einzelnen Bestandteilen der Elektroden, hauptsächlich auf der Aktivkohlenstoffpulver und der leitenden Kohlenstoffzusätzen durchgeführt. Beobachtungen sind mit denen auf zusammengebauten Elektroden konsistent. Die Aktivkohle aus Kunstharz mit weniger Funktionalitäten zeigt bessere Stabilität gegen die Alterung als die aus natürlichen Precursors mit mehr Sauerstofffunktionsgruppen. Ein ähnliches Phänomen wurde auch bei leitenden Kohlenstoffzusätzen beobachtet.

CONTENTS

Abstract	I
Zusammenfassung	III
Chapter 1 Introduction	1
1.1 Ultracapacitors working on double layer capacitance.....	2
1.2 Ultracapacitors working on “Pseudocapitance”	3
1.3 Asymmetric ultracapacitors.....	4
1.4 Goals and structure of the thesis	4
Chapter 2 Background	7
2.1 Construction of ultracapacitors	7
2.2 Materials for ultracapacitor electrodes.....	10
2.2.1 Graphite	11
2.2.2 Activated carbons.....	12
2.2.3 Carbon blacks.....	15
2.2.4 Porosity in carbon.....	16
2.2.5 Interfacial chemistry and electrochemistry of carbon surfaces.....	20
2.3 Electrolyte	24
2.3.1 Aqueous media.....	26
2.3.2 Nonaqueous media	27
2.4 Current collector – aluminium foil.....	30
2.5 Binder.....	32
Chapter 3 Methods	33
3.1 Structural characterization.....	33
3.1.1 Gas volumetric porosimetry	33
3.1.2 Raman spectroscopy.....	39
3.2 Chemical Analysis.....	43
3.2.1 X-ray photoelectron spectroscopy (XPS).....	43
3.2.2 Fourier Transformed Infrared(FTIR)	48
3.2.3 Elemental Analysis.....	53
Chapter 4 Experimental details	55
4.1 Sample preparation.....	55
4.1.1 Ageing of ultracapacitors	55
4.1.2 Ageing of components for ultracapacitors	56
4.2 Structural characterization.....	58
4.2.1 Porosimetry	58
4.2.2 Raman spectroscopy.....	59
4.3 Chemical composition characterization	60
4.3.1 Elemental analysis.....	60

4.3.2 Infrared analysis	60
4.3.3 XPS analysis.....	61
Chapter 5 Influences of ageing conditions	63
Chapter 6 Ageing effects on the electrodes of ultracapacitors.....	67
6.1 Microstructural changes of electrodes.....	67
6.1.1 Pore structure changes – porosimetry	67
6.1.2 Microcrystallinity changes – Raman spectroscopy.....	74
6.1.3 Summary	82
6.2 Chemical composition changes of electrodes	83
6.2.1 Elemental analysis.....	87
6.2.2 X-ray photoelectron spectroscopy (XPS).....	88
6.2.3 Attenuated total reflection Fourier transform infrared (ATR-FTIR)	96
6.2.4 Summary	104
Chapter 7 Ageing mechanisms of the ultracapacitors	105
7.1 Anodic reactions.....	106
7.2 Cathodic reactions.....	114
7.3 Non-electrochemical reactions.....	118
7.4 Summary	121
Chapter 8 Ageing effects on individual components of electrodes of ultracapacitors.....	123
8.1 Ageing effect on the activated carbons	123
8.1.1 Microstructural changes	124
8.1.2 Chemical composition changes.....	131
8.2 Ageing effect on the conductive agents	141
8.2.1 Microstructural changes	141
8.2.2 Chemical composition changes.....	143
8.2.3 Summary	145
Chapter 9 Conclusions and perspectives.....	147
References	151
Appendix	165

Chapter 1

Introduction

In the last two decades, the predictable depletion of fossil fuels and the environmental impact have driven people to develop low-cost and more environmentally friendly energy conversion and storage systems. Among many options electrochemical power sources have attracted acute attention and have been widely applied. Electrochemical power sources can be found from portable electronics to large electric vehicles (EV), such as rechargeable batteries (lithium ion battery, nickel-metal hydride battery and advanced lead acid battery), fuel cells and electrolytic capacitors.

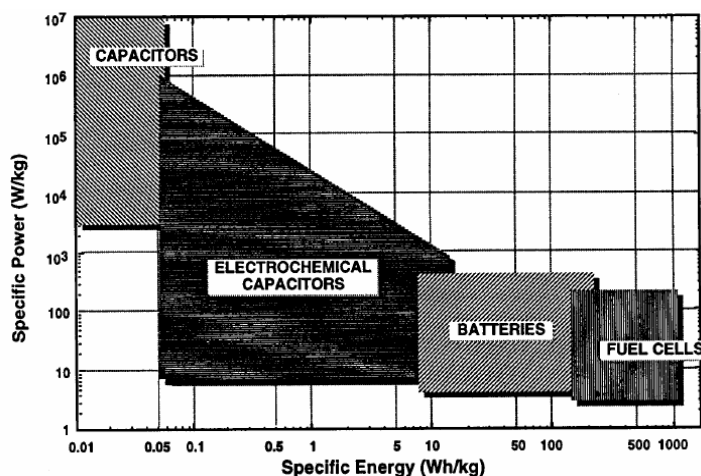


Figure 1.1 Ragone plot for energy-related electrochemical systems [Koetz00]

Specific energy and specific power are two figures of merit to evaluate the properties of these systems. High specific energy means to store a maximum amount of energy in minimal weight or volume and high specific power means to fulfill the output in very short time. Fuel cells and rechargeable batteries are typical power devices with high specific energy but poor specific power and conventional electrolytic capacitors stand on the other end to have high specific power with poor specific energy. Although some progress has been made in lithium ion battery field which improved the situation from one end slightly, there is still a big gap. This is suggested to be bridged by electrochemical capacitors (also called ultracapacitors or supercapacitors) (see Fig. 1.1).

Ultracapacitors may improve the performance of the electrolytic capacitor in terms of specific energy or improve the performance of the rechargeable batteries in terms of

specific power when combined with the respective device. In addition, ultracapacitors have a much longer cycle life than batteries because no or negligibly small chemical charge transfer reactions are involved. With these properties, they are of key importance in supporting the voltage of a system during increased loads for a lot of devices from portable equipment to hybrid electric vehicles (HEV), such as passenger cars, buses and locomotives. Their power assistance supports engine starting and acceleration. Due to their high power density for charging as well as discharging they are suitable for regenerative braking, which means to recuperate the redundant energy during slowing down and braking. In electronic devices such as cellular phones, camcorders, and navigation devices, ultracapacitors can also be found for low drain-rate memory, microprocessor and real time clock backup. [Conway99, Kötzt00]. Three types of ultracapacitors working on different principles have been developed and applied.

1.1 Ultracapacitors working on double layer capacitance

This is the most widely applied type of ultracapacitor. It works on the principle that electrostatic charges are stored in the electrochemical double layer (Helmholtz layer) formed at a solid/electrolyte interface.

When the capacitor is charged, charge excess and depletion will be formed on two ends, positive and negative ionic charges within the electrolyte separate and migrate towards two ends to compensate for this. In this case, two double layers are formed and charges are stored there. The capacitance is calculated according the formula

$$C = \frac{Q}{V} \quad (1.1)$$

The correspondingly stored energy will be

$$E = \frac{1}{2} QV = \frac{1}{2} CV^2 \quad (1.2)$$

Hence, capacitance and working voltage are two essential factors to improve the energy storage capability. For a smooth electrode in concentrated electrolyte solution, capacitance can be estimated according to equation

$$C = \frac{A \times \epsilon_0 \times \epsilon_r}{d} \quad (1.3)$$

where, A is the area of electrode, ϵ_0 is vacuum permittivity, ϵ_r is relative dielectric constant and d is the thickness of the double-layer. The thickness of the double layer

is always in the range of several angstroms, so the most effective way to increase the capacitance is to enlarge the electrode area.

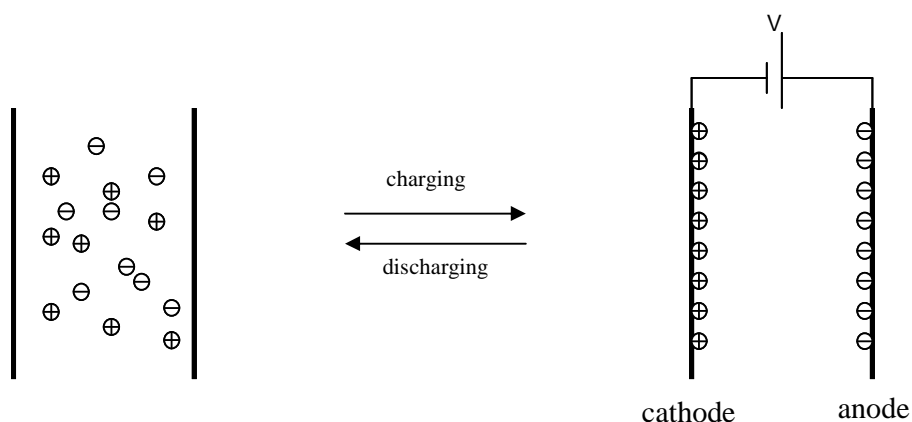


Figure 1.2 Working principle of a single-cell double layer capacitor

As shown in Fig. 1.2, the definition of the electrodes in the present work is according to the charging state.

A lot of work has been done to develop large area electrodes for ultracapacitors, using for instance, activated carbons, carbon felts, glassy carbons and carbon aerogels, etc. However, a large area should never be the only standard for estimating this kind of electrodes. The availability of the area, the structural and chemical stabilities and the cost are also very important. A good combination of these has to be found in practice.

1.2 Ultracapacitors working on “Pseudocapacitance”

Pseudocapacitance arises in some electrosorption processes and in redox reactions at an electrode. In this system, the materials give accessibility to protons and electrons that are involved in several overlapping redox processes. This effect is Faradaic in origin, involving the passage of charge across the double layer, as in battery charging or discharging, but capacitance arises on account of the special relation that originates from thermodynamic reasons between the extent of charge acceptance (Δq) and the change of potential (ΔV), thereby a derivative $d(\Delta q)/d(\Delta V)$ or dq/dV , which is equivalent to a capacitance, can be formulated. Pseudocapacitance is usually coupled with an appreciable double-layer capacitance component.

Two principal types of materials for this category have been discovered and studied,; one is electroactive oxides or hydrous oxide films of transition metals, e.g. RuO_2 , IrO_2 , Co_3O_4 , MoO_3 [Conway99]; the other is electrogenerated or chemically formed,

redox-active films of conductive polymers such as polyaniline, polypyrrole, and polythiophene, and various derivatives thereof [Gottesfeld91, Gottesfeld87, Rudge94, Rudge94, Conway 90]. RuO₂ out of the first type has been commercialized, but due to the high cost of Ru metal as the raw material, the application is limited to the military field. Conductive polymers are not commercialized yet for the limitation of long-term cycling stability.

1.3 Asymmetric ultracapacitors

Based on the working principles introduced above, asymmetric ultracapacitors have been developed and put into application a long time ago. It combines one electrode working on electrostatic energy storage and the other working on the Faradaic process. Normally activated carbons are used as the cathode and Ni(OOH) or conductive polymers as the anode. Through the structural tailoring of anode materials, the shortage of power output from Faradaic process can be remedied and high energy density and power density can be realized at the same time [Nelson05, Ganesh05]. The application of this kind of ultracapacitors is mainly limited due to the cost.

1.4 Goals and structure of the thesis

Among the above introduced types of ultracapacitors, the first type of ultracapacitors with porous carbon electrode is most widely applied for the sake of cost advantage, durability and stability. However, even though this system works on the basis of electrostatic charge storage, this system normally holds 5-10% contribution from pseudocapacitance. Since the structure and surface characteristics of porous carbon materials are complicated, the processes involved were not fully elucidated so far. Under critical conditions, like high temperature, overcharge and overdischarge, some irreversible electrochemical process might happen and result in ageing processes, such as capacitance loss and performance deterioration. This will obviously influence the performance and long term stability of the system. It is meaningful to figure out the ageing mechanisms for the further improvement and development of ultracapacitors.

This thesis focuses on the clarification of the mechanisms which induce the ageing of ultracapacitors with porous carbon electrodes. A multi-method research has been carried out for this purpose.

To give a clearer idea of our work, more background knowledge is given in chapter 2, where the construction of ultracapacitors, the materials used in ultracapacitors, the definition of ageing, and primary analysis of ageing are described.

In chapter 3, the methods applied for characterization are introduced, as well as the experimental details. Raman spectroscopy and porosimetry are applied for structural characterization. Electron spectroscopy for chemical analysis (ESCA), Fourier transformed infrared (FTIR) and CHN (carbon, hydrogen and nitrogen) elemental analysis are applied for chemical characterization. The working principles and operations for these methods will be explained. More experimental details can be found in chapter 4.

The influences of ageing conditions including temperature and voltage are briefly discussed in Chapter 5.

Chapter 6 gives the results of integrated electrodes from assembled ultracapacitors from various methods, and a thorough analysis as well as discussion. In this case, the integrated electrode means it contains several components such as activated carbons, conductive agents and binders, e.g. fluoropolymers, adhering to an aluminium current collector. Asymmetric structural and chemical changes have been found on the anode and cathode.

Based on the results from Chapter 6, ageing mechanisms on the anode and cathode are discussed in Chapter 7.

To further clarify the ageing influences on the individual components of the electrodes, in contrast to the integrated electrodes studied in Chapter 6, various activated carbons, conductive agents are chemically and electrochemically aged and characterized separately. Results and discussions can be found in Chapter 8.

A brief summary of the present work and suggestions for the improvement of the properties of the ultracapacitors from the point of anti-ageing are given at the end.

Chapter 2

Background

2.1 Construction of ultracapacitors

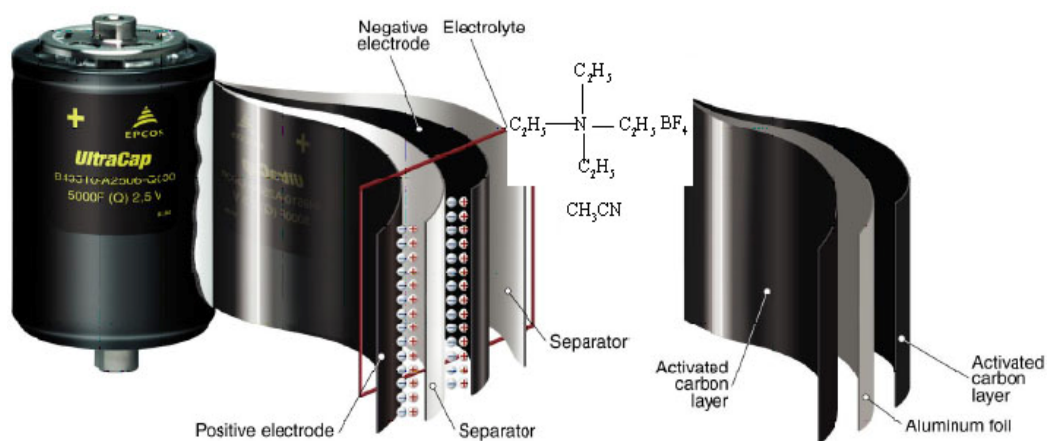


Figure 2.1. Construction of ultracapacitors

As shown in Fig. 2.1, ultracapacitors are composed of two electrodes, anode (positive electrode) and cathode (negative electrode) to store electric energy. An isolating porous separator is inserted between the electrodes in order to prevent a short circuit, while the ions are allowed to permeate through. The electrolyte is ion-conducting to supply the ions to form capacitance on the interface between the electrode and electrolyte as introduced in Chapter 1, for example, a solution of tetraethylammonium tetrafluoroborate (TEATFB) in acetonitrile (ACN) (see Fig. 2.1).

The electrode for ultracapacitors normally contains several ingredients with different functions – active ingredients such as activated carbon to offer high specific area for the capacitance, conductive agents such as carbon black and graphite to improve the conductivity between the activated carbon grains. In order to improve the packing density to achieve higher capacitance and higher conductivity, activated carbon and conductive agents are kept integrated as a layer by binders which are typically fluoropolymers (polyethylene, carboxymethylcellulose and other water soluble binders can also be applied). Mixing processes are typically blending or slurry dispersion. This layer then firmly adheres to a current collector, which is normally a metal foil to input and output the current.

What is ageing?

Ageing means the performance deterioration, which for ultracapacitors is the decrease of capacitance and increase of equivalent series resistance (ESR) with time.

The definition of capacitance has been given in Chapter 1. A simplified simulated circuit for the ultracapacitor system is shown in Fig. 2.2, which includes the double layer capacitances C_1 and C_2 formed on the interface of the electrode and electrolyte, the equivalent series resistance (ESR) composed of (1) the contact resistance between particles of electrode materials, (2) the contact resistance between the current collector and electrode material, (3) the electrolyte resistance and (4) the contact resistance between the terminal to the current collector. R_p in the circuit represents the parallel resistance, which may be from ohmic leakage pathways between the two electrodes of a charged capacitor or from some leakage processes, corresponding to Faradaic, potential-dependent charge transfer reactions.

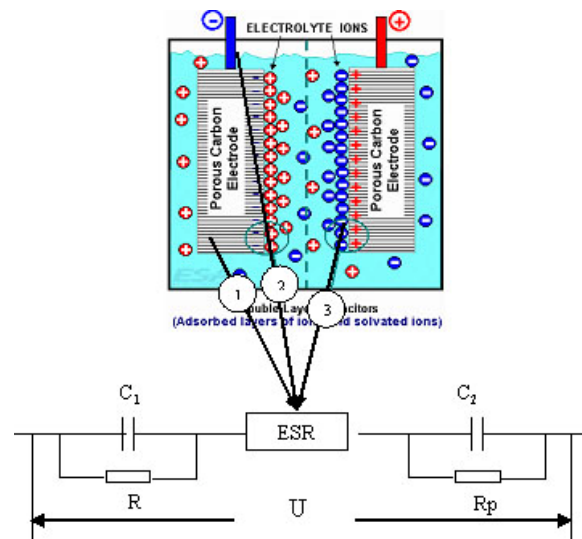


Figure 2.2 Simulated circuit for double layer ultracapacitors

To avoid a misunderstanding due to the oversimplification in the Fig 2.2, two points have to be noted here: first, the situation for porous electrodes is much more complicated than what is shown here, a distributed RC network should be included in the equivalent circuit according to transmission-line model, which is out of the focus of the present work; second, in a real system there is no dripping electrolyte, two electrodes are separated only by the separator which means the distance is in micrometer range.

Although electric double layer capacitors work on the principle of electrostatic charge storage, there are always some electrochemical processes involved, which normally

contribute 5 to 10 percent to the whole capacitance, most of these reactions are usually reversible. When the capacitors are utilized under critical conditions such as high temperature and/or high voltage, irreversible reactions might occur such as by-product deposition on the electrode surfaces and gas evolution. These have various influences: First, the active element in the system is irreversibly consumed; second, gas evolution and accumulation in closed systems increase the internal pressure, which in extreme cases causes structural destruction of ultracapacitors; finally, all these effects will change the structural and chemical characteristics of the electrodes, which in turn influence capacitance and equivalent series resistance.

Ageing is a comprehensive effect and may be caused by all the components of the system. Therefore to understand this calls for a multi-method investigation.

Asymmetric polarization on the anode and cathode of ultracapacitors

Apart from the definitions introduced above, it is worthwhile to mention here the asymmetric polarization of the ultracapacitors based on porous carbon materials to give an idea of the potential range where the present work is carried out.

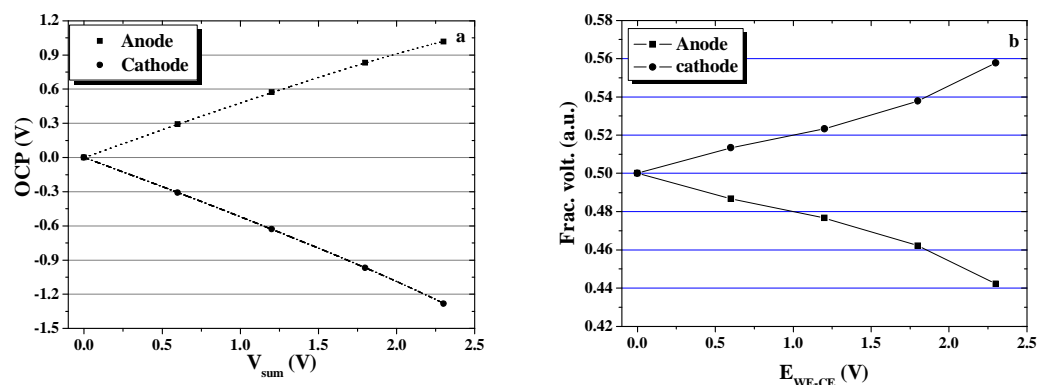


Figure 2.3 Asymmetric polarization of ultracapacitors, a. Dependence of V_{an} and V_{ca} on V_{sum} , b. Fractional V_{an} and V_{ca} with V_{sum}

In the usual ultracapacitors, symmetric design is adopted. However, results from the three electrode setup indicate that there is an asymmetric polarization on the anode and cathode, as shown in Fig. 2.3. [Siemens01, Yang05] Where, the open circuit potential (OCP) between the anode and reference electrode (RE, Ag/Ag^+) is denoted as V_{an} , and that between cathode and RE as V_{ca} and the sum voltage V_{sum} (or V_{WE-CE}) between working and counter electrodes is the sum of V_{an} and V_{ca} , i.e., $V_{sum} = |V_{an}| + |V_{ca}|$. According to Fig. 2.3a, both of V_{an} and V_{ca} on V_{sum} increase linearly with the increase of V_{sum} . The linearity implies that it is quite close to an ideal capacitor with

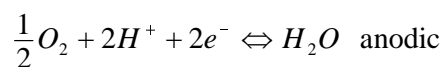
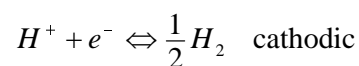
negligible Faradaic reactions. After V_{sum} reaches 2 V, a deviation from the linearity is observed, which can be correlated to the onset of some electrochemical reactions. In Fig. 2.3b, the ratio of V_{an} and V_{ca} versus V_{sum} is shown. It is clearly seen that $R_{V_{\text{an}}}$ and $R_{V_{\text{ca}}}$ meet each other only at the $V_{\text{sum}}=0$ V, and then run separately in inverse direction. $R_{V_{\text{an}}}$ decreases gradually and reaches 0.44 at $V_{\text{sum}}=2.3$ V, whereas $R_{V_{\text{ca}}}$ increases and reaches 0.56.

2.2 Materials for ultracapacitor electrodes

As mentioned before, materials for double layer ultracapacitors should have high area available to form as high a capacitance as possible. In addition, they should have high electrochemical stability.

Carbon is an element almost uniquely suited for fabrication of the double layer ultracapacitors. Carbon has the ability to bond to itself (catenation) via sp^3 (diamond-like) and sp^2 (graphite-like) hybridization. The sp^2 hybrid has three outer electrons in three equivalent bonding orbitals respectively, which are directed in a plane at 120° to each other. The fourth electron in the third p-orbital is capable of forming π -bonds with neighbouring atoms. Because of these variations, it exists in several well-known allotropic forms —diamond, fullerenes, graphite, amorphous carbon, and carbon nanotubes. Among these, graphite and amorphous carbon such as activated carbon and carbon black have already been widely applied for electrochemical systems.

From the electrochemical point of view, carbon is relatively stable and has a potential voltage range of almost ideal polarizability approaching 1.2V in aqueous solution limited by the potential difference between the cathodic and anodic decomposition reaction as shown below, and possibly up to 3.5V in non-aqueous media. [Conway99]



Solid carbons are taken to consist mainly of carbon atoms grouped into layers of fused aromatic rings exhibiting a certain degree of planarity (or two-dimensional order). This planarity can be extended from a few rings (as in non-graphitizable carbons) to thousands of them (as in graphitizable carbons). In either case, the individual layers are likely to contain imperfections (e.g., twists, non-aromatic links, and carbon

vacancies), in spite of which they tend to stack more or less on top of each other, and are held in position by weak van der Waals forces (ca. 13.2 kJ/C atom [Krevelen81], versus >288 kJ/C atom for carbon-carbon bonds). Heating to temperatures higher than 2500 °C in non-reactive environments may (for graphitizable carbons) or may not (for non-graphitizable ones) smooth the imperfections and improve the stacking order, so as to make the structure of the material resemble that of graphite more or less. According to this ability, carbons can be classified into graphitizable and non-graphitizable. The so-called “graphitizable” carbons tend to be soft and non-porous, with relatively high densities, and can be readily transformed into crystalline graphite by heating at temperatures in the range 2200-3000 °C. In contrast, “non-graphitizable” carbons are hard, low density materials which cannot be transformed into crystalline graphite even at temperatures of 3000 °C and above. The low density of non-graphitizable carbons is a consequence of a microporous structure as introduced later, which gives these materials an exceptionally high internal surface area. These structural arrangements are responsible for remarkable chemical, electronic and electrical properties of carbons. [Kinoshita88, Bansel88, Donnet76]

In the present study, activated carbon is utilized as active ingredient to form capacitance, other carbonaceous materials like carbon black and graphite are applied as current conductive agents to improve the conductivity of the electrode. Hereinafter we give a brief introduction of structural, physical and chemical properties of these materials. To facilitate the discussion, we start from graphite and then take this as the basis for other carbon materials.

2.2.1 Graphite

From the point of crystallographic structure, the ideal graphite structure consists of layers of carbon atoms arranged in hexagonal rings that are stacked in a sequence ABAB... This form of graphite is called hexagonal graphite. The graphite structure with the stacking sequence ABCABC... is called rhombohedral graphite, which is less stable and less prevalent than hexagonal graphite. The carbon-carbon bond length is 0.142 nm in the hexagonal rings and 0.335 nm in the direction of the c axis, which is perpendicular to the rings. The layer planes are composed of a hexagonal array of carbon atoms held by stable covalent bonds, but with weak van der Waals bonds between the layers. Because of the anisotropic structure of graphite, anisotropic properties are to be expected. Metallic properties are exhibited in the direction parallel

to the layer planes, while semiconducting properties are exhibited in the perpendicular direction. The electrical resistivity is about $10^{-2} \Omega \cdot \text{cm}$ in the direction of the c axis and $10^{-4} \Omega \cdot \text{cm}$ in the direction parallel to the hexagonal carbon planes. The high conductivity of graphite and its good chemical stability are attractive features for its use in electrochemistry. Graphite is widely applied in lithium ion batteries as an electrode for various electrochemical processes.

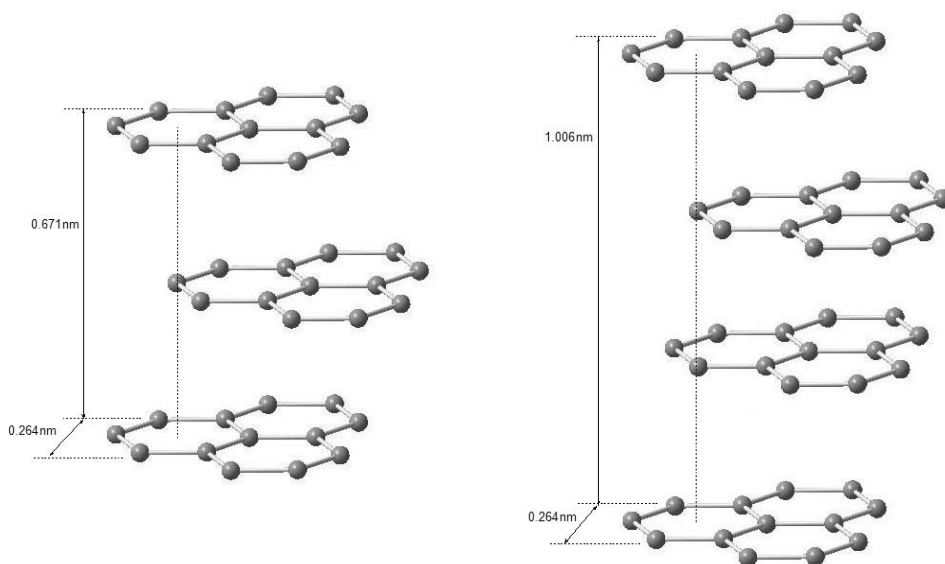


Figure 2.4 Crystal structure of graphite

Graphite occurs naturally in the earth's crust, however, the ash content of natural graphites is generally quite high (5 to 20%) thereby natural graphites are not used much in electrochemical systems. Of greater importance for electrochemical applications is artificial graphite, which is produced from different precursors (e.g., petroleum coke, pitch coke, and carbon blacks) by a variety of methods.

2.2.2 Activated carbons

Activated carbons normally have a porous structure and very high specific areas from 1000 to 2000 m^2/g or even higher, which means a couple of grams activated carbon will have a surface area similar to or even more than a soccer field.

In terms of structure, activated carbons are non-graphitizable and composed of imperfect sections of graphitic lamellae. It is possible to imagine taking perfect lamellae and 'cutting' them into sizes varying from about 1 nm to about 500 μm . The smaller sizes, 1-10 nm, can be crumpled and defects can be introduced. They can be 'bonded' together to create a three-dimensional network.

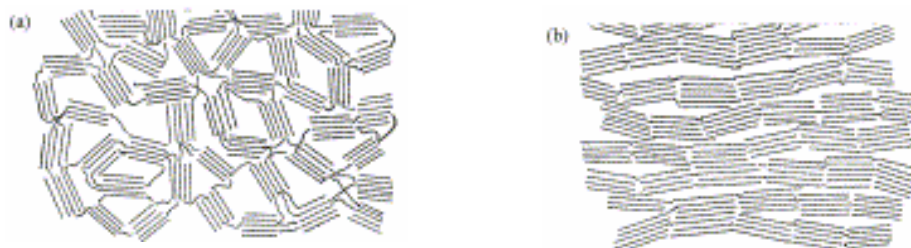


Figure 2.5 Franklin's representations of (a) non-graphitizable and (b) graphitizable carbons.

[Franklin51]

The first structural models of graphitizable and non-graphitizable carbons were put forward by Franklin in her 1951 paper [Franklin51]. In these models, the basic units are small graphitic crystallites containing a few layer planes, which are joined together by cross links. The precise nature of the cross-links is not specified. A schematic illustration of Franklin's models is shown in Fig. 2.5. Her theory of crystallite growth in carbons depended on the assumption that growth results from the movement of whole layers or large fragments rather than individual atoms. It follows from this that the degree of crystal growth will depend on the orientation of the individual structural units and the amount of cross-linking between them. In non-graphitizable carbons, the structural units are oriented randomly, as shown in Fig. 2.5(a), and the cross links are sufficiently strong to impede movement of the layers into a more parallel arrangement. On the other hand, the structural units in a graphitizable carbon are approximately parallel to each other and the links between adjacent units are assumed to be weak as shown in Fig. 2.5(b). The transformation of such a structure into crystalline graphite would be expected to be relatively facile.

The most serious shortcoming of Franklin's models for the structure of graphitizable and non-graphitizable carbons is that the nature of the cross-links between the graphitic fragments is not specified. Such cross-links must be extremely strong, since they are sufficient to prevent graphitization even at temperatures of 3000 °C and above. As far as models incorporating sp^3 -bonded carbon atoms are concerned, the main problem is that sp^3 carbons are thermodynamically unstable at high temperatures. Diamond is converted to graphite at 1700 °C, while tetrahedrally bonded carbon atoms in amorphous films are unstable above about 700 °C. Therefore, the presence of sp^3 atoms in a carbon cannot explain the resistance of the carbon to

graphitization at high temperatures. It should also be noted that the x-ray diffraction evidence for sp^3 -bonded atoms in non-graphitizable carbons has been questioned.

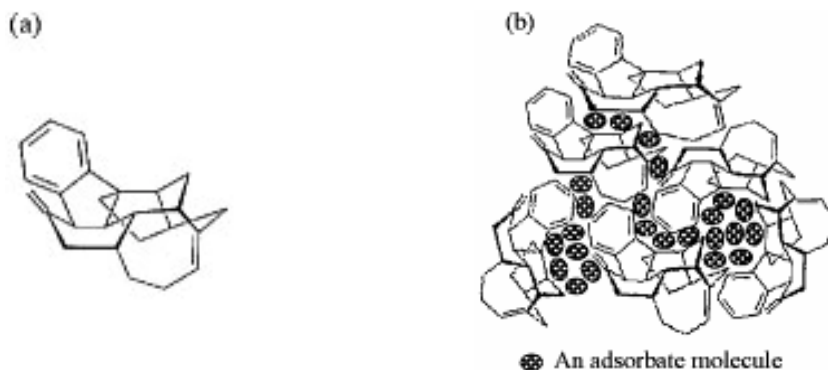


Figure 2.6 (a) Possible carbonaceous structural unit produced by pyrolysis of cellulose precursor, according to Byrne and Marsh, (b) model of microporous carbon made up of such units. [Byrne95]

Some models of disordered carbons have been put forward in which the carbons are not exclusively bonded in six-membered rings. These probably provide a much more realistic basis for understanding the structure of non-graphitizable carbons than the early models based on curved and twisted graphene sheets. Byrne and Marsh [Byrne95] discussed the structure of carbons produced by the pyrolysis of cellulose-type precursors. They suggested that such carbons might be made up of small structural units such as that illustrated in Fig. 2.6a. This structure contains sp^2 and sp^3 carbons bonded in five-, six-, and seven-membered rings. A group of such structures, with adsorbate molecules situated in the gaps between the units, is shown in Fig. 2.6b.

The structure forms during the manufacturing process, which involves two main steps: carbonization and activation. The carbonization of the carbonaceous raw material is achieved at temperatures below 800 °C in the absence of oxygen. During the carbonization, most of the non-carbon elements such as oxygen and hydrogen are removed as volatile gaseous products by the pyrolytic decomposition of the starting materials. Afterwards the material is activated. There are two principal activation methods, thermal activation and chemical activation. Thermal activation involves heating previously charred materials at high temperature (700-1100 °C) in the presence of oxidizing gas such as steam (H_2O). Chemical activation involves heating a mixture of the raw material and a dehydrating agent, e.g. nitric acid or sulfuric acid, to temperatures from 400 to 800 °C. During activation, the residual carbon atoms group into sheets of condensed aromatic ring systems with a certain degree of planar structure. The mutual arrangement of these aromatic sheets is irregular and therefore

leaves free interstices between them which may become filled with the tarry matter or the products of decomposition. These interstices give rise to pores, which make activated carbons excellent adsorbents. [Oberlin84] The characteristics of porosity in activated carbons will be introduced later in this chapter.

Activated carbons can be obtained from a wide variety of carbonaceous materials. The most frequently used on a commercial scale are peat, coal, brown coal, wood and coconut shell. However, it is not easy to control the extent and size distribution of resultant porosities when these natural feedstocks are used, for they have large structural variability. Therefore, in addition there are other precursors required from which to produce carbons with reproducible pore size distributions to meet specifications. Such precursors are the synthetic resins and other polymeric materials. In general the properties of the final product are determined by several factors such as the raw material used, the activating agent, and the conditions of the activation process. [Bansal88]

2.2.3 Carbon blacks

Carbon black mainly consists of carbon (ca. 97-99%) and is considered to be amorphous. Many models have been proposed for the structure of carbon-black particles and here we give one example from Heidenreich's publication in 1968 (see Fig2.7). It has similar microstructure to graphite. They are poorly crystallized solids in which assemblies of microcrystallites form spherical particles, disordered at the center of the particle, but tending towards an "onion peel" framework at the outer border. The interlayer distances are large: 0.35 to 0.36 nm, and never less than 0.34 nm even after thermal treatment at 3000 °C. They are therefore non-graphitizable carbons.

Carbon blacks are constituted by small, generally spherical particles (primary particles) with diameters in the size range of 10 to 75 nm depending on the method of preparation. In addition to variations in particle size, carbon blacks possess different types of aggregates. Aggregates consist of fused primary particles and range in size from 50-400 nm. The aggregate is considered to be the smallest dispersible unit (or working unit) of carbon black. [Dawson96, Cabot05] A low structure black is made of less primary particles compactly fused together and hard to disperse, while a high structure black is made of many primary particles with considerable branching and chaining thereby the graphite layer planes are continuous between the particles.

[Burgess71] Considering the performance, high structure carbon blacks have higher specific areas, higher conductivity and better dispersions.

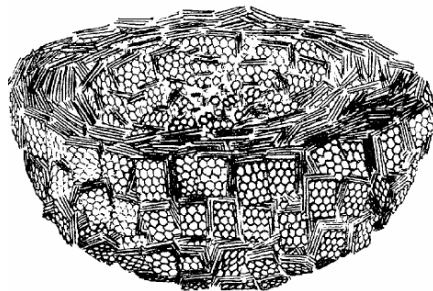


Figure 2.7 Microstructural model of carbon black [Heidenrich68]

Carbon black is electrically conductive and is widely applied for conductivity improvement in polymer engineering and electrochemical industry. When the carbon black is homogeneously dispersed and mixed with the matrix to a certain concentration, agglomerates of the aggregates are formed, in which a compact one-, two- or three-dimensional network of the conducting phase is then obtained, thereby increasing the conductivity. In the electrodes for our research, carbon blacks are blended with activated carbon and binders to form the active layer, as shown in Fig. 2.1.

The main stages of carbon-black formation in manufacturing processes involve the thermal decomposition or partial oxidation of hydrocarbons and the formation of polyaromatic macromolecules in the vapour phase followed by nucleation of these macromolecules into droplets, which are then converted into carbon black particles. The structure, characteristics and performance may significantly vary for different precursors and manufacturing processes. Three major manufacturing processes are applied to produce commercial carbon blacks – channel process, furnace process and thermal process.

2.2.4 Porosity in carbon

Activated carbons are used for electrode material for ultracapacitors because of their porous structure, high specific area, outstanding adsorption ability and low cost. Hence it is significant to understand the porosity in carbon, which involves the specific area, pore morphology and pore size distribution.

Based on the experiences of adsorption chemistry, total porosity is classified into three groups. IUPAC classifies porosities as follows: [Sing85]

Micropores width less than 2 nm

Mesopores width between 2 and 50 nm

Macropores width greater than 50 nm

It is useful as well to classify micropores further into ultra-(<0.7 nm width) and super- (1.0-2.0 nm) micropores, these definitions being relevant when considering physisorption behaviour.

For a discussion of the principle, adsorption of gasses is commonly employed. Micropores are considered as being about the size of adsorbate (the gas or vapour when adsorbed, the terms admolecule and adatom are also used in this context) molecules and accommodate one, two or perhaps three molecules. Mesoporosity is wider and is characterized by hysteresis loops stemming from capillary condensation during adsorption and desorption at high relative pressures of adsorption, which will be discussed in depth later. Macropores are transport pores to the interior of particles, and are considered as external surface.

The forces responsible for adsorption are van der Waals or London dispersion forces, which arise from induced dipole – induced dipole interactions. Unless some form of chemical bonding is involved, it is usually assumed that the surface is inert and therefore that the gas-solid interaction energy, Φ , is controlled by the change in potential energy of the gas molecule, by the depth of the potential energy well corresponding to the most favourable physisorbed site. For the simplest type of adsorption system, i.e. a small non-polar molecule on a uniform non-polar surface, the interaction energy may be expressed in the approximate Lennard-Jones (12:6) form as [Kittel96]

$$\Phi(r_{ij}) = B_{ij} \sum r_{ij}^{-12} - C_{ij} \sum r_{ij}^{-6}$$

where, i is a adsorbed molecule, j is an atom in the solid, r_{ij} is the distance between i and j , and B_{ij} and C_{ij} are characteristic repulsion and attraction constants for the gas-solid system.

The sorption behaviour in macropores is distinct from that of mesopores and micropores. Whereas macropores are so wide that they can be considered as nearly flat surfaces (see Fig. 2.8a). The sorption behaviour in micropores is dominated almost entirely by the interactions between fluid molecules and the pore walls; in fact the adsorption potentials of the opposite pore walls are overlapping. Hence the adsorption in micropores (i.e., micropore filling) is distinct from the adsorption phenomena occurring in mesopores. As illustrated in Fig. 2.8b, the pore potential in mesopores is not dominant anymore in the core of the pores. Hence, the adsorption

behaviour in mesopores depends not only on the fluid-wall attraction, but also on the attractive interactions between fluid molecules, which may lead to the occurrence of capillary (pore) condensation. Pore condensation represents a phenomenon whereby gas condenses to a liquid-like phase in pores at the pressure less than the saturation pressure P_0 of the bulk fluid. It represents an example of a shifted bulk transition under the influence of the attractive fluid-wall interactions.

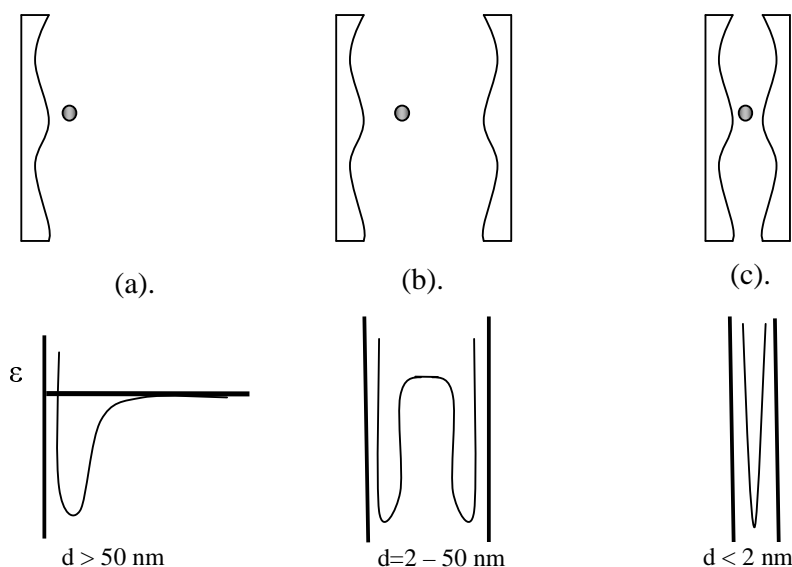


Figure 2.8 Schematic illustration of adsorption potential, ϵ , on (a) planar, nonporous surface; (b) mesopore; (c) micropore, d is pore width [Lowell04]

What the admolecule “sees” are atoms of adsorbent (the solid material on which adsorption occurs) separated from other adsorbent atoms, and sometimes there is just enough space (a volume element) for the admolecule to locate itself between several of these adsorbent atoms. During an adsorption process, adsorbent molecules diffuse through the network of interconnected micropores. The process of physisorption is dynamic. When a state of equilibrium is established between the adsorbed phase and the adsorbent, there is a continuous process of replacement of the adsorbed molecules within a pore. The frequency of change is of the order of 10^3 - 10^{10} s^{-1} . There is always diffusion into and out of the pores. During adsorption at low relative pressures, admolecules spend most of their time in the smallest (with highest energy) volume elements of the pores. All other volume elements act as transport pores. With progressive increase in relative pressure, adsorption takes place in volume elements of progressively increasing size (or decreasing energy). Some volume elements are

capable of holding two or three admolecules, and so establish the process of cooperative adsorption.

Porosity in solids is characterized by information contained within the adsorption isotherm. The adsorption isotherm is a description of equilibrium states of an adsorbate within an adsorbent. To quantify the adsorption process, the extent of adsorption (described as n_{ad} in mmol of adsorbate per gram of adsorbent) is related to the equilibrium partial pressure P/P_0 at constant temperature (where P is the equilibrium pressure of adsorption, and P_0 is the saturated vapour pressure at the selected temperature. P is normally lower than P_0 otherwise liquid condensation will occur, so the maximum for P/P_0 in the isotherms is 1).

Fig. 2.9 sets out the six major classes of isotherm shapes that are obtained from adsorption experiments.

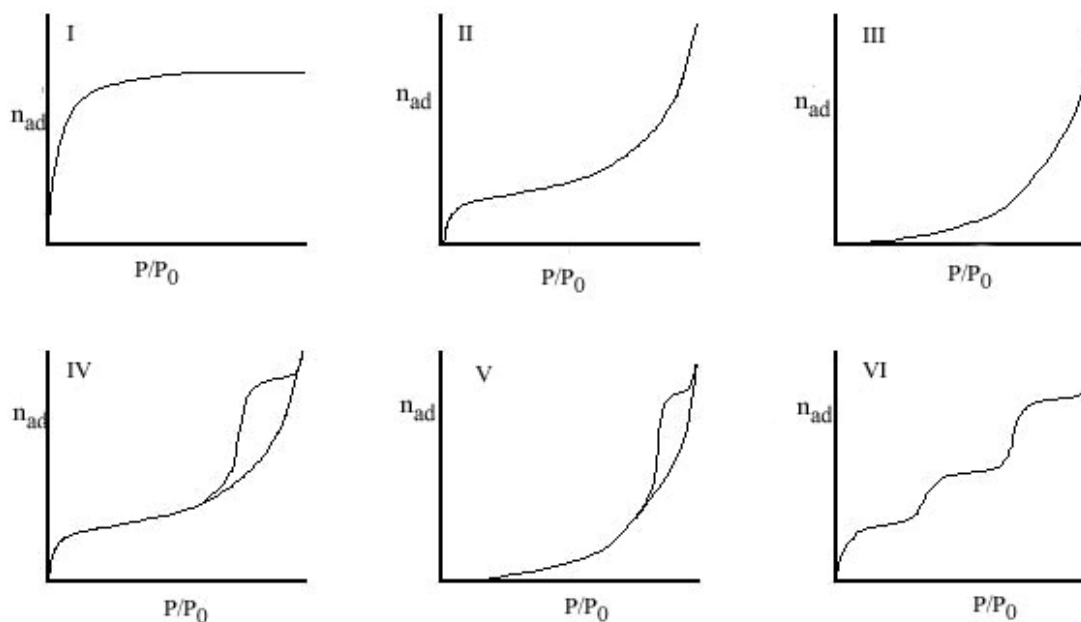


Figure 2.9 IUPAC classification of sorption isotherms [Sing85]

Type I isotherms are typical for microporous solids in which micropore filling occurs significantly at relatively low partial pressure $<0.1 P/P_0$, the adsorption process being complete at appr. $0.5 P/P_0$. Examples include the adsorption of nitrogen on microporous carbon at 77 K and of ammonia on charcoal at 273 K.

Type II isotherms describe physisorption of gases by non-porous solids. Monolayer coverage is succeeded by multilayer adsorption at higher P/P_0 values without restriction. Carbons with mixed micro- and mesoporosity can also exhibit this type of adsorption behaviour.

Type III and Type V isotherms are convex toward the relative pressure axis. These isotherms are characteristic of weak gas-solid interactions, where the interaction between the adsorbates is stronger than that between adsorbent and adsorbate.

Type IV isotherms show a hysteresis loop which is associated with mesoporous solids, where capillary condensation occurs. The vapour over concave surfaces (internal pore surfaces) may condense at pressures lower than the condensation pressure for flat surfaces. This difference of the pressure of condensation and evaporation for some pores (corresponding to the same adsorbed amounts) results in isotherm hysteresis.

Type VI isotherm is a stepwise isotherm and represents complete formation of successive monomolecular layers.

In order to confine the conditions for mathematic modeling, various pore shapes have been assumed for activated carbons, e.g. slit pore, cylindrical pore, bottle neck and wedge. For example, Dubinin Radushkevich (DR) equation for microporosity assessment and micropore size distribution are based on the slit pore model. This will be introduced in detail in Chapter 3.

2.2.5 Interfacial chemistry and electrochemistry of carbon surfaces

As mentioned earlier in this chapter, solid carbons make up a very long list of materials and they have diverse physical and chemical characteristics. In spite of their diversity, solid carbons share two unique features:

- the presence of sp^2 -hybridized carbon exhibiting at least two-dimensional order
- the possibility with which they combine with other elements (e.g., oxygen) to form a variety of surface functional groups.

The second feature has important consequences for the utilization of these materials. On the positive side, the tremendous flexibility of solid carbons provides the possibility to produce materials with optimum surface chemical, electrochemical, and physical properties for selected applications. On the other hand, the properties (in particular the chemistry and the electrochemistry) of final products are invariably difficult to predict, to evaluate and to reproduce. The accumulated knowledge about the properties of solid carbons relies heavily on the interpretations obtained over the years using data generated by a wide variety of experimental techniques such as temperature programmed desorption (TPD), X-ray photoelectron spectroscopy (XPS), infrared (IR), Boehm's titration (acid-base titration) and electrochemical

measurements like cyclic voltammetry. Unfortunately, when applied to solid carbons, many physical and virtually all chemical characterization tools fail to provide direct, unambiguous results. Nevertheless, all techniques that uncover differences among samples are important, because their underlying theories and inferences provide (i) a much needed frame of reference and (ii) a basis for critical, comparative assessment. At the present time, the following are generally agreed upon as being well-known facts about carbon surfaces [Leon94]:

- They can form chemical or physical bonds with other substances;
- They can accommodate Bronsted acid sites, Lewis basic sites, and sites capable of taking up or giving up single electrons (i.e., oxidizing or reducing sites, respectively). (Bronsted acid is proton donor and the Bronsted acidity is defined according to the proton donating ability of a substance, and on the contrary Bronsted base is a proton acceptor. Lewis acid is a molecular entity that is an electron-pair acceptor, in turn the Lewis acidity describes the electrophilicity; Lewis base is normally the electron-pair donor.)
- Many heteroatoms hold on tenaciously to the surface and can only be removed at the expense of some carbon (e.g., oxygen adsorbed at temperatures as low as 233K being primarily released, upon heating, as CO and CO₂);
- Oxygen is invariably the most common heteroatom found on carbon surfaces, a fact that explains the large number of studies devoted to oxygen functional groups.

One notion widely accepted is that clean carbon surfaces are made up of (at least) two chemically different kinds of sites, basal and edge carbon atoms. The validity of this assumption was confirmed for highly pure graphite, by noting that the reactivity of edge sites toward oxygen is over one order of magnitude higher than that of basal sites [Henning66, Thomas65] Logically when the structural order of solid carbons decreases, its edge-to-basal site ratio increases, and so does the carbon's overall reactivity. [Radovic83] The surface reactivity can lead to the presence of surface functionalities, usually involving oxygen species.

As shown in Fig. 2.10 various surface functionalities have been proved to exist in carbon materials. The unique character of most functional groups stems from the fact that they are made up of heteroatoms whose electronegativities are different from those of carbon atoms. The more electronegative atom in a bond tends to acquire a negative partial charge, leaving the other atom with a positive partial charge, thus the

functional groups fall into two categories: donor groups shift the electron cloud away from them and acceptor groups shift the electron cloud towards them. Donor groups contain σ - or π -electron pairs (e.g., OH, OR, O(C=O)R), which can partially donate and behave as Lewis base. Acceptor groups contain empty orbitals (e.g., (C=O)OH, (C=O)OR, (C=O)H), which tend to partially fill by withdrawing electrons from their neighbouring atoms and behave as Lewis acid. Carbon substrates generally contain aromatic portions that permit both electron cloud and charge delocalization via extended π bonding. The distinction between donor and acceptor groups is important in that it sets the stage for the generation of acidity scales for functional groups on carbon surfaces. If taking the conventional Bronsted strength, i.e. the ability to donate a proton, as the standard, acceptor groups are weaker Bronsted acid because they tend to localize the electron cloud density around them and this makes them less willing to release protons while donor groups on the other hand, tend to form stronger Bronsted acid. Carbon substrates largely determine the extent to which these effects can take place. For instance, if one compares the Bronsted acid strength of ArOH and Ar(C=O)OH (where Ar presents an aromatic substrate), one finds that the latter is more acidic because, even though it acquires charge from the substrate, it manages to spread it between its two oxygen atoms through resonance. The former is willing to give electrons but cannot spread its charge as efficiently as the latter.

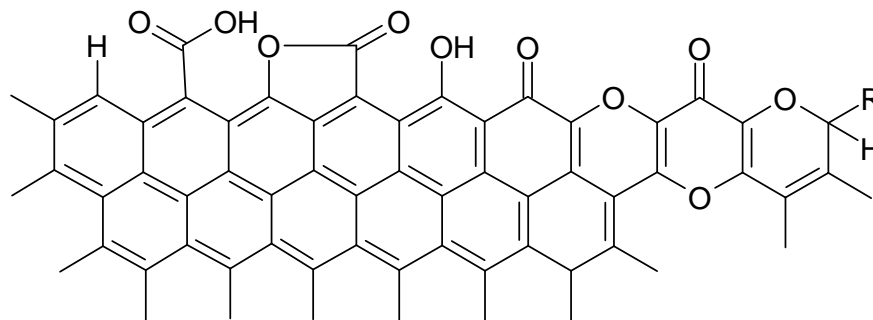


Figure 2.10 Functional groups on carbon surface (density of functional groups exaggerated)

On the other hand, carbon surfaces respond to electrochemical stimuli. Either some of the functional groups can be oxidized or reduced, or they act as an intermediate to promote the oxidation or reduction of other species in the surrounding. The occurrence of these two kinds of reactions involves a transfer of electrons (rather than ions). Considering the functional groups on the surface of carbon, there are quite a few unpaired electrons, such as delocalized π electrons and localized σ , as shown in

Fig. 2.11. Their amount is normally proportional to the surface area. This is taken as an indication that one or more types of oxygen functional groups could act as electron acceptors.

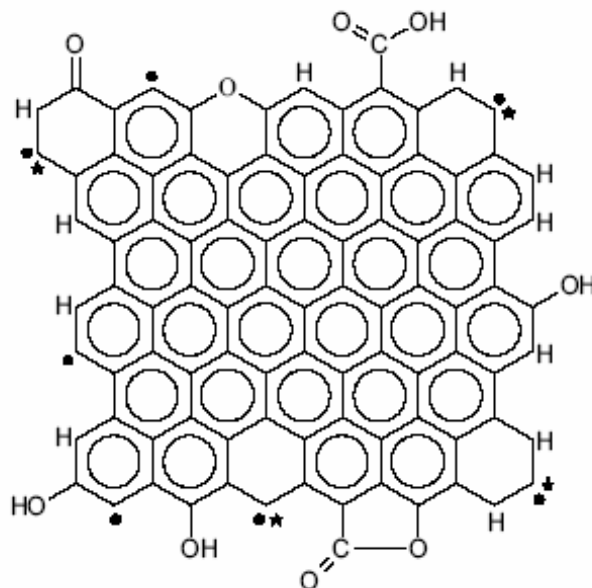


Figure 2.11 Schematic representation of a graphene layer including the oxygen containing functional groups at the edges. Dot and dot+* mean unpaired σ . electron and in-plane σ pair (where * is a localized π electron), respectively. [Radovic99] (All carbon atoms in the structure are supposed to be sp^2 hybridized, and it is difficult to illustrate with “double/single alternating bonds”.)

IR evidence [Zawadzki89] and a number of electrochemical observations have provided some solid basis for the electron transfer process by radicals produced by quinoid on carbon surfaces. Other functional groups could in principle intervene as well, e.g. carbonyl, phenolic groups. Some of the functional groups like carboxyl groups (except carboxylic acid) may not be so active in electron transfer as quinoid groups, but this might be due to the fact that the energy needed to effect the electron transfer could actually break bonds which will result in the decomposition of the structure. In this regard, one must bear in mind that on solid carbons the nature of the substrate can have a substantial effect on the electrochemical behaviour of the available functional groups; for instance, large aromatic substrates and “activating” functional neighbours can facilitate their reduction. For instance (see Fig. 2.12), quinoid functionalities consist of a couple of carbonyl groups placed on the edge of the common graphene layer (structure I). Resonance considerations permit the stabilization of a number of radicals (structure II) in equilibrium with structure I. These radicals may take up electrons and become anions (structure III and V). The

anions may further bind protons in solution, as shown in structure IV and VI. In this case, quinoid functionalities are transformed into phenol groups. This behaviour resembles very much that encountered on quinhydrone electrode, for which the reaction $C_6H_4O_2 + 2H^+ + 2e^- = C_6H_4(OH)_2$ is well documented.[Janz61, Midgley91]

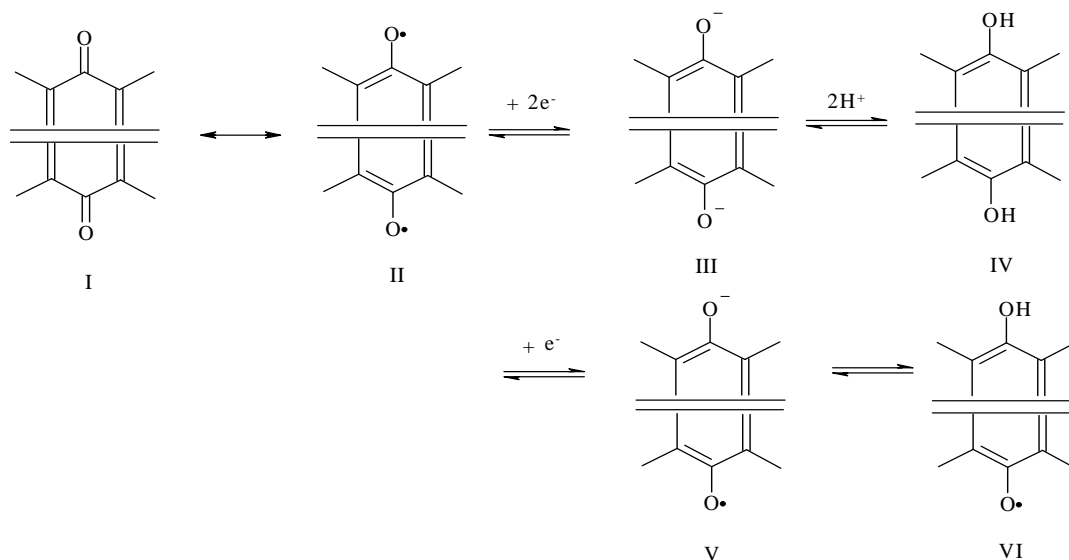


Figure 2.12 Electron transfer activity of quinoid sites.

In general, the existence of various functional groups on the surface of carbon significantly influences the physical and chemical properties of the material. It also offers many possibilities for complicated chemical and electrochemical reactions.

2.3 Electrolyte

From the working mechanism introduced in the first chapter, the electrolyte can influence the performance of ultracapacitors in two aspects. One is the working potential, which determines the energy stored in the system, the other is the equivalent series resistance (ESR) that will influence the power output.

As shown in the first chapter, the energy stored in ultracapacitors is proportional to the square of the working potential, which is normally limited by the electrochemical stability window of the system, in most cases, much smaller than that. The electrochemical stability window is defined as the potential range in which an electrode can be polarized in a solution without the passage of substantial Faradaic currents. In general, this parameter for a solid-liquid system is limited by the electrochemical stability of the salt or the solvent or by the dissolution or degradation of the electrode. Hence, the nature of the solvent, the nature of the salt, the nature of

the electrode materials will all influence the electrochemical stability window. Sometimes the impurities in the system might also affect the electrochemical stability.

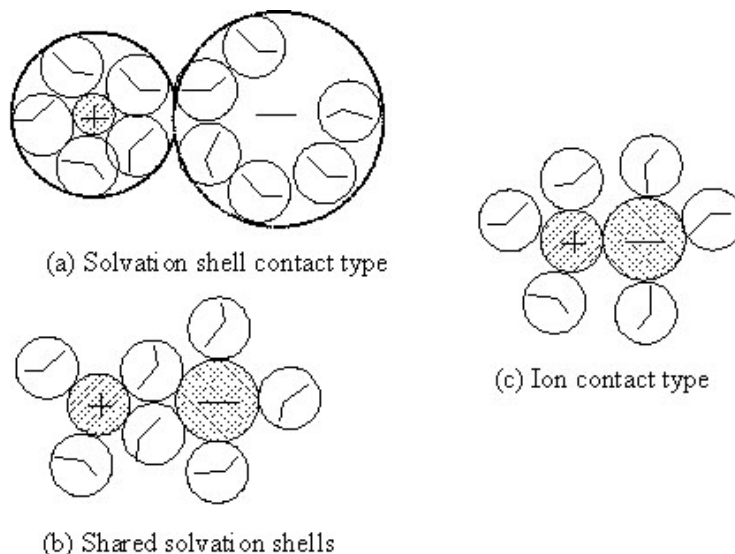


Figure 2.13 Types of ion pairs in an electrolyte solution (taking aqueous system as example): (a) solvated-ion pairs (b) solvent-shared ion pairs, and (C) contact ion pairs

For the conductance of the electrolyte-solvent system, two principal factors are involved. One is the concentration of free charge carriers e.g., cations and anions, and another is the ionic mobility or conductance contribution per ion. The former is normally determined by the degree of dissociation into free ions. Basically, in order to obtain good solubility and charge separation in solution, the charge density of the ions has to be low, and thus bulky anions and/or cations have to be chosen. The mobility is related to the ionic concentration, temperature and the dielectric constant of the solvent. It has been recognized that the variation with solvent can be described in terms of two general types of solvents, designated “leveling” and “non-leveling” or “discriminating”. Three stages of ion pairing, depending on the extent of retention of solvation, are illustrated in Fig. 2.13. A leveling solvent is one that provides strong solvation and a tendency for complete dissociation or minimum ion pairing, as (a) in Fig. 2.13. Such solvents are usually those that have high dielectric constants, often with hydrogen-bonded structures with large dipole moments, and lead to less differentiation (hence leveling) of conductivities due to ion pairing. Non-leveling solvents lead to a wider differentiation of the conductivities, mainly on account of solvent-specific ion pairing that is related to ion size and solvation, and to the

dielectric constant and donicity of the solvent. The ion-pairing degree can be loose like (b) or compact like (c) in Fig. 2.13.

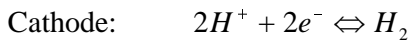
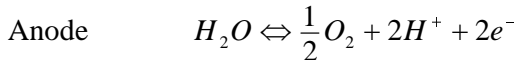
2.3.1 Aqueous media

H^+ , K^+ and Na^+ have the highest mobility (U) and conductivity of equivalent solution (λ_0) among the cations, and SO_4^{2-} and OH^- have the highest values among the anions. Their ionic properties at infinite dilution in aqueous solutions at 25°C are shown in table 2.1. [Bard01] So H_2SO_4 or KOH are normally chosen for the aqueous electrolyte in carbon-type double-layer capacitors. [Conway99]

Table 2.1 Ionic Properties at Infinite Dilution in Aqueous Solutions at 25 °C [Bard01]

Ion	$\lambda_0, \text{cm}^2\Omega^{-1} \text{equiv.}$	$U(\times 10^{-4}), \text{cm}^2\text{sec}^{-1}\text{V}$
H^+	349.82	36.25
K^+	73.52	7.619
Na^+	50.11	5.193
OH^-	198	20.52
$1/2SO_4^{2-}$	79.8	8.27

High conductivity highly improves the property of ESR of electrochemical double layer capacitors, and this system is especially suitable for high power output. However, the decomposition limit from water is thermodynamically 1.2 V, as mentioned before or practically, in kinetic terms, 1.3-1.4 V. Redox reactions are as follows:



To prevent the ESR increasing from the depletion of ions in the electrolyte, relatively concentrated electrolytes are required. In this case, corrosion of the hardware components has to be taken into account, which is important for the design, reliability and self-discharge characteristics of the capacitor device. From this point of view, neither H_2SO_4 nor KOH is ideal, for they are both highly corrosive.

From these discussions, it is obvious that although aqueous electrolytes yield low ESR values, their electrochemical stability window is narrow. A wider electrochemical stability window is necessary for the “energy performance” of ultracapacitors. Consequently, nonaqueous electrolytes have attracted more attention.

With nonaqueous media, a much wider variety of electrolyte-solvent systems are available and has been extensively investigated.

2.3.2 Nonaqueous media

As mentioned above, nonaqueous media have the advantage of wider electrochemical stability windows over aqueous systems, however, this also means requirements for the solvent and salt are stricter – the content of impurities and water has to be controlled.

2.3.2.1 Solvent

The criteria for the choice of solvents depend on the following factors:

- The reactivity of the solvent toward the electroactive species and the electrode material.
- The polarity, and hence the ability to dissolve salts and provide appropriate conductivity.
- The electrochemical stability window of the solvent (which means the voltage domain without solvent reaction). As discussed below, this parameter, however, may relate strongly to the salt chosen [Aurbach91]. It should be emphasized that the electrochemical window relates strongly with the purity. For instance, trace oxygen and water are highly reactive in many systems, and their reduction may interfere with the purely electrochemical behaviour of the system, thus limiting the electrochemical window of the solvent-salt system [Cotton66, Aurbach90]. Hence, the possibility of obtaining highly pure material is also an important criterion for the choice of solvent.
- Safety aspects such as toxicity and flammability. They are of major concern in applications as well as the cost.
- Physical aspects such as volatility, melting and boiling points.

Out of above concerns, suitable solvents for ultracapacitors are mainly from the following three classes:

- 1) High dielectric constant (close to water at $\epsilon = 81$) dipolar aprotic solvents such as organic carbonates, ethylene carbonate (EC, $\epsilon = 89.1$) and propylene carbonate (PC, $\epsilon = 69$);
- 2) Lower dielectric dielectric constant but high donor-number (a measure of the ability of a solvent to solvate cations and lewis acids) solvents such as ethers, dimethoxy ethane (DME), tetrahydrofuran (THF);

3) Intermediate dielectric constant aprotics such as acetonitrile (ACN), dimethylformamide (DMF), dimethylacetamide (DMA) and butyrolactone (BL).

The first comprehensive set of data on the oxidation reactions of nonaqueous electrolyte solutions, as well as their positive anodic limit for use in electrochemistry, was prepared by Mann [Mann70]. Table 2.2 summarizes some useful selected data from his review.

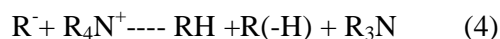
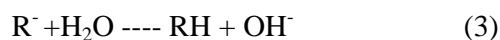
Table 2.2 Oxidation potentials and reactions of nonaqueous systems

Solvent	Salt anion	Working electrode	Reference electrode	Anodic limiting reaction/products	Limiting potential(V)
ACN	ClO_4^-	Pt	Ag/AgNO ₃	$\text{ClO}_4^- - e^- \rightarrow \text{ClO}_4\cdot$; $\text{ClO}_4^- + \text{CH}_3\text{CN} \rightarrow \text{HClO}_4 + \cdot\text{CH}_2\text{CN} \rightarrow \text{NCCH}_2\text{CH}_2\text{CN}$	2
ACN	BF_4^-	Pt	Ag/AgNO ₃	Reaction unidentified, CH ₃ CONH ₂ was detected	4
PC	ClO_4^-	Pt	Hg/Hg ₂ Cl ₂ /KCl	Unidentified	1.7
DMF	ClO_4^-	Pt	Hg/Hg ₂ Cl ₂ /KCl	HCON(CH ₃)CH ₂ · formation	1.6
THF	ClO_4^-	Pt	Ag/AgClO ₄	Unidentified	1.5-1.8

From Mann's review, it is clear that the anion of the electrolyte and the electrode material have a pronounced effect on the oxidation potentials of the nonaqueous systems. When the anion is ClO_4^- , its oxidation onset at potentials above 1.5 V versus Ag/Ag⁺ may promote further intensive solvent degradation, as was found with ACN. It is important to note that using BF_4^- instead of ClO_4^- in ACN extended its anodic stability by 2 V. Later on, more work has been conducted on the anodic stability with nonaqueous reference electrodes, whereas the data correspond well to the data provided by Mann obtained with aqueous reference electrodes.[Zyat'kova93] It appears that acetonitrile is the solvent with the highest anodic stability and PC is more reactive than acetonitrile from this point of view. [Lund01] Moreover, acetonitrile is advantageous from its physical properties. For example, ACN has lower viscosity and the conductivity of TEATFB in ACN is higher than that in PC. Recently, the work by the group of Lust in the University of Tartu, Estonia, indicated in their research that pore resistance, i.e. the internal distribution of the electrode resistance with ACN as solvent is much lower than that with PC. [Arulepp04, Lust04, Lust02, Lust03]

2.3.2.2 Electrolyte salts – cathodic and anodic reactions

As discussed before, the first criterion for the choice of salts that can be used with respect to the solvents is appropriate conductivity. In order to obtain good solubility and charge separation in solution, the charge density of the ions has to be low, and thus bulky anions and/or cations have to be chosen. Hence, in electrochemical double layer capacitors, the cations may be onium ions such as tetraalkylammonium ions (R_4N^+) and tetraalkylphosphonium salts and sometimes may be Na^+ , K^+ in aqueous systems. Tetraalkylammonium salts have come into favor due to their better solubility and conductivity in the high dielectric constant solvents. This cation is preferred in applications since it avoids the possibility of alkali metal deposition on the cathode of a capacitor upon adventitious overcharge, which would lead to passivation. Furthermore, the reduction potential of this cation is very low thereby a wide electrochemical window can be obtained. Work of Peters' group in Indiana University [Dahm96] indicated that, when using glassy carbon as working electrode, the cathodic stability of tetraethylammonium in dimethylformamide can reach appr. -3.0 V vs. saturated calomel electrode at 25 °C. A number of investigations have dealt with the cathodic reaction of tetraalkylammonium on various electrodes. [Simonet77, Bernard79, Bernard82, Finkelstein59, Finkelstein65, Ross60, Ross70, Simonet98] Tetraalkylammonium is reduced according to the mechanism shown below. Alkanes, alkenes and trialkylamines are the main products. The size of alkyl group may influence the ease of reaction and yield from the point of stereochemistry.



The commonly used anions are also characterized by relatively bulky structures, such as BF_4^- , ClO_4^- , PF_6^- , AsF_6^- , $SO_3CF_3^-$. The anodic stability of the above salts is in following order: $AsF_6^-, PF_6^- \geq BF_4^- > SO_3CF_3^- \geq ClO_4^-$ [Ciemieki84, Ue94]. As shown in table 2.2, when the anion is ClO_4^- , its oxidation onset at potentials above 1.5V (vs. Ag/Ag^+) may promote further solvent degradation, as was found in ACN. When using BF_4^- instead of ClO_4^- in ACN, the anodic stability limit is extended by 2V.

The oxidation potentials of PF_6^- and BF_4^- are even higher than that of the solvents ACN and PC. Hence the oxidation potential limit of the system when applying these salts is due to the solvents rather than the salts.

Table 2.3 Electrolytic conductivities ($\text{mS}\cdot\text{cm}^{-1}$) of organic liquid electrolytes at 1 mol/l, 25°C [a. Ue94, b. House71, c. Rousseau72]

Electrolyte	PC	DMF	ACN
Et_4NBF_4	13 ^a	26 ^b	56 ^b
Bu_4NBF_4	7.4 ^a	14 ^b	32 ^b
Et_4NPF_6	12 ^a	25 ^a	55 ^a
Bu_4NPF_6	6.1 ^a	13 ^a	31 ^a
$\text{Et}_4\text{NCF}_3\text{SO}_3$	11 ^a	21 ^c	42 ^c
$\text{Bu}_4\text{NCF}_3\text{SO}_3$	5.7 ^a	11 ^c	23 ^c
Et_4NClO_4	11 ^a	24 ^b	50 ^b
Bu_4NClO_4	6.0 ^a	12 ^b	27 ^b

Table 2.3 presents some data on the electrolytic conductivities of salts composed of the cations and anions discussed above. Et_4NBF_4 in ACN has the best conductivity. Combined with the aforementioned electrochemical stability, this electrolyte system shows obvious advantages.

2.4 Current collector – aluminium foil

Aluminium foil is normally applied for the current collector.

Similar to the majority of wet electrolytic capacitors, aluminium with etched surface is applied to improve the contact between the aluminium foil and the activated carbon layer.

A number of methods have been developed for the roughening of the aluminium surface, including sand blasting, mechanical embossing, scratching with rotating brushes, use of abrasive materials and chemical/electrochemical etching with acids and salts. Of all proposed and known methods of roughening the anode surface, the chemical/ electrochemical etching processes have been found to be most satisfactory and are therefore in general use, in one form or another.

The manner in which various reagents etch aluminium is usually characteristic of the specific etching agent; in general, however, alkali tends to attack aluminium surfaces

uniformly, whereas certain of the acid reagents have a definite roughening action. Etching with alkali, therefore, reduces the thickness of the anode material uniformly with only a minor increase in effective surface area. Hydrochloric acid (single or in combination with metal chlorides), however, has a pronounced roughening action, increasing the anode surface area.

Aluminium exposed to air always has a thin film of oxide on its surface. The full roughening action of the hydrochloric acid cannot become effective until this oxide film is penetrated. As a result, the most effective way of etching aluminium foil is to first remove the oxide film by the uniform attack of an alkali hydroxide, such as NaOH. NaOH is best used hot and in concentrations from 4 to 10 per cent. The time of immersion can be determined by experiment, but should only be long enough to remove the surface film with less material loss of metal.

The characteristics of the aluminium sheet or foil are also important in determining the results obtained by etching. For best results, the foil should be especially fabricated for etching. There is a definite relation between the crystal structure of the metal and the effectiveness of the etching. It has been found, for example, that aluminium, annealed to a high temperature, has a coarser grain structure than aluminium annealed for a long period of time at a lower temperature. Hard drawn aluminium does not etch as satisfactorily as soft aluminium, and the coarser grain structures produce the best results.

The purity of aluminium also has a marked effect on the etching results; aluminium of a purity of 99.99% will be hardly affected by the same procedure which produces full effective etching of aluminium of a purity of 99.8%. It might be mentioned in passing, that full advantage is taken of this fact in obtaining an accurate method of quickly checking for total aluminium content of aluminium foil.

Etching of aluminium foil brings with it the important problem of removing all traces of chlorides and other contaminating substances, such as other metals, from the surface. Metals such as iron and copper plate out electrolytically on the aluminium and must be later removed. This is invariably accomplished by treatment with nitric acid.

One important point that has to be mentioned here is the influence of current collector foil on the anodic stability limit of electrochemical windows in nonaqueous systems. As has been found for lithium ion battery, at potentials above 3V (vs. Li/Li⁺), many nonactive metals that are important as current collectors (e.g., Ni, stainless steel and

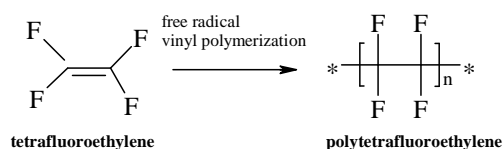
Al) may oxidize and dissolve. However, the metal cation and the salt anion (e.g. ClO_4^- , halides, AsF_6^- , BF_4^- , SO_3CF_3^-) may form insoluble salt that passivates the electrode and thus prevent massive dissolution of the electrode material at high potentials. Hence, in many cases we obtain an apparent stability of metal electrodes because of passivation. A typical case is aluminium, which is the most preferred current collector for 4V cathodes in Li ion batteries, they can withstand even much higher potentials. This is because the most commonly used salts for Li batteries (which comprise fluorinated anions such as BF_4^- , AsF_6^-) liberate active fluoride (e.g., due to trace HF unavoidably present with these salts, or formed by hydrolysis with trace water). It is assumed that at high potentials, AlF_3 is formed, which passivates the electrode very efficiently, preventing Al ion diffusion into the solution. Fortunately, the AlF_3 film is sufficiently thin to allow electron tunneling, and thus the electrical contact with the electrode active mass is maintained. [Aurbach99]

2.5 Binder

There are quite some choices for the binders for ultracapacitors like fluoropolymers polyvinyl alcohol, polyvinyl acetate, polyvinyl butaryl, methyl cellulose, and carboxymethylcellulose. [Mushiake00]

Fluoropolymers are most widely applied in the ultracapacitors for their excellent stability and versatility. In the family of fluoropolymers, there are various products such as polytetrafluoroethylene (PTFE), Polyvinylidene fluoride (PVDF) ethyltrifluoroethylene (ETF) and fluorinated ethylene propylene (FEP). PTFE is the most well known and widely applied one.

PTFE is made of a carbon backbone chain, and each carbon has two fluorine atoms attached to it. PTFE is a vinyl polymer, and its structure, if not its behaviour, is similar to polyethylene. Polytetrafluoroethylene is made from the monomer tetrafluoroethylene by free radical vinyl polymerization. This molecule is highly repellent to other materials and has very high chemical stability. Only few substances can attack it in extreme conditions. To increase the adhesion of PTFE to other materials, the PTFE surface is often activated.



In the present studied system, a fluoropolymer is applied as the major binder.

Chapter 3

Methods

3.1 Structural characterization

3.1.1 Gas volumetric porosimetry

The adsorbed amount as a function of pressure can be obtained by volumetric (manometric) and gravimetric methods, carrier gas and calorimetric techniques, etc. However, the method most frequently used for the micropore characterization in the materials like activated carbon, is the gas volumetric measurement.

3.1.1.1 Working principles

The gas volumetric method is based on calibrated volumes and pressure measurements by applying the general gas equation. It is performed by the addition of a known volume of gas (adsorbate), typically nitrogen, to a solid material in a sample vessel at cryogenic temperatures. At cryogenic temperatures, weak molecular attractive forces will cause the gas molecules to adsorb onto a solid material. An adsorbate is added to the sample in a series of controlled doses, the pressure in the sample vessel is measured after each dosing. By measuring the reduced pressure due to adsorption, the ideal gas law can be used to determine the quantity of gas adsorbed by the sample. As discussed in Chapter 2, the resulting relationship of volume of gas adsorbed vs. relative pressure at constant temperature (P/P_0 , where P is the equilibrium pressure of adsorption, and P_0 is the saturated vapour pressure at the selected temperature) is known as an adsorption isotherm.

It was noted by Freeman [Freeman70] and Marsh [Marsh87] that an experimental adsorption isotherm is a very specific curve. An isotherm is indicating how many pores are filled at each level of site energy or adsorption potential. The total isotherm is a description of the distribution of adsorption potential within the sample. The linearization of an experimental isotherm is stating that the distribution of adsorption potentials of about 10^{21} sites per gram, can be described in terms of a mathematical equation of statistical distributions, e.g. a Rayleigh, Gaussian, Lorentzian or log-normal distribution. [Marsh65, 67]

3.1.1.2 Adsorption equations

The Langmuir equation is based on the assumptions that: (1) only monolayer adsorption can occur, (2) adsorption is localized, with no adsorbate-adsorbate interactions and (3) the heat of adsorption is independent of surface coverage, i.e. the adsorbent has a homogeneous surface. These assumptions are invalid for sure for any real surface except for very low coverage (θ). Thus, it is just introduced as the base for other model but not applied in the present work.

Brunauer, Emmett and Teller (BET), in 1938, extended Langmuir's kinetic theory to multilayer adsorption. The BET model assumes that the uppermost molecules in adsorbed stacks are in dynamic equilibrium with the vapour. Since the equilibrium is dynamic, the actual location of the surface sites covered by one, two or more layers may vary but the number of molecules in each layer will remain constant. The equation (for unrestricted multilayer formation) is

$$\frac{P}{V(P_0 - P)} = \frac{1}{V_m \times c} + \frac{(c-1)}{V_m \times c} \times \frac{P}{P_0} \quad (3-1)$$

where, P = equilibrium pressure

P_0 = saturation vapour pressure at adsorption temperature

V = volume of gas adsorbed

V_m = volume of gas adsorbed on the first monolayer

c = constant related exponentially to the heat of adsorption in the first layer.

Plotting $P/V(P_0 - P)$ against P/P_0 results in a line with a slope of $(c-1)/V_m \times c$ and an intercept of $1/(V_m \times c)$. Thus the volume of gas adsorbed on the first monolayer (V_m) and the constant (c) can be obtained. Furthermore, by using the ideal gas law, at the standard temperature and pressure (STP), the molar volume of an ideal gas is 22414 cm^3 , so the number of molecules required to cover the monolayer (n) can be calculated by

$$n = \frac{V_m}{22414 \text{cm}^3 \cdot \text{mol}^{-1}} \quad (3-2)$$

When the cross-sectional area of the adsorbate molecule (A_m) is known, the total surface area of the adsorbent is given by $S_t = A_m Ln$, where L is Avogadro's number. Thus the specific surface area (S) of the adsorbent can be calculated from the total surface area (S_t) and the sample weight (w) as $S = S_t/w$. [Brunauer38, Lowell04, Quantachrome01].

The BET equation requires a linear plot. For most solids, using nitrogen as the adsorbate, the linear region is restricted to a limited region in the P/P_0 range of 0.05 to 0.35. This linear region is shifted to lower relative pressures for microporous materials. It is found in our research, in the P/P_0 range of 0.01 to 0.10, a linear behavior is well reproduced for most of the samples. The so-called five point BET is then applied for specific area calculation, which takes five volume and relative pressure values in the linear region to obtain slope and intercept. The error of the BET method can be high due to its inherent drawbacks – the modeling for this equation does not describe the process of adsorption in microporous carbons. In micropores no real multilayer adsorption can really happen (refer to Fig. 2.8).

The Dubinin-Radushkevich (DR) equation [Dubinin47] differs from the Langmuir and BET equations in that it is not based on a model process to describe the physisorption of gasses but on considerations of energies of adsorption. Dubinin recognized that the adsorption energy for ultramicropores (diameter at 0.4 to 0.7 nm) is much higher than for supermicropores (diameter at 0.7 to 2 nm) due to enhanced adsorption effects in microporosity, as introduced in Chapter 2. With a slit-shaped pore model as the basis for the theory, Dubinin proposed that ultramicro- and supermicropores fill differently according to their respective adsorption potential and the interaction between the adsorbed molecules (refers to Fig.2.7). The “primary micropore filling” takes place at very low P/P_0 (e.g. 10^{-5} to 10^{-2}) and involves the entry of individual molecules into pores of molecular dimension (in the range $d = \sigma$ to 2σ , d is the distance between two walls of the pore, σ is the molecular diameter of adsorbate). Secondary micropore filling is believed to be a cooperative process, occurring in the wider micropores (e.g. in slits of $d \approx 2\sigma$ to 5σ) and involves adsorbate-adsorbate interaction or quasi-multilayer adsorption. This mechanism is known as TVFM (the volume filling of micropores).

Dubinin et al. also assumed that the distribution of pore sizes was heterogeneous and followed a Gaussian distribution [Dubinin47]. They postulated that the fraction of the adsorption volume V occupied by liquid adsorbate at various adsorption potentials can be expressed as a Gaussian function:

$$W = W_0 e^{-\left(\frac{A}{\beta E_0}\right)^2} \quad (3-3)$$

where,

W = volume of adsorbate filled micropore (cm^3/g) at relative pressure P/P_0 and temperature (K)

W_0 = total volume of the micropores (cm^3/g)

A = adsorption potential, asserted to be $A = RT \ln \frac{P_0}{P}$ when the adsorbate is in the liquid state

β = adsorbate affinity coefficient

E_0 = characteristic energy of the adsorbent

Substitution and simplification yields:

$$\lg W = \lg W_0 - \frac{BT}{\beta} \left(\lg \frac{P_0}{P} \right)^2 \quad (3-4)$$

where, B is a structural constant, which can be obtained from the slope and taken as a qualitative measure of the relative average micropore size of the adsorbent as shown in equation 3-4. The larger the B value is, the lower the characteristic energy E_0 is and the larger the average micropore size is (i.e. a wider distribution). Hence the following information can be obtained by interpreting an adsorption isotherm using the DR equation, (1) extent of micropore volume capacity; (2) relative pore-size distributions; (3) deviations of adsorption energies from a Gaussian or related type of distribution.

3.1.1.3 Pore size distribution (PSD) analysis

The distribution of pore volume with respect to pore size is called a pore size distribution. In the last half century, many models have been proposed for pore size distribution in micropore range, e.g. methods based on the experimental correlations – DR method as described above, Dubinin-Astakhov (DA) method, Horvath-Kawazoe (HK) method [Horvath83] and Saito-Foley (SF) method [Stoeckli90]; and in the mesopore range, methods based on the Kelvin equation such as Barret, Joyner and Halenda (BJH) method [Barrett51] and Dollimore and Heal (DH) method [Dollimore64]. But these classical macroscopic theories normally do not give a realistic description of the filling of micropores and even narrow mesopores because each of them is based on some assumptions in order to simplify the situation. This leads to an underestimation of pore sizes.

In contrast, molecular models of adsorption such as density functional theory (DFT) and Monte Carlo (MC) simulations, based on statistical mechanics, give a much more accurate description of adsorption phenomena [Cracknell95]. Based on given

intermolecular potentials of fluid-fluid and fluid-solid interactions, they allow the construction of adsorption isotherms in model pores. [Seaton89, Aukett92, Lastoskie93, Olivier95, Olivier97, Quirke96, Gusev97, Gusev97, Jagiello04, Jagiello98]

An important assumption is normally made when DFT is used to model adsorption in an amorphous material: the material is made up of a collection of independent, non-interconnected pores of some simple, defined geometry (usually of slit or cylindrical shape). And in experimental systems the adsorbed fluid in a pore is in equilibrium with a bulk gas phase. For such a system the grand canonical ensemble provides the appropriate description of the thermodynamics.

The general procedure is as follows:

- 1) Define the interaction potentials for the fluid-sorbent and fluid-fluid interactions with Leonard-Jones potential. The fluid interactions with the sorbent will depend, among other things, upon the structural and chemical nature of the surface, the shapes and sizes of the pores in the material, and the connectivity of the porous network.
- 2) Apply statistical mechanics to calculate the sorbent property (which we shall denote Ψ) for individual pores of size H , shape (denoted symbolically as g), and surface interaction Φ_{sf} (the solid fluid intermolecular potential, which in general depends on the surface location), at specified temperature T and pressure P .
- 3) Calculate the overall sorbent property Ψ_t at state conditions T and P by integrating the individual pore properties over the distribution of pore sizes, pore shapes, and surface interactions:

$$\Psi_t(T, P) = \iiint \Psi(H, g, \Phi_{sf}; T, P) f(H, g, \Phi_{sf}) dH dg d\Phi_{sf} \quad (3-5)$$

In practice, the distribution function $f(H, g, \Phi_{sf})$ is rarely available from experiment for such calculations. Instead, one can fit the model results for individual pores to experimental property data to extract desired distribution information. For highly ordered crystalline sorbents such as zeolites, this procedure can yield detailed structural information. Activated carbons, by contrast, are less well ordered sorbents that generally possess a broader distribution of pore sizes, geometries, and so on. For these sorbents it is more difficult to characterize the complete distribution function $f(H, g, \Phi_{sf})$. In order to render the problem tractable, it is proposed to replace above equation by the simpler equation

$$\Psi_i(T, P) = \int \Psi(H; g, \Phi_{sf}, T, P) f(H) dH \quad (3-6)$$

where, $f(H)$ is the PSD. This equation will be correct for materials having a single pore geometry and chemically homogeneous surfaces. For real materials, in which geometric and chemical heterogeneity occurs, $f(H)$ is regarded as giving the PSD for an effective porous material, in which all of the heterogeneity of the real material is approximated by a distribution of pore sizes. [Lastoskie93]

To solve for the pore size distribution of porous carbons, model isotherms are fitted to experimental nitrogen uptake measurements. Mathematically, the experimental isotherm $N(P/P_0)$ is expressed as

$$N\left(\frac{P}{P_0}\right) = \int_{H_{\min}}^{H_{\max}} \rho\left(\frac{P}{P_0}, H\right) \times f(H) \times dH \quad (3-7)$$

where, $N(P/P_0)$ = experimental adsorption isotherm data

H_{\min} = width of the smallest pores considered in the analysis

H_{\max} = width of the largest pores considered in the analysis

$\rho(P/P_0, H)$ = the mean density of nitrogen in a pore of width H at (P/P_0)

$f(H)$ = pore size distribution function

The density functional theory provides the individual pore isotherms $\rho(P/P_0, H)$, which are then applied to the experimental adsorption measurements in the numerical solution of the integral to obtain the pore size distribution $f(H)$.

3.1.1.4 Instrumentation

Low-temperature measurements with gases such as argon and nitrogen are generally preferred for gas volumetric methods. The quantity of gas remaining in the gas phase is measured. The amount of gas adsorbed at equilibrium pressure is given as the difference between the amount of gas admitted and the amount remaining in the space around the adsorbent. A schematic description of this type of instrument can be found in Fig. 3.1.

The principle behind this method consists of consecutively introducing known amounts of adsorbate to the sample, which is kept at liquid nitrogen temperature (77 K). Adsorption of the injected gas in the sample causes the pressure to slowly decrease until an equilibrium pressure is established in the manifold. The equilibrium pressure is measured by a transducer chosen according to the pressure range where adsorption is established during the experiment. The gas uptake is calculated directly

from the equilibrium pressure values. The raw experimental data are the equilibrium pressures and the amount of gas adsorbed for each step. Helium is applied for the calibration of the instrument and calculation of the dead volume in the manifold.

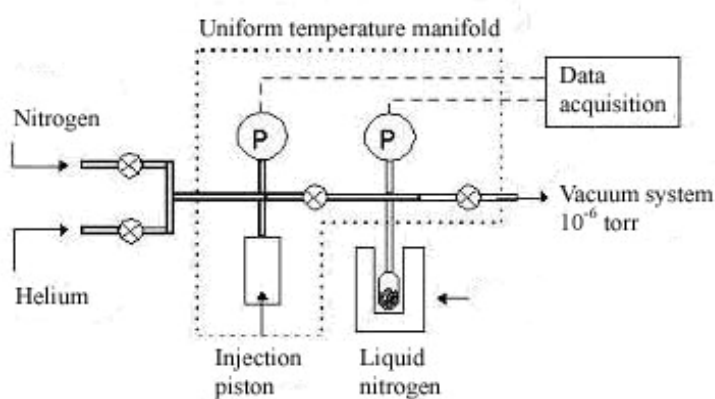


Figure 3.1 Volumetric adsorption measurement

All physisorbed material must be removed from the adsorbent surface before the isotherm is determined. This is usually achieved by outgassing the adsorbent at elevated temperature.

3.1.2 Raman spectroscopy

Raman spectroscopy is widely applied in condensed matter physics and chemistry to study vibrational, rotational, and other low-frequency modes in a system. It is a powerful technique to diagnose the internal structure of molecules and crystals, and is widely used for the structure identification of graphite, diamond and other carbon materials.

3.1.2.1 Working principles and characteristics

When the light strikes an object, most of the photons are elastically scattered, i.e. the scattered photons have the same energy and wavelengths as the incident photons, which is called Rayleigh scattering (as shown in Fig. 3.2a). However, a small fraction (approximately 1 of 10^7 photons) can be inelastically scattered by quasi-particle excitations of the medium, which is termed the Raman effect, thereby either giving energy to the medium (Stokes scattering, as shown in Fig. 3.2b) or removing energy from it (anti-Stokes scattering, as shown in Fig. 3.2c). Anti-Stokes transitions are much weaker than Stokes and hard to detect in conventional experiments.

Raman scattering is, as a rule, much weaker than Rayleigh scattering and most experiments require an intense source which is as monochromatic as possible – a laser with a narrow linewidth is usually used – and the collected light must be carefully filtered to exclude the dominant Rayleigh signal. Other potentially large sources of non-Raman signal include fluorescence (the decay of long-lived electronic excitations) and of course light from ambient sources. Fluorescence can be particularly pernicious to a Raman measurement because the fluorescence signal is also shifted from the laser frequency, and so can be much more difficult to avoid. (Note that although the fluorescence spectrum is shifted from the laser frequency, the fluorescence shift depends on the laser frequency whereas the Raman shift does not).

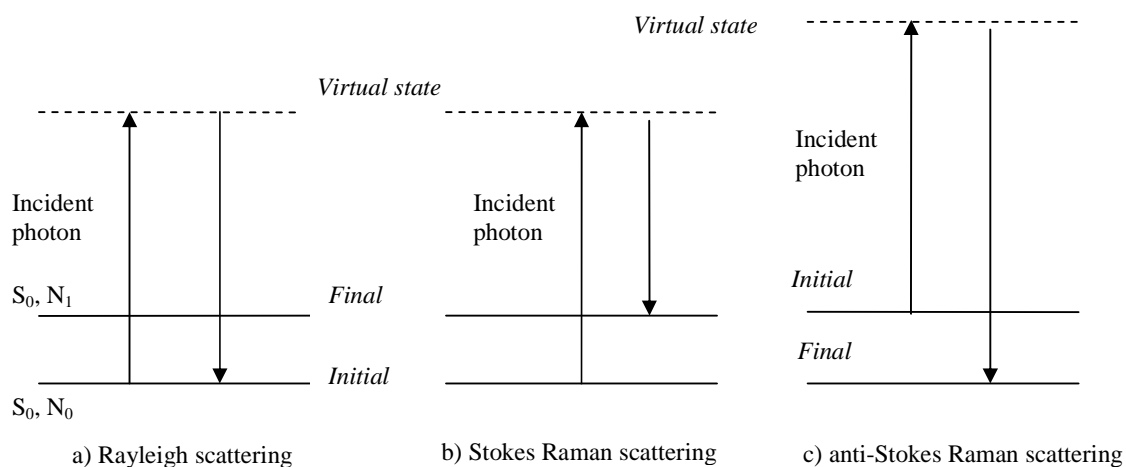


Figure 3.2 Schematic representations of the energy levels of Rayleigh and Raman scattering. S_0 and N_0 : electronic and vibrational ground state; N_1 : first excited vibrational state

Excitation with easily available laser lines in the visible range means that Raman effect is in the energy range of molecular and lattice vibrations. For solid samples, the Raman effect involves a coupling between incident photons and quasi-particle excitations such as phonons (lattice vibrations) and electronic single particle or collective excitations within a sample, which results in the emission of light from the sample, shifted in frequency from the incident “excitation” light.

Single resonance Raman is widely known in Raman spectroscopy and frequently used to study the electronic and vibrational properties of crystals or molecules. This occurs when the virtual state approaches an electronic excited state, thereby resulting in a large enhancement of the Raman cross section and an increase of the Raman signal up to a factor of 10^6 [Martin83]. Closely related is the idea of double resonant Raman

scattering, where the phonon energy has to match the energy difference between two electronic bands in excited states. Double resonances are much stronger than single resonances. However, they are only observed under very specific conditions: the energetic difference between two electronic bands is adjusted to the phonon energy by applying electric or magnetic fields, uniaxial stress, or by a proper choice of the parameters of semiconductor quantum wells [Miller86, Cerdeira86, Alexandrou88, Gubarev91]. Double resonant conditions were thereby realized for distinct excitation energies. [Thomsen00]

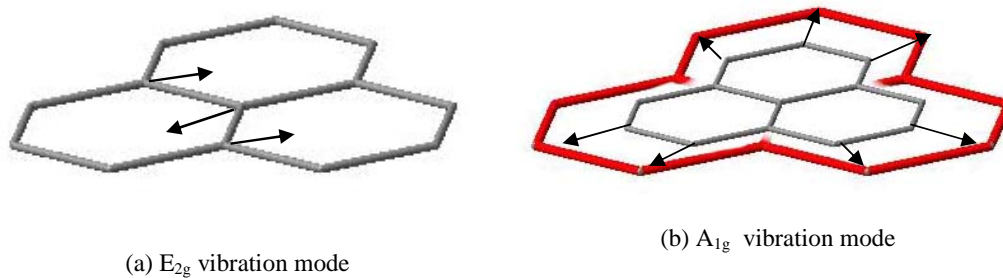


Figure 3.3 Vibration modes in carbonaceous materials

The first order Raman spectra of carbonaceous materials show two significant modes. Besides the G mode with an E_{2g} symmetry at around 1600 cm^{-1} (as shown in Fig. 3.3a) there is an additional defect induced peak, the so-called D mode with A_{1g} symmetry at about 1380 cm^{-1} (see Fig. 3.3b). [Tuinstra70, Vidano81, Kawashima95, Kauschke87, Nemanich79] The D mode is related to the finite crystallite size and disappears for perfect crystals. Its frequency was found to shift with excitation energy at a rate of $40\text{-}50\text{ cm}^{-1}/\text{eV}$ over a wide excitation energy range [Vidano81, Wang90, Sood98], a phenomenon which has not been well understood until now. A relatively convincing explanation was recently proposed by Thomsen and Reich that double resonances are responsible for the observation of the defect induced D mode in graphite and its peculiar dependence on excitation energy. The double resonance considered has a much stronger enhancement than simple incoming or outgoing resonances and this explains why the defect mode (and its second order peak) is so strong compared to the graphite Γ point vibration [Thomsen00]. The ratio of the intensities of these two peaks gives information on the microstructure of carbonaceous materials.

3.1.2.2 Instrumentation

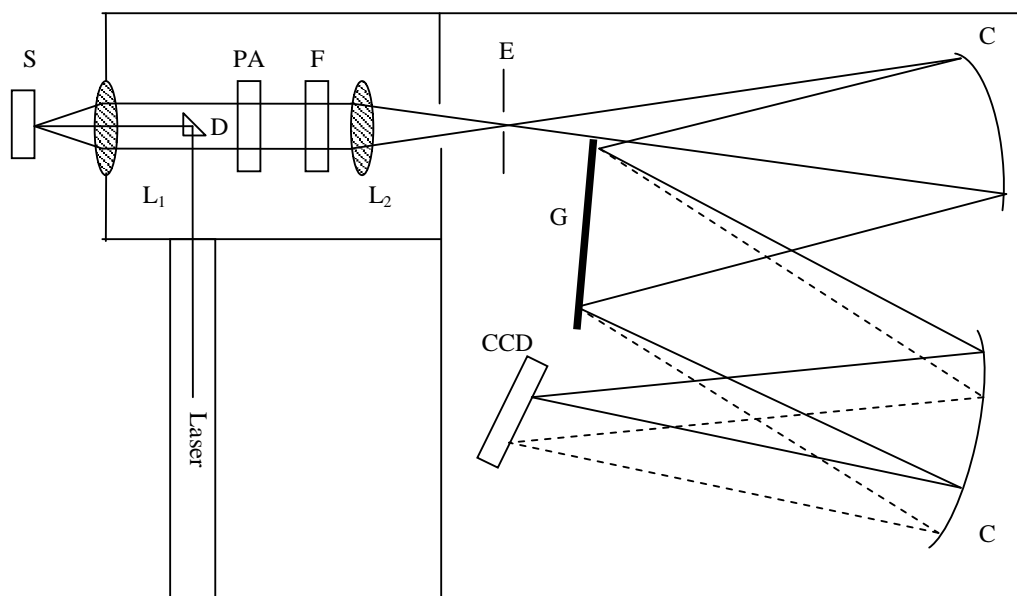


Figure 3.4 Schematic picture of Raman spectrometer and detector, S sample, PA polarization analyzer, D deflection prism, L_{1,2} lenses, F filter for suppressing the Rayleigh line (on interference basis or holographically), E entry slit, G grating, C collimator mirrors, CCD charge-coupled device

In the present work, a Raman-microscope-spectroscope is applied. Fig. 3.4 shows a schematic picture of the Raman spectrometer and detector. In standard Raman configuration, a laser beam is filtered for monochromaticity and directed by a system of mirrors to a focusing/collecting lens. The beam is deflected onto the sample; the scattered light which passes back through the same lens is then passed through a second lens into the spectrometer. Between the two lenses there is a polarization analyzer and a filter for suppressing the Rayleigh line (on interference basis or holographically). The spot size of the laser beam can be adjusted from 10 to 40 μm with various lens. After entering the spectrometer the light is reflected from the collimator mirror C onto the grating G, spectrally separated there, and it finally hits the detector.

Nowadays, multichannel charge-coupled devices (CCD), in which the different positions (wavelengths) are read simultaneously, are most used for Raman detectors. The wavelength/intensity information is then read to a computer and converted in software to frequency/intensity. This is the Raman spectrum raw data.

3.2 Chemical Analysis

3.2.1 X-ray photoelectron spectroscopy (XPS)

X-ray photoelectron spectroscopy (XPS), also called electron spectroscopy for chemical analysis (XPS), is one of the most widely used surface characterization methods. The popularity of XPS as a surface analysis technique is attributed to its high information content, its flexibility in addressing a wide variety of samples, its sound theoretical basis, and its nondestructiveness.

3.2.1.1 Working Principles and Characteristics

XPS is working on the basis of the photoelectric effect [Einstein05]. When a photon impinges upon an atom, the energy of the photon might be totally transferred to an electron and excite the emission of the electron from the atom.

The basic physics of this process can be described by Einstein equation, simply stated as $E_B = h\nu - KE$, where E_B is the binding energy of the electron in the atom, which represents the difference in energy between the electrons in ionized and neutral atoms; $h\nu$ is the energy of the radiation source ($h =$ Planck constant 6.62×10^{-34} J·s, $\nu =$ frequency of the radiation in Hz) and KE is the kinetic energy of the emitted electron that is measured in the XPS spectrometer.

Fig. 3.5 and Fig. 3.6 show the energy level diagram for an electrically conductive sample and an electrically insulating sample, respectively.

For a conductive sample, by grounding the sample and the spectrometer, the Fermi levels of the sample and spectrometer are aligned thereby E_B can be obtained by

$$E_B = h\nu - KE - \phi_{sp}$$

where ϕ_{sp} is the work function of the spectrometer.

However, when the sample does not have sufficient electrical conductivity, the Fermi levels are not aligned and binding energy cannot be drawn from the working function of the spectrometer anymore. Normally an additional source of electrons is required to compensate for the positive charge built up by emission of the photoelectrons. As shown in Fig. 3.6, the energy equation now becomes:

$$E_B^{vac} = E_B^f + \Phi_s = h\nu - KE + \Phi_e$$

Thus, binding energy (E_B) is referenced to vacuum level of the sample (E_{vac}) and the energy of the charge neutralization electrons (Φ_e). This makes it difficult or

impossible to measure absolute E_B values, and in this case an internal reference is best to be introduced for calibration.

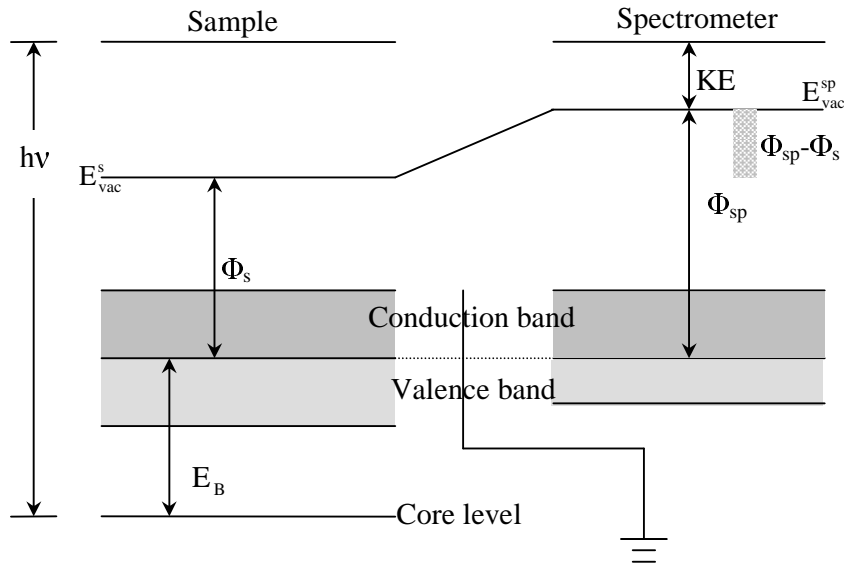


Figure 3.5 The energy level diagram for an electrically conductive sample that is grounded to the spectrometer. The Fermi levels of the sample and spectrometer are aligned ($E_f^s = E_f^{sp}$) so that E_B is referenced with respect to E_f . The measurement of E_B is independent of the sample work function, Φ_s , but is dependent on the spectrometer work function, Φ_{sp} .

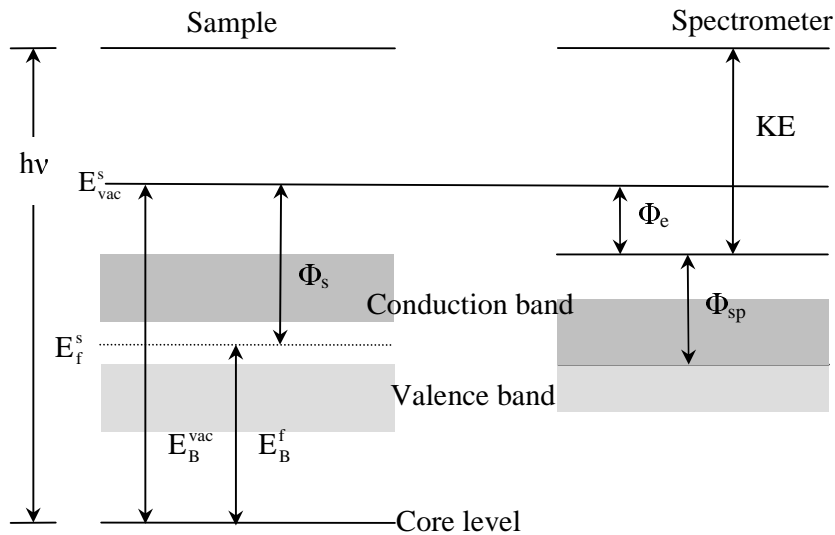


Figure 3.6 The energy level diagram for a sample electrically insulated from the spectrometer. The vacuum level of the sample (E_{vac}^s) is aligned with the energy of the charge neutralization electrons (Φ_e) so that E_B is referenced with respect to Φ_e . The measurement of E_B is dependent on the sample work function, Φ_s [Ratner97]

In XPS, X-ray, as the irradiation source, can penetrate the sample on the scale of 1000 nm, while electrons with the energy ranging between 10 and 1000 eV are only able to

penetrate less than 10nm. The small inelastic mean free path (IMFP) of electrons, which is defined as the average length over which the electron can travel without energy loss, enables XPS's high surface sensitivity. The sampling depth into a solid is normally within a few nm depending on the materials and electron energy, and sensitivity reaches 0.1 to 1 monolayer. In XPS, only the photoelectrons possessing characteristic emission energies will contribute to the photoemission peaks, while electrons emitted from the surface zone that have lost some energy due to inelastic interactions will form a scattering background.

A closer look at the process shows that the binding energy of the electron in the atom is determined by the initial state and final state of the electrons. The initial state is the ground state of the atom prior to the photoemission process, which is mainly determined by the type of the atom. The core electron of an element has a unique binding energy, which can be seen as a "fingerprint". If the energy of the atom's initial state is changed, e.g. by formation of chemical bonds with other atoms, E_B will shift with a fixed value, which is defined as chemical shift. Hence through the analysis of the binding energy of defined elements, the chemical composition of a sample can be obtained. Take carbon as an example, when carbon is bonding to a hydrogen atom, the binding energy of C1s (corresponds to the electrons in the 1s level in C atom) is typically at 284.6eV. When hydrogen is substituted by other elements like oxygen, nitrogen and the bonding changes, the binding energy will change. Upward shifts in binding energies result from a decrease in electron density around the nucleus in question (i.e., from oxidation), whereas downward shifts result from an increase. Linear correlations between these shifts and the charge on given atoms can be expected and have been reported for carbon-oxygen, carbon-nitrogen, carbon-fluorine functional groups, etc. [Papirer78, HP72, Albers92]

On the other hand, the binding energy is also determined by the final state which is mainly dependent on the relaxation effect in solids. In all cases the electron rearrangements during photoemission will result in the lowering in E_B . Contributions to the relaxation energy arise from both the atom containing the core hole (atomic relaxation) and its surrounding atoms (extra-atomic relaxation). Sometimes, the final state effects can help to obtain information about the chemical environments. However, in our research, this final state influence is not expected to be of significance.

Furthermore, as already discussed, when the electrical conductivity of the sample is not sufficient, positive charge accumulation may occur due to the excitation of photoelectrons and then result in the shift of binding energy to higher values. In this case, an additional source of electrons to compensate for the charge effect will be necessary. Ideally, this is accomplished by flooding the sample with a monoenergetic source of low-energy (<20 eV) electrons, e.g. from a heated tungsten filament.

An unambiguous interpretation of XPS spectra in our research is not straightforward. Problems arise because, e.g. (i) the external (probed) and the internal composition of a solid carbon sample may differ, and they often do; (ii) in porous carbons external voids can constitute a portion of the probed space and artificially lower the measured concentration of surface species, especially those close to, but not necessarily at, the gas-solid interface (e.g., carbon); (iii) charging effect as described above can render measuring absolute E_B values difficult and even impossible and a proper standard has to be applied, which is not available in our case, as will be discussed in the related chapter; (iv) the deconvolution of lumped C 1s, O 1s, or N 1s peaks into individual components and a proper assignment is far from being straightforward at present, although software offers quick solutions. [Bansal88, Stoehr90, Papirer78, HP72, Albers92]

From the point of quantification, since the spectral peaks from a mixture or a compound are approximately the sum of all the elemental peaks from the individual constituents and the intensity of one peak is proportional to the number of atoms in the surface regions, a semi-quantitative analysis of chemical composition is feasible. Since XPS is based on the excitation of electrons at core levels and since the atoms have different levels, each element shows different sensitivity to the excitation. This is normally defined as sensitivity factor, which is proportional to the intensity of the peaks. By measuring the peak areas and correcting them by sensitivity factors (in addition an instrumental fact has to be incorporated), the relative abundance of each detected element can be determined. For a sample with defined stoichiometry and high purity, XPS can give quantitative results with good reproducibility and accuracy. While the atomic percentage of the element decreases toward the XPS detection limits (ca. 0.1 atomic percent), the relative standard deviation will increase significantly. For inhomogeneous samples, the reliability of the quantification from XPS is questionable. In addition, the presence of contaminants also disturbs the quantitative

analysis at the surface of samples. In this case, sputtering is a good tool for cleaning the sample.

3.2.1.2 Instrumentation

For XPS, normally three parts are indispensable:

- 1) Ultra-high vacuum system ($< 1 \times 10^{-9}$ Torr) is applied to exclude the interference from gas particles to electrons and keep the cleanliness of the analyzed surfaces.
- 2) X-rays are applied for the source of radiation because the energy of soft X-ray is in the range from 200eV to 2000eV and compatible with the binding energy of the electrons at core levels in nearly all elements. X-rays are produced by impinging a high energy electron beam at around 10 keV on an anode (Al or Mg are most commonly applied, normally called $AlK\alpha$ and $MgK\alpha$ X-ray). A monochromator between the X-ray source and sample is normally used to narrow the energy spread of X-rays striking the sample, improve the resolution, and prevent electrons, satellite X-ray lines and heat radiation from striking the sample.

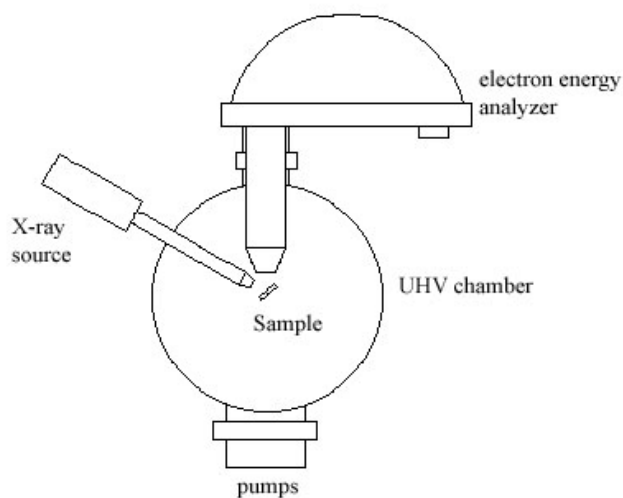


Figure 3.7 A Schematic diagram of an XPS spectrometer

- 3) Analyzers are applied to measure the flux of emitted electrons of a particular energy. Typically, there are two types of electron detectors: concentric hemispherical analyzer (CHA), cylindrical mirror analyzer (CMA). The preferred option for photoemission experiments is CHA, which uses an electric field between two hemispherical surfaces to disperse the electrons according to their kinetic energy.

Electrons with a range of energies are allowed to successfully travel from the entrance to the exit of the analyzer without a collision with one of the hemispheres, electrons with energies outside this range will be dispersed as shown in Fig. 3.8. The center line potential (thick broken line in Fig 3.8) is known as the pass energy. The higher the pass energy is, the stronger signal is achieved, while the resolution is lower. So normally for the survey scan to find the elements, higher pass energy is applied, and when detailed assignment for chemical shifts is necessary, lower pass energy is more suitable.

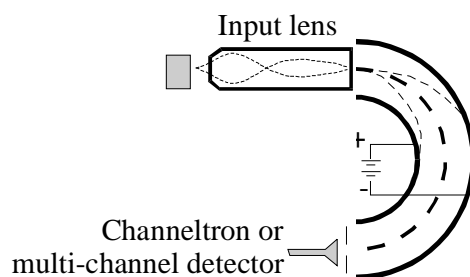


Figure 3.8 Schematic diagram of CHA analyzer

3.2.2 Fourier Transformed Infrared(FTIR)

IR spectroscopy is widely applied for the determination of molecule structure and identification of compounds. Its attractiveness comes from its enormous versatility, simple sample handling, fast information collection, nondestructiveness, as well as its low cost compared to other techniques which requires high vacuum for operation. It offers the information for detailed identification of the functional groups on the surface of activated carbons, which cannot be reached from the XPS results.

3.2.2.1 Working Principles and Characteristics

Infrared (IR) spectroscopy measures the infrared intensity versus wavelength (or energy in wavenumbers) of light. Based upon the energy, infrared light can be categorized as far infrared ($4 \sim 400\text{cm}^{-1}$), mid infrared ($400 \sim 4,000\text{cm}^{-1}$) and near infrared ($4,000 \sim 14,000\text{cm}^{-1}$). The mid IR region is of greatest practical use for functional group identification.

Through energy uptake, the atoms in molecules can be excited to vibrate around their state of equilibrium. Like the energy of the electrons, the vibrational energy is also quantized, which means only when the radiant energy matches the energy of a specific molecular vibration, absorption can occur. Certain groups of atoms absorb

energy and therefore give rise to bands at approximately the same frequencies so that the position of absorption bands is characteristic. Thus the energy usually given in wavenumbers, sometimes referred to as frequencies at which a molecule absorbs radiation give information on functional groups present in the molecule. This offers the possibility of directly stating the structural groups.

As we already introduced in Chapter 2, various carbon-oxygen functional groups exist on the surface of carbon materials. To distinguish these functional groups, infrared has the inherent advantage that similar functional groups will behave differently when they are connected to different elements or other functional groups. Taking carbonyl group C=O as an example, it has a characteristic vibration at about 1750 cm^{-1} in lactones, 1730 cm^{-1} in esters, 1700 cm^{-1} in carboxylic acids, 1580 cm^{-1} in quinoids. This can remedy the disadvantage of XPS that signals from these groups will convolute, and allow better assignment of XPS peaks.

Optical phonons can also be excited by infrared radiation because they, too, correspond to a mode of vibration creating a time-varying electrical dipole moment. Phonons that interact in this way with light are called infrared active. Phonon vibrations of the graphite lattice can normally be found at about 1588 cm^{-1} in infrared spectra. This mode has been observed widely in the infrared spectra of carbonaceous materials while the interpretation does not reach a consensus, which will be discussed in Chapter 5.

IR spectroscopy is very closely related to Raman spectroscopy [Colthup90, Hendra91, Grasselli91]. Both types of spectroscopy often give similar spectra, but also sufficient differences exist so that they can provide supplemental or complementary information. For example, for symmetrical molecules with an inversion center, bands appear in the Raman spectra are not found in the IR spectrum, and vice versa. The difference of the selection rule of IR and Raman is, in order to be IR active, a vibration must cause a change in the dipole moment of the molecule, while in Raman, there must be a change in polarizability of the molecule. The polarizability is a measure for the “deformation capability” of the electron shell.

Fourier transform infrared (FTIR) is widely applied. Interferometry is applied for the experiment so that all wavelengths are measured simultaneously, then a Fourier transform is calculated to convert the collected interferogram to the spectrum. This has the advantages of multiplexing (fast), throughput (high intensity) and higher wavenumber stability compared to dispersive IR spectrometer.

Researchers have tried for a long time to apply FTIR to characterize the functional groups existing on the surface of carbonaceous materials. [Puente98, Iglesias98, Rositani87, Starsinic83, Zhuang94, Zawadzki89, Zawadzki78, Zawadzki81, Ishizaki81, Biniak97, Danderkar98, Valente04, Moreno-Castilla97, Fanning93] But for this purpose, normal transmission FTIR faces two problems, one is the strong absorption of carbon. Well-distinguished spectra are not easy to record since the total complete mid IR range is affected. The other is the content of functional groups in carbonaceous materials is relatively low. For this reason, attenuated total reflection infrared is applied.

Attenuated total reflection infrared (ATR-IR) spectroscopy, also known as internal reflection spectroscopy (IRS), is a versatile, nondestructive technique for obtaining the infrared spectrum of materials which are either too thick or too strongly absorbing to be analyzed by transmission spectroscopy. For bulk material or thick film, no sample preparation is required for ATR analysis and air is normally chosen as reference.

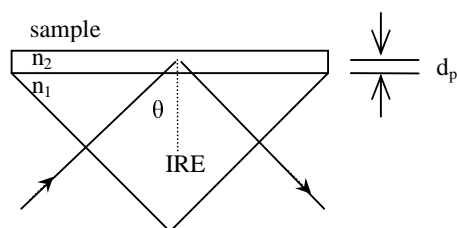


Figure 3.9 Schematic representation of total internal reflection with single reflection. n_1 =refractive index of the internal reflection element; n_2 = refractive index of the sample with $n_2 < n_1$, θ =angle of incidence; d_p = depth of penetration, $n_1 > n_2$

For ATR-IR spectroscopy, the infrared radiation is passed through an infrared transmitting crystal with a high refractive index such as Ge in order to get a total reflection of the radiation within the ATR element, see Fig. 3.9. The sample surface is pressed into close optical contact with the top surface of the crystal. The IR radiation from the spectrometer enters the crystal. It then reflects through the crystal and penetrates into the sample a finite amount along the top surface via the so-called “evanescent wave”. The intensity of the evanescent wave decays exponentially with the distance from the surface of the internal reflection element. As the effective penetration depth is usually a fraction of a wavelength, total internal reflectance is generally insensitive to sample thickness.

However, total reflection never occurs if the sample absorbs the electromagnetic wave. The internal reflection technique measures the reduction of reflectivity due to the absorption by the sample. Since the IR source is polychromatic, some of the electromagnetic waves are totally reflected while others are not for the usual samples measured by the internal reflection technique. The reflected beam is a mixture of totally-reflected and partially-reflected waves, thus the name attenuated total reflection (ATR) technique.

3.2.2.2 Instrumentation

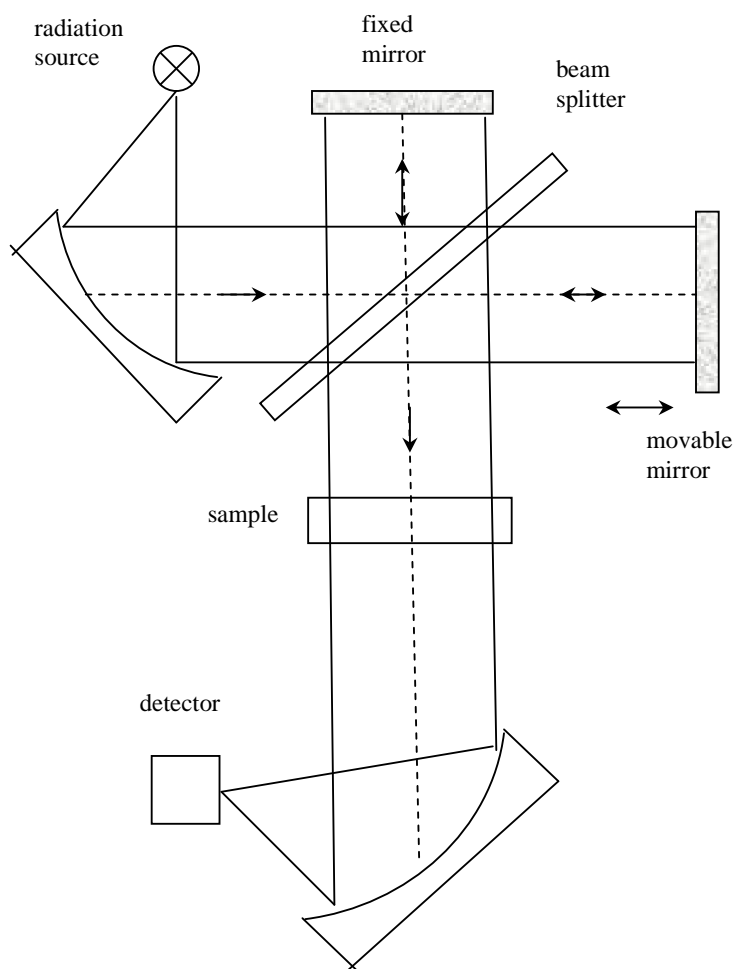


Figure 3.10 Schematic illustration of Fourier transform spectrometer with a classical Michelson interferometer

Early-stage IR instruments of the dispersive type used a prism or a grating monochromator. Hence slow scanning is characteristic of a dispersive instrument. A

Fourier Transform Infrared (FTIR) spectrometer obtains infrared spectra by first collecting an interferogram of a sample signal with an interferometer, see Fig. 3.10.

The beam of radiation from the source is split by a semi-permeable beamsplitter into two partial beams that are reflected on a fixed and on a movable mirror back to the beamsplitter where they recombine and are brought to interfere. The fraction directed back to the source is not used and gets lost. A shifting of the movable mirror changes the optical pathlength in this interferometer arm, whereby a phase difference between both partial beams results and, hence, a change of the interference amplitude. The intensity signal from the detector, as a function of the change of the optical pathlength corrected by a constant component, is called an interferogram. An FTIR spectrometer acquires and digitizes the interferogram, performs the FT function, and outputs the spectrum.

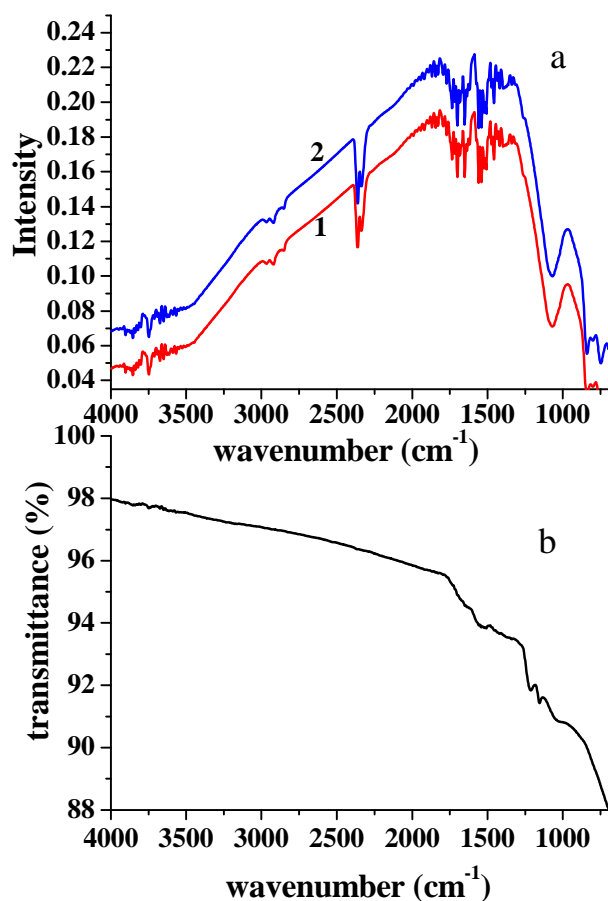


Figure 3.11 Calculation of the transmittance from sample and background single beam spectra.

- spectrum of sample 1 (shifted in the ordinate) and background spectrum 2 with air as reference
- quotient from both spectra

Normally single beam spectra, which occur primarily in the spectral measurement, are predominately calculated, whether it is with sample or as a pure background spectrum. It is necessary to measure the cited spectra consecutively, whereby the quotient of both gives the transmittance spectrum. The procedure is explained in Fig. 3.11.

3.2.3 Elemental Analysis

Elemental analysis is widely applied for determining the chemical composition of organics, as well as for carbonaceous materials such as activated carbons, carbon blacks. It is easy to operate, requires small amount of sample (in milligram range) and can give the content of C, N and H precisely. However, the shortage of this method is that it is destructive and has strict requirements on the sample – only powder samples can be analyzed.

3.2.3.1 Working principles

This method applies the combustion method. Samples are combusted in a pure oxygen environment, with the resultant combustion gases measured with a chromatograph.

The content of the elements are calculated based on the weight of sample, the corresponding peak area collected from the chromatograph and a factor K of the instrument:

$$C = \frac{K \times I}{W} \times 100\%$$

where, C = content of the element

I = peak area of the combustion product detected by chromatograph

W = weight of sample

K = constant, calculated from a standard material with a known elemental composition, such as acetanilide, benzoic acid, EDTA, etc. ($K = \frac{C_s \times W_s}{I_s}$, C_s

= percentage of the element in standard material, W_s = weight of the standard material, I_s is the area of the peak from the combustion product of the element in chromatograph)

The absolute error in the measurement is 0.3% by weight. Detection limits are generally 0.01 to 0.1%.

3.2.3.2 Instrumentation

Samples are packed into lightweight containers of oxidizable metal, which is normally tin or aluminium, and dropped into a vertical quartz tube, heated to 1050 °C; a constant flow of helium is maintained. The high temperature created by the flash combustion of the container ensures a complete decomposition of metal salts and other materials that are not easily decomposed. When the sample is introduced, the helium stream is temporary enriched with pure oxygen. Flash combustion takes place, primed by the oxidation of the container. The resulting combustion products pass through specialized oxidation reagents such as chromium oxide (CrO_3), to ensure the complete transformation from the carbon, hydrogen and nitrogen to carbon dioxide (CO_2), water (H_2O), nitrogen (N_2) and nitrogen oxides, respectively. These gases are then passed over copper to remove excess oxygen and to reduce the nitrogen oxides to elemental nitrogen; helium is used as the carrier gas. The gases are then introduced into the chromatographic column, heated to about 190°C. The individual components are separated, eluted in the order $\text{N}_2 - \text{CO}_2 - \text{H}_2\text{O}$, and measured by a thermal conductivity detector (TCD). A schematic diagram of the instrument can be seen in Fig. 3.12.

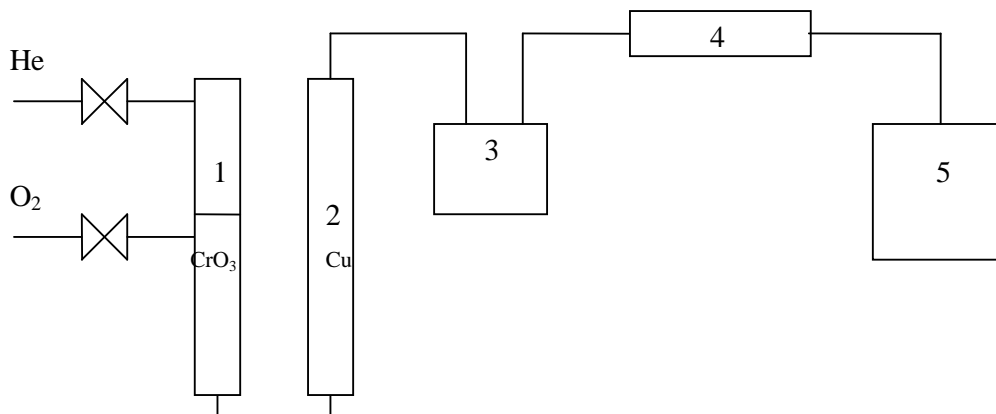


Figure 3.12 Schematic diagram of the instrument 1. combustion tube, 2. reduction tube, 3. mixing zone, 4. separation zone, 5. detector

Chapter 4

Experimental details

4.1 Sample preparation

4.1.1 Ageing of ultracapacitors

This part of work is completed in Epcos, Heidenheim, Germany. Electrode from Epcos is assembled into 200 F ultracapacitors as shown in Fig. 4.1. The electrolyte is tetrafluoroborate (TEATFB) in acetonitrile at approximate 1 M (battery grade) and paper separator is applied. The ultracapacitors are then put into ageing experiments at various direct current (DC) voltages and various temperatures as shown in Table 4.1.

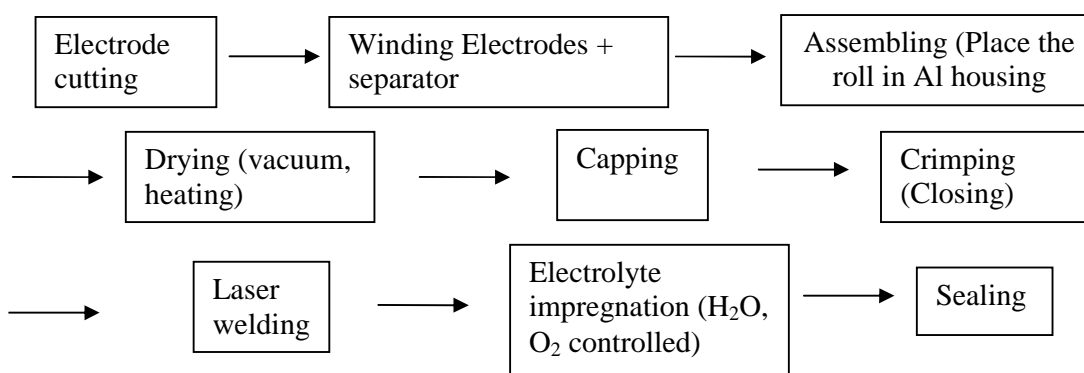


Figure 4.1 Processing procedures of ultracapacitors

About every 600 hours, the capacity and equivalent series resistance (ESR) are measured in Epcos by electrochemical impedance spectroscopy (EIS). The spectra are recorded with a PGSTAT30-FRA2 electrochemical analyzer (Autolab) in the frequency range from 1 kHz to 10 mHz at 0 V, 2.5 V at room temperature and -30 °C, respectively. The capacitance is calculated from the imaginary part of the complex impedance according to $C = -1/2\pi fZ''$. The value achieved from 2.5 V, room temperature at $f = 50$ mHz is taken as the capacitance for the ultracapacitors.

Afterwards, samples are sent to Max-Planck-Institute Stuttgart where the structural and chemical characterizations are carried out.

The ultracapacitors are torn up mechanically by a cutting tool. Electrodes are cut into small pieces at about 0.5×0.5 cm² (normally samples are taken from the middle part along the electrodes). The samples are immersed into a large quantity (appr. 10 ml for

each piece) of acetonitrile overnight to let the adsorbed salt diffuse out. Then the electrodes are rinsed by solvent (appr. 10 ml for each piece) with shaking for 10 to 12 times to remove the salt, and the results presented later prove these procedures are effective enough for the removal of salts. After the desalting samples are pre-dried in normal oven (60 °C) and then sent to vacuum oven to be dried at 80°C and appr. 10^{-3} Torr overnight to remove the water completely and sent to characterization.

Table 4.1 Ageing conditions of ultracapacitors

Code	Ageing conditions		
	Voltage(V)	Temp(°C)	Time (hours)
I	2.5	80	3048
II	2.3	80	3115
III	2.5	70	3700
IV	2.8	50	2919
V	2.3	70	2904
VI	2.5	50	2924
Reference sample	2.3	room temperature	24

4.1.2 Ageing of components for ultracapacitors

Three activated carbon samples provided by Epcos are chosen for ageing experiments, two (A and B) from natural precursors (coconut shell) and one (C) from synthetic resin. The manufacturing procedure refers to Chapter 2.

Three conductive agents provided by Epcos are chosen for ageing experiments, one acetylene carbon black sample (A-B); two ketjen blacks, Ketjen black A (K-A) and Ketjen black B (K-B). The precursors of the Ketjen blacks are unknown.

Chemical ageing

Powder samples are dried in vacuum oven at 80 °C and 10^{-3} Torr overnight and then transferred to a flow box (Kiki, Germany) purged with argon 5.0 (99.999 vol. %, water content 1 – 3 vpm and oxygen content 1-2 vpm). Normally it takes less than ten minutes for the transferring and the sample containers are sealed before being taken out of the oven to minimize the adsorption of water. Practically, the water and oxygen content might be higher than the defined value because of the contamination during transfer. We measured the water and oxygen content at the gas outlet of the flowbox, which indicated the water content is lower than 30 ppm and the oxygen content is

around 48 ppm. The technical parameters of the flow box can be found in Appendix I. In the flow box, the samples are immersed in acetonitrile (Merck, Germany, for DNA synthesis, max.10 ppm H₂O) and electrolyte, respectively. The ratio of the carbon to the liquid is about 1: 10 in volume. The flasks are tightly sealed by the caps and with Parafilm[®] (The Lab Depot, Inc., USA) further. Each sample is prepared 5 times in parallel in order to test for various time periods. Afterwards, they are taken out from the flow box and put in the temperature control box at 50 °C. Although this is considered to be a relative tight way, water and oxygen might permeate into the samples from ambience during the storage. Once a month the samples are taken out, immersed in salts are fully rinsed and the characterizations are carried out. The longest time is comparable to the ageing time for the electrodes for about half a year. During the experiment, no significant solvent loss is observed.

Electrochemical ageing

Activated carbon powder samples are dried first in the vacuum oven at 80 °C and 10⁻³ Torr overnight to remove the adsorbed water and then transferred to argon flow box. Then they are assembled directly in a Swagelock type (two electrodes) lab cell as shown in Fig. 4.2 without binders and conductive agents, neither without any extra container and polarized at 2.9 ± 0.1 V DC voltage for 45 days. The voltage is controlled by a DC power supply and monitored with a digital voltmeter.

After the ageing is completed, the powders are taken out, separated into anode and cathode according to the polarization – since the powders are loose and fluffy, there is always mixing of the powder from anode and cathode.

The powders are rinsed by acetonitrile in ultrasonic bath for half an hour and then sent to centrifugal separation at 15000 rpm for 10 minutes. The supernatant is carefully taken out to reduce the possible particle loss. The supernatant for the first time centrifugation is collected and analyzed by IR spectroscopy later. The rinsing and separating process is repeated for 6 to 8 times to let the adsorbed salt totally rinse off. The desalted powders are dried first in normal oven at 60 °C for 5 to 6 hours and then put into the vacuum oven to be dried at 80°C, appr. 10⁻³ Torr overnight to remove the water and then sent to characterizations.

The experimental procedure for pure conductive agents is identical to that for activated carbons.

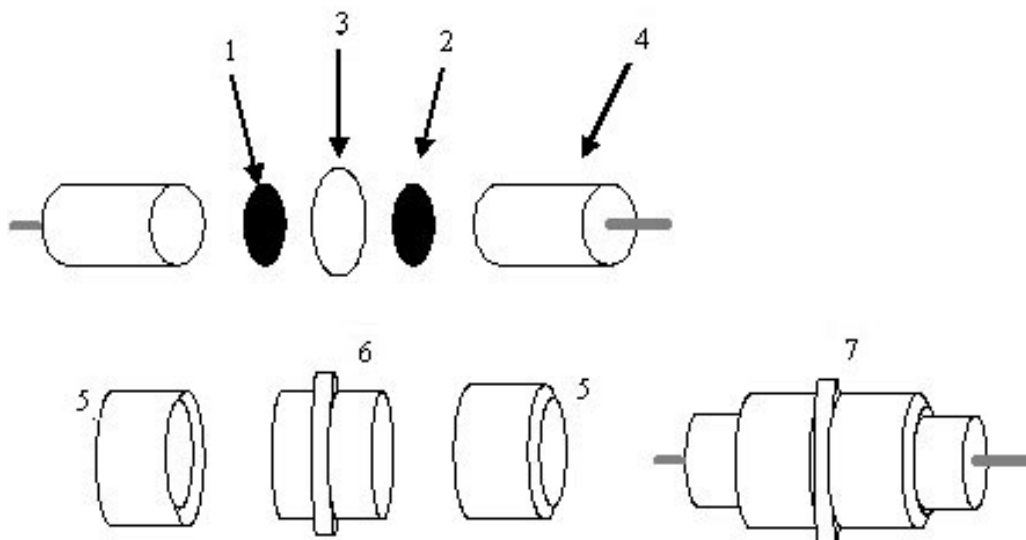


Figure 4.2 Schematic drawing of Swagelock type labcell – 1. working electrode 2. counter electrode 3. paper separator 4. current collector (Al foil) 5 and 6. Swagelock fittings (stainless steel) – tube: bored through for tubing and tubing connection 7. assembled labcell; Mylar[®] film fitted to the inner walls of 5 and 6 to avoid the contact between 5, 6 and 4.

4.2 Structural characterization

4.2.1 Porosimetry

77 K N₂ isotherms are measured with a porosimeter (Autosorb-1, Quantachrome, USA).

Since the length of the corresponding sample cell (glass tube) is too long for a normal electronic balance, a 3 mm(Ø) * 10cm (L) quartz tube is specially made. Samples are first put into the small tube and weighed to reduce the error from weighing. Thereinafter the small quartz tube is put into a Quantachrome 9 mm (Ø) glass sample tube for outgassing and measurement.

In the present work, most of the samples are fine powder and have the problem of elutriation, which means the loss of powder out of the sample cell. This is caused by too rapid a gas flow out of the cell. The most serious problems are encountered during the outgassing procedure to degas the moist, “light” powders, which normally requires heating and evacuating. As the sample heats from ambient, the pressure over the sample decreases due to the action of the vacuum. At some point the water “flashes” into steam. This rapid expansion of gas volume drives powder out of the bulb and up the stem of the cell. The trapping of the powder will cause the corrosion of the gaskets and bring about leakage problems.

To prevent the elutriation, several measures have been adopted:

- Wide diameter cell tube of Φ 9 mm is applied;
- A glass fibre bundle is put at the outlet of specially made small quartz tube to firstly stop the powder;
- Special filter with fine Pt fibre inside designed by Quantochrome is applied. This filter is normally tightly clamped at the outlet of the Φ 9 mm sample cell. After several times measurements, the filter is cleaned with ethanol in ultrasonic bath to remove the trapped powder.
- Outgassing temperature is first set to 60 °C for about 6 hours and then increased to 150 °C to prevent “flash” generation of water vapour which blows the sample out of the cell.

Normally the outgassing time is 24 hours. The samples are refilled with nitrogen after outgassing and weighed again to calibrate the weight in order to reduce the error from water and air adsorbed in original sample and the possible mass loss during outgassing. This takes 2 to 5 minutes and then the sample is sent to measurement.

The specific surface area of the samples is calculated with 5 point BET in the range from $P/P_0 = 0.01$ to 0.1. Calculations with DR and DFT models are carried out with the software Autosorb[®] (Quantochrome, USA).

4.2.2 Raman spectroscopy

Raman spectra are obtained with a Labram 010 spectrometer (Jobin Yvon Horiba, France) using the 632.8 nm He-Ne line as an excitation source. The laser power is 4 mW and the slit width is set to 100 μ m. Raman spectra from 500 to 4000 cm^{-1} at about 1 cm^{-1} interval were measured for 100s in the backscattering geometry with a single monochromator. The detector is a charge coupled device electronically cooled. To improve the signal-to-noise ratio, 5 scans were averaged.

Electrode samples are directly loaded on microscope slides. Powder samples are pressed to densely attach to microscope slides. This method is proved to be not sensitive to the interference of water.

The obtained Raman spectra are first calibrated by polynomial baseline subtraction by the Labram software, which is proved to be well reproducible. The deconvolution is carried out with five Lorentzian shape peaks on top of linear background in the region from 800 to 2000 cm^{-1} in Origin 7.5, as described later.

4.3 Chemical composition characterization

4.3.1 Elemental analysis

CHN analysis was performed on a Perkin Elmer Analyzer 240 at the University of Stuttgart. The samples are rinsed and dried in vacuum oven at 80 °C and $\text{appr.}10^{-3}$ Torr before being sent to measurement. The samples are carefully sealed by Parafilm[®] to prevent the interference from water. And the time interval between drying and measuring is tried to keep as short as possible to minimize the problem from contamination, however it still takes several hours which is relatively longer than other methods.

This method requires powder samples to avoid the errors from incomplete combustion and inhomogeneity. The activated carbon layers from electrodes are cut into small pieces (less than 1 mm²), to satisfy these requirements.

4.3.2 Infrared analysis

Infrared spectra were collected on a Equinox 55 infrared spectrometer (Bruker, Germany) with a Globar mid infrared source and a deuterated triglycine sulfate (DTGS) detector. An ATR configuration (PIKE Miracle) with a germanium crystal as the internal reflection element (IRE) is applied. Detailed parameters of the IR spectrometer can be found in Appendix II.

The sample chamber is continuously purged with argon 5.0 (99.999 vol.%) at the rate of $\text{appr.} 4 \text{ l/min}$ to reduce the interference of water and carbon dioxide. 2000 scans are added at a resolution of 8 cm^{-1} .

Between two measurements, the Ge crystal is cleaned by water, wiped with soft lens paper and dried for 10 minutes. A pressure is loaded to guarantee the good contact between the sample and Ge crystal. To prevent the fluctuation of the pressure, the pressing tool (stamp) on the ATR configuration is recommended to be set at a fixed height value and not to change.

The transmittance spectra are generated from raw spectra collected with samples referenced to the raw spectra of air.

To distinguish the difference of the outmost surface and the inner part of the electrodes, the samples are stripped with adhesive tapes and analyzed with IR layer by layer (approximately 30-40 μm per layer, which is estimated from the times of stripping to totally remove the activated carbon layer at the thickness of 100 μm).

4.3.3 XPS analysis

XPS characterization of the surface composition and chemistry has been carried out on a AXIS HSi 165 and Ultra spectrometer (Kratos Co., UK) using Al K α radiation (energy: 1486.6 eV). An X-ray power of 150 W (15 kV, 10 mA) was used for all analyses. The base pressure in the sample analysis chamber is 10^{-9} to 10^{-10} Torr.

Right after drying, samples are sent to the instrument to transfer to antechamber. The spectra obtained indicated there is no interference from water, which normally shows a O1s peak at 535 – 536 eV.

Electrode samples are directly fixed on the sample holder, while the powder samples are pressed on an Indium foil (by an agate press) and then fixed on the sample holder. The photoelectron surface area (spot size) is around 1 mm².

Survey spectra (1200 eV to -5 eV) were recorded with the pass energy of 80 eV and the narrow scans for F 1s, O 1s, N 1s, C 1s were recorded with the pass energy of 20 eV.

The samples were sputtered off for appr. 20 nm by an argon ion gun to remove the possible contamination, which normally occurs during sample preparation and sample loading. The spectra show obvious changes, especially for the content of elements, in the first 10 nm sputtering. The converging is observed after the sample is sputtered off for appr. 20 nm, see Appendix III.

For the electrode samples, charging effect is apparent because of the high thickness and low conductivity so that the neutralizer was applied to reduce the charging effect. The neutralizer is a tungsten fibre heated to emit electrons, which can compensate the positive charges accumulated on the surface because of the loss of electrons. The powder samples do not have this problem because of the low thickness of the carbon powder and good conductivity of the indium.

Quantification is done by means of the relative elemental sensitivity factor method which uses the sensitivity factors referenced to F 1s, determined experimentally from many compounds with defined stoichiometry.

The curve fitting of C 1s, N1s, O 1s, F 1s envelopes is carried out with a mixed Gaussian (30%) – Lorentzian (70%) component profiles after subtraction of a so-called Shirley background with the CasaXPS processing software. All peak positions are calibrated with the graphitic carbon peak at 284.6 eV.

Chapter 5

Influences of ageing conditions

As described in Chapter 4, ultracapacitors are aged under various ageing conditions and ageing time, thereby they show various capacity and ESR deterioration. According to the capacity after ageing, the samples are encoded from I to VI for the severity of ageing. The severity decreases with the number increase in turn.

Table 5.1 Sample coding and the ageing condition

Code	Ageing conditions		
	Voltage(V)	Temp(°C)	Time (hours)
I	2.5	80	3048
II	2.3	80	3115
III	2.5	70	3700
IV	2.8	50	2919
V	2.3	70	2904
VI	2.5	50	2924

The capacity loss for each sample is shown in Fig. 5.1. According to the impedance spectra, the ESR of sample I and II increase several magnitudes compared to new capacitors and the data are not applicable anymore, so only samples III to VI are included.

It is known that high voltage and temperature can both speed up the ageing, and in ultracapacitor field there is an empirical regulation based on propylene carbonate (PC) electrolyte that 10 K or 0.1 V increase cuts life time by half . [Hahn04] In this case, life can be calculated as:

$$L = L_0 \times \left(\frac{1}{2}\right)^f$$

$$f = \frac{(T - 298K)}{10} + \frac{(V - 2.3V)}{0.1}$$

where, L = the lifetime of the capacitors investigated

L_0 = the lifetime of the capacitors applied at 2.3V and 298 K

f = the ageing factor, which can be calculated as shown above

T = the ageing temperature (K)

V = the ageing voltage (V)

If following this relationship, in our case, sample I and IV, V and VI should have experienced similar ageing and have the compatible capacity loss and ESR increase. And the order of ageing would have been $I = IV > III > II > V = VI$. Apparently, as shown in Fig. 5.1, the order of ageing is not well consistent with this.

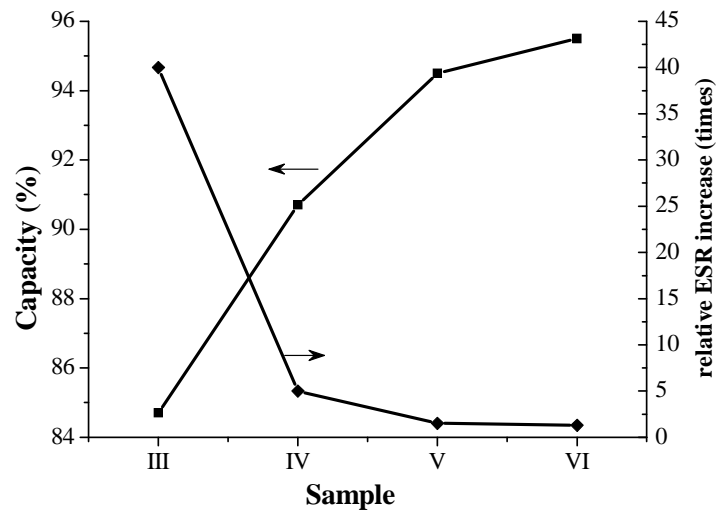


Figure 5.1 Capacity (as the ratio to the capacity of ultracapacitors not aged) and relative ESR increase for samples experienced various ageing conditions

This discrepancy is possibly due to the evaporation of acetonitrile (boiling point 82 °C at 1 atm). When the temperature increases, the acetonitrile starts to evaporate in the closed system and will result in the accumulation of the internal pressure. Normally there is pressure release apparatus in ultracapacitors and the accumulation of pressure might blow it open. In this case, the ultracapacitor becomes and remains a relatively open system and the evaporation speeds up and the electrolyte permeates out further. In some extreme cases, white deposit crystals from electrolyte salt can be observed on the aged ultracapacitors. Some work was carried out in Epcos and tried to calculate the internal pressure value, since the real volume is hard to evaluate for ultracapacitors based on activated carbons no reasonable value could be reached.

The weight loss of the ultracapacitors after ageing is given in Fig. 5. 2, which indicates sample I and II both aged under 80 °C, have much higher weight loss than others. The weight loss might come from the solvent evaporation as well as gas

evolution from electrochemical reaction (details see Chapter7), however, the contribution from the latter one might be much less than the former one. The loss of solvent will directly cause the conductivity loss and ESR increasing. In this case, the deterioration of the properties of the ultracapacitors will follow a third ageing mechanism besides temperature and voltage, which is electrolyte depletion. However, when the temperature condition does not reach the extreme, the influence from voltage becomes obvious as shown in the results above.

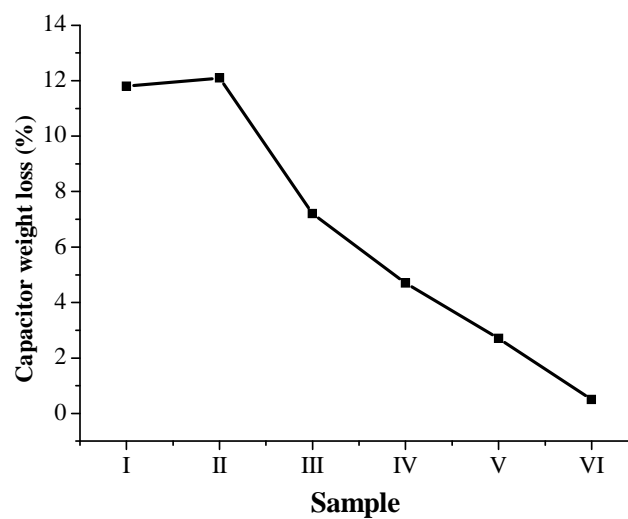


Figure 5.2 Weight loss of samples experienced various ageing

Chapter 6

Ageing effects on the electrodes of ultracapacitors

In this chapter, the results collected from new electrode (without any contact with the electrolyte and treating) and aged electrodes from the ultracapacitors aged under various conditions are presented and discussed. Microstructural changes are characterized by porosimetry and Raman spectroscopy; chemical composition changes are characterized by the elemental analysis, XPS and IR spectroscopy.

6.1 Microstructural changes of electrodes

6.1.1 Pore structure changes – porosimetry

High specific area is considered to be one of the most important advantages for the activated carbons applied for electrochemical double layer capacitors. A lot of work has been aimed at finding the relation between the specific area and the double layer capacitance of carbonaceous materials.

Theoretically, the higher the specific area of the electrode is, the higher the double layer capacitance. However, the situation is far more complicated. Earlier work showed that there is no linear relation between the capacitance and the surface area while the pore size distribution is even more important. [Shi95, Qu98, Shirashi02, Salitra00, Endo01, Endo02, Tamai03, Lozano-Castellós03, Gryglewicz05, Tamail05]. An important factor is the accessibility of micropores to the electrolytic medium. The results show that the electrochemical double layer capacitance depends largely on the pore size and unhindered movement of ions in pores. Qu and Shi [Qu98] found that the DFT pore size distribution can be taken as one of the key factors that dictate the selection of activated carbon material for ultracapacitors.

In the present work, N_2 adsorption isotherms of the electrodes from ultracapacitors aged under various conditions are measured. The relation between the double layer capacitance, BET specific area, micropore volume and pore size distribution is primarily discussed. To avoid the deviation brought from the inhomogeneity, data from two to three samples from each capacitor are collected and compared. More is not feasible, because the measurement is very time consuming. Moreover, relative

rather than the absolute values are taken as the index for comparison to further remedy the deviation.

6.1.1.1 Specific area and pore volume changes with ageing

The N_2 adsorption isotherms of the electrodes from the ultracapacitors aged at various conditions do not show significant differences in shape and adsorptive capacity. So only the comparison between new electrode (without any contact with the electrolyte or any other treatment) and aged electrodes from one of the aged ultracapacitors are shown in Fig. 6.1 (from Cap III). The isotherms are of type I, as introduced in Chapter 3, which means the electrodes keep their microporous structure after ageing. The measurement of a reference sample (polarized only for 24 hours) indicates there is no obvious decrease in BET specific area and pore volume in both anode and cathode compared to the new electrode, which means the rinsing procedure is effective, furthermore short term polarization has little effect on the pore structure of electrodes.

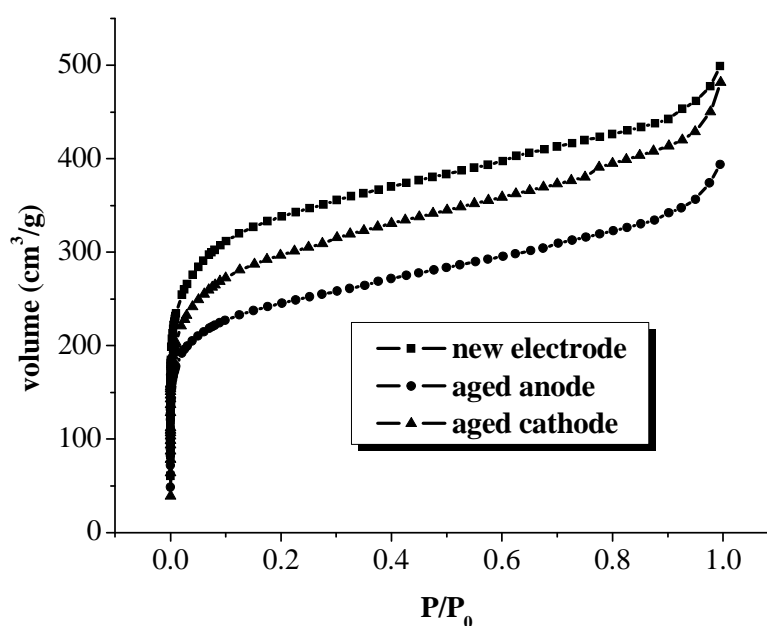


Figure 6.1 77 K N_2 adsorption isotherms of new and aged-electrodes

The porosity characteristics of the materials measured are listed in Table 6.1. The pore volume is calculated by DFT taken as the total volume; the specific area (S_{BET}) is calculated with the BET method within a range of relative pressure P/P_0 from 0.01 to 0.1 (micropore range). The volume (V_{mic}) and surface area (S_{mic}) of the micropores are calculated with the DR model. The introduction of these models refers to Chapter

3. The porosity change (loss of pore volume, micropore volume, micropore specific area and BET specific area) is plotted versus the change of capacity in Fig. 6.2 to give a clearer indication of the ageing.

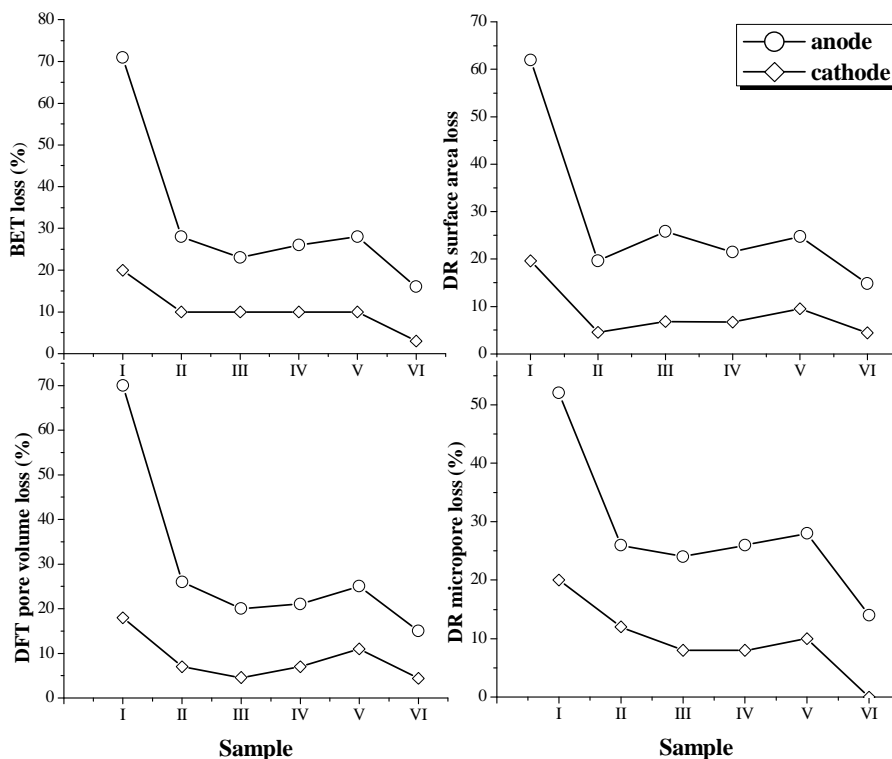


Figure 6.2 Pore volume and specific area loss of aged anodes and cathodes

As already mentioned in Chapter 3, in a strict sense, the BET method is not applicable to microporous adsorbents. Micropores allow only 1 to 2 layers to adsorb (see Fig. 2.8), so there is no real multilayer adsorption. Pore filling is usually completed at relative pressures below 0.1, and linear BET plots are found at even lower relative pressures. In this case the obtained BET surface area does not reflect the true internal surface area, but should be considered as “characteristic or equivalent BET area”. [Lowell04] In the present work, the range of linearity for the BET plots is below 0.1, and five values in the range from 0.01 to 0.1 are taken for the BET calculation.

The results in Table 6.1 show that the BET method underestimates the specific area of materials compared to the DR method based on micropore filling mechanisms. The DR method was for a long time considered to be a good way to postulate the micropore filling process for activated carbons, and linear DR plots over a large relative pressure range can be found for a number of microporous carbons. However,

the interactions of the adsorbate molecules with the porous material and their impact on micropore filling (and thus on the shape of the adsorption isotherm) are not considered in the DR model. When the adsorbent is highly inhomogeneous, the DR plots will deviate from linearity, thus the estimation of micropore volume and pore size distribution from that will be inconsistent. However, in the present study, it is observed that the linearity of DR plots from the activated carbon layers deviates not much, which proves the availability of this method and the homogeneity of the materials. Furthermore, the disadvantages of the BET method and DR model can be overcome by applying modern methods such as DFT (of statistical mechanics). It is widely used and considered to be one of the most accurate methods for size analysis of micro- and mesopores. [Lastoskie93, Neimark97, Neimark98, Jagiello04]

Table 6.1 Porosity characteristics of electrodes

Sample		S_{BET} (m ² /g)	S_{DR} (m ² /g)	V_{mic} (cm ³ /g)	V_{total} (cm ³ /g)
New electrode		1264	1297	0.46	0.59
I	anode	480	493	0.18	0.26
	cathode	1019	1043	0.37	0.48
II	anode	972	1043	0.37	0.44
	cathode	1140	1238	0.44	0.54
III	anode	911	962	0.35	0.43
	cathode	1115	1209	0.43	0.52
IV	anode	930	1019	0.36	0.43
	cathode	1141	1210	0.43	0.54
V	anode	910	976	0.35	0.42
	cathode	1127	1174	0.42	0.52
VI	anode	1061	1105	0.39	0.50
	cathode	1218	1240	0.44	0.59

From the data in Table 6.1 and Fig. 6.2 it can be found that, although the DR method and BET method give different absolute values for the specific area, the ratios of the specific area loss for the aged samples, calculated with both methods, are similar.

The data in Table 6.1 and Fig. 6.2 demonstrate that aged anodes suffer a higher pore volume loss and surface area loss than cathodes. But neither the specific area loss nor the pore volume loss can be correlated to the capacity deterioration quantitatively in a straightforward way. From the data it can also be seen that in a certain range, between

the more seriously aged sample (II) and less aged sample (VI), the pore characteristics are not very different. This hints that pore volume and specific area loss are only two of the factors influencing the capacity of ultracapacitors.

6.1.1.2 Pore size distribution changes of the electrodes with ageing

Pore size distribution histograms are calculated by the DFT model in the relative pressure range from 7.7×10^{-6} to 0.7, which corresponds to the pore size range from 0.5 to 5 nm. The relative abundance of pores of the various pore width ranges (so called pore content in the histogram and described by the percentage of the volume of the pores in certain pore size range versus the total pore volume) can be read easily (see Fig 6.3). The histogram describes the possible distribution of pores in each size range but not for precise pore widths, thus is considered to be more objective than the pore size distribution line (which describes the distribution of the pores with precise width). A minimum at about 1 nm can always be found in DFT pore size distribution. This feature has been observed in many studies for a number of carbon materials and is attributed to the fact that the pore model used in the DFT calculations does not adequately represent actual activated carbons.* [Jagiello04, Jagiello98, Olivier97]

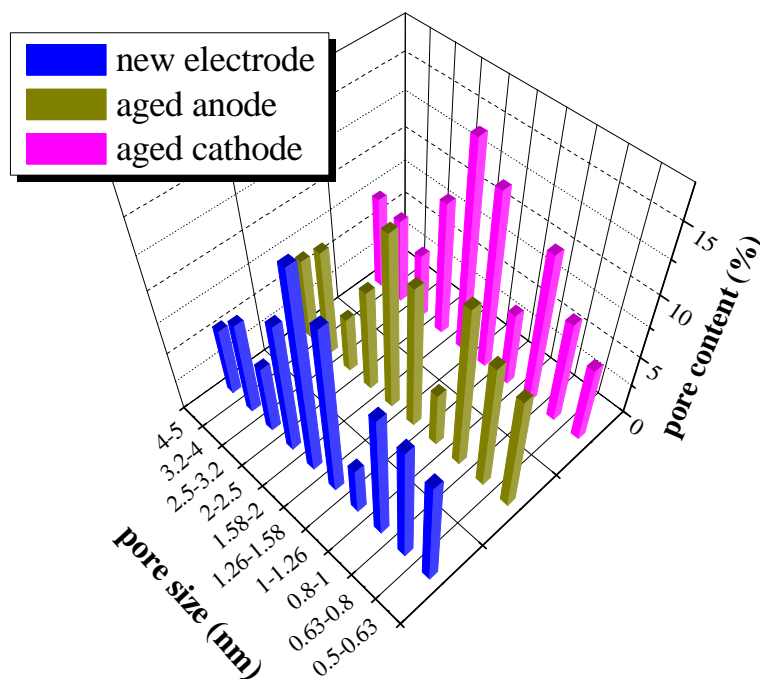


Figure 6.3 DFT pore size distribution histogram comparison of new electrode and aged anode and aged cathode

The electrochemical capacity (the capacity of new ultracapacitors set as 100%) is plotted versus the content of pores in various pore size ranges in anodes and cathodes in Fig. 6.4. The original pore size distribution histogram was divided into ten size ranges (for mathematic reasons): 0.5 - 0.63 nm, 0.63 - 0.79 nm, 0.79 - 1nm, 1 - 1.26 nm, 1.26 - 1.58 nm, 1.58 – 2.0 nm, 2.0 – 2.5 nm, 2.5 - 3.2 nm, 3.2 – 4.0 nm, 4.0 - 5.0 nm. In some of these ranges the relation between the capacity loss and pore content is very similar and can be combined. This is why the pore size ranges are different for aged anodes and cathodes in the plots in Figure 6.4.

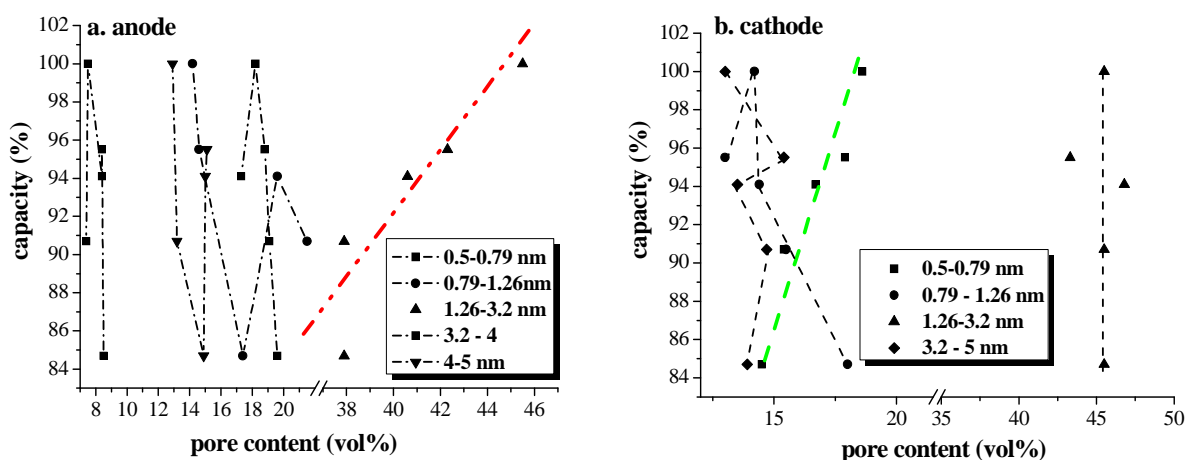


Figure 6.4 Relation of the electrochemical capacity and pore size distribution

The data show that, in anodes, pores with sizes in the ranges of 0.5 – 0.79 nm, 0.79 – 1.26 nm and 4 – 5 nm show no correlation with the capacity, while the content of the pores with widths in the range of 1.26 to 3.2 nm can be correlated to the electrochemical capacity quite well. In other words, ageing decreases the content of the pores in this size range. In cathodes, the amount of pores between 0.5 and 0.79 nm decreases with ageing, but much less than the decrease of the pores in the range of 1.26 to 3.2 nm for the anodes. The content of pores of larger than 1.26 nm does not change much with ageing. For pores from 0.79 to 1.26 nm, the relation of the pore content change and capacity change follows no obvious rule.

There are only a few investigations dealing with the relation of pore characteristics of activated carbon and ultracapacitor capacitance and the results do not agree. Theoretically, the pore size should be as large as possible to allow for maximum kinetics, which is important for the power performance of the ultracapacitors; at the same time the specific area should be high enough to facilitate maximum adsorption

for capacitance formation, which is important for the energy performance. An optimal combination of these two parameters is of course desired. It was estimated that only pore diameters larger than 5 nm may be useful in nonaqueous electrolytes. [Kinoshita95]. However, Japanese industry data [Endo02] emphasize that the pore size within the range of 3 – 4 nm is suitable for ultracapacitors with tetraethylammonium tetrafluoroborate (TEATFB) in propylene carbonate (PC). Endo et al. [Endo01] found that a pore around two to three times larger than that of the electrolyte ions should be the most suitable pore size for allowing a high capacitance. In their later work, diameter of Et_4N^+ and BF_4^- were calculated to 0.74 nm and 0.49 nm, respectively. These values are comparable with Ue's calculation of the molecular radii of Et_4N^+ and BF_4^- , which were 0.342 nm and 0.218 nm, respectively. [Ue94] Therefore, as Endo's assumption, the pores with size between 1 to 2 nm should be more important. Later, Endo et al. tried to take into account the solvation of PC and calculated solvated cation and anion diameters of 1.96 nm and 1.71 nm, respectively. Based on these results and on the assumption that the cation solvation size will be the rate determining factor, they suggested that pore sizes between 1 to 2 nm are crucial and govern the capacity of ultracapacitors with TEATFB in PC. [Endo02] Although the values are quite consistent with their first assertion, it is not easy to understand from their data how solvated ions with diameters of almost 2 nm can move freely in pores with the diameter of only 1-2 nm. Up to now, there is no conclusive result available for the optimal pore characteristics for the electrolyte containing TEATFB in PC. Few investigations have been carried out based on ultracapacitors with TEATFB in acetonitrile.

The data from this work indicate that on the anode the loss of pores in the size range of 1.26 to 3.2 nm can be correlated with the capacity loss quite well. This can be interpreted as the pores of size from 1.26 to 2 nm being preferable for the movement of the ions without solvation shell, while pores in the size range from 2 nm to 3.2 nm are suitable for the solvated ions.

When the ultracapacitors are aged, electrochemical processes occur on the anode, as will be discussed in the chemical characterization part, and relatively large molecules form on the anode. In this case, some of these pores are blocked and not approachable for the ions anymore, thus results in the capacity loss. In comparison, the blocking at the cathode is less significant.

It is known that ultramicropores (with widths smaller than 0.7 nm) are not important for ultracapacitors because they are too small for the ions to move in. [Shi95, Qu98, Salitra00, Shiraishi02, Endo01, Endo02, Tamai03, Lozano-Castellós03, Gryglewicz05, Tamai05] For aqueous electrolyte system such as sulfuric acid or potassium hydroxide, it was proposed that micropores larger than 0.5 nm were utilizable at sufficiently low charging and discharging rate [Shi95]. However, this condition will never be fulfilled in real application so the minimum size should be larger. For nonaqueous systems such as tetraalkylammonium tetrafluoroborate in propylene carbonate (PC), according to the earlier discussion the minimum utilizable pore size can be considered to be 1 nm.

Based on these assumptions, the loss of pores in 0.5 – 0.79 nm range in the cathodes should have little contribution to the capacity loss. The loss of these pores can also be attributed to the pore blockage – at negative potentials, Et_4N^+ cations move into these pores and are blocked there because of the spatial confinement. Theoretically they can move out, but kinetically this process is very slow and this kind of blockage accumulated gradually with ageing (technical operation is always facilitated by slow charging and fast discharging).

6.1.2 Microcrystallinity changes – Raman spectroscopy

Raman spectroscopy is a promising method for characterization of highly disordered materials like activated carbons, because it is sensitive not only to crystal structures but also to molecular structures (and therefore to “short-range order” of the atoms in a molecule). The Raman signals of graphite crystals result from lattice vibrations and are very sensitive to the degree of structural disorder. The spectrum of near-ideal graphite, which is observed for large single crystals and highly oriented polycrystalline graphite (HOPG), significantly differs from the Raman spectra of disturbed graphitic lattices, such as polycrystalline graphite or boron-doped HOPG, see Fig. 6.5. [Mapelli99]

Theoretical calculations show that each of the first-order Raman bands visible in spectra of highly ordered and disordered graphites can be attributed to a vibrational mode of the ideal graphitic lattice. For an ideal graphitic crystal only a few of these vibrational modes are Raman-active, see Fig. 6.6. [Nemanich79, Al-Jishi82, Wang90, Nemanich77]

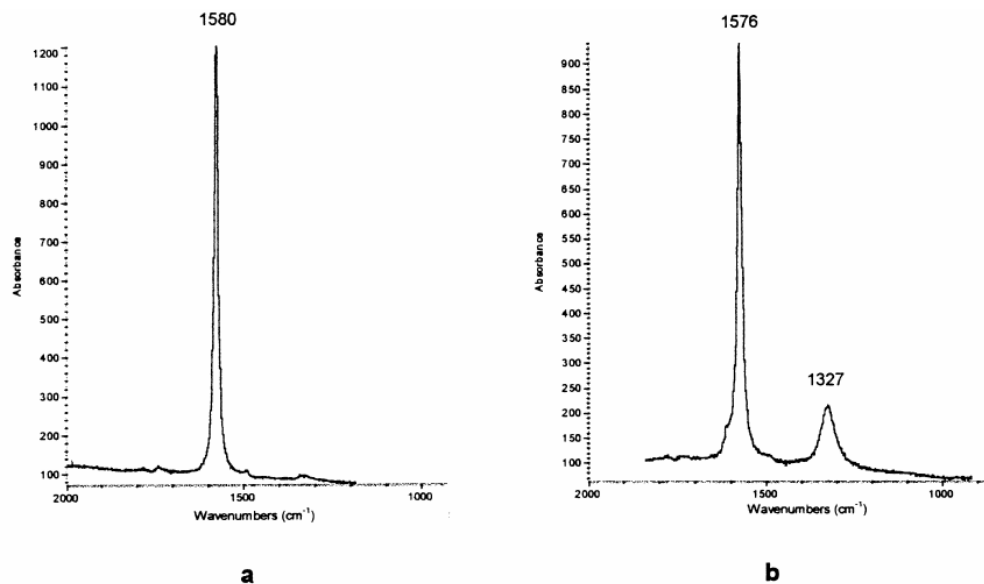


Figure 6.5 Raman spectra from: a. single crystalline graphite b. polycrystalline graphite

In case of structural disorder, some ideally forbidden vibrational modes can become Raman active. The first-order bands (D or “Defect” bands) are known to be characteristic for disordered graphite, and to grow in intensity relative to the G band with increasing degree of disorder in the graphitic structure.

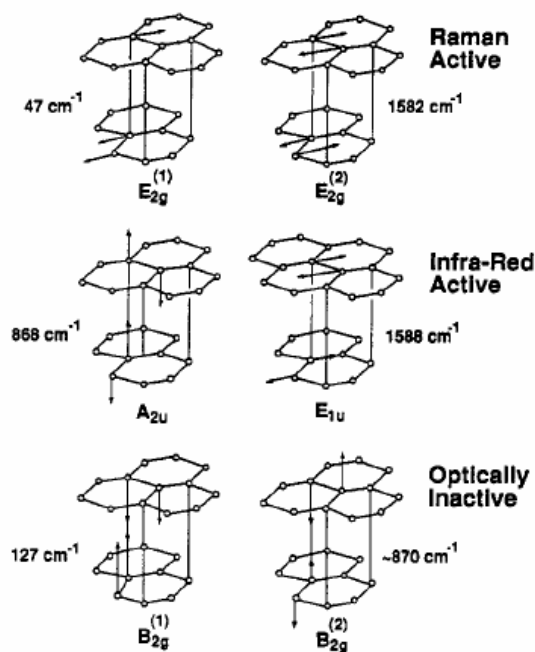


Figure 6.6 Vibration mode in graphite crystal

The most intense is the D_1 band, which appears at appr. 1360 cm^{-1} and corresponds to a graphitic lattice vibration mode of A_{1g} symmetry with “breathing” character. The D_1 band has been suggested to arise from the reduced symmetry of the graphite lattice near edges or near a heteroatom in case of doped graphite. Moreover, this band has been observed in Raman spectra taken on the edge planes (perpendicular to the graphene layers) of large graphite single crystals and of HOPG. Thus, in polycrystalline carbonaceous materials, consisting of large numbers of small graphitic crystallites, carbon atoms at the edges of graphene layers are considered as the most probable origin of the D_1 band [Katagiri88, Wang90]. Another first-order band accounting for structural disorder is the D_2 band at about 1620 cm^{-1} , which can be observed as a shoulder on the G band. The D_2 band was assigned to a lattice vibration analogous to that of the G band with E_{2g} symmetry, but involving graphene layers at the surface of a graphitic crystal, i.e. graphene layers which are not directly sandwiched between two other graphene layers. Indeed, it was observed to replace the G band in intercalation compounds. [Dresselhaus82, Dresselhaus81]

Various carbonaceous substances were investigated in earlier studies, such as different types of graphite, amorphous and graphitic carbon films, diamond films, glassy carbon, coal, pitch and coal fibres, activated carbons, fullerenes and carbon nanotubes [Tuinstra70, Lespade84, Mernagh84, Katagiri88, Wang90, Cuesta94, Sze01, Ramsteiner87, Robertson86, Knight89, Wagner89, Nakamizo74, Garrell91]. Sadezky et al. summarized the results from earlier work in their recent publication, as shown in Table 6.2 [Sadezky05].

Earlier work indicates that the relative intensities of both the D_1 and D_2 bands increased with increasing excitation light wavelength (λ_0) and the frequency of the D_1 band shifts with the excitation energy at a rate of 40 to $50\text{ cm}^{-1}/\text{eV}$ over a wide excitation energy range. [Vidano81, Wang90, Sood98, Póscik98, Baranov87, Katagiri88] These phenomena are still not well understood and brought various explanations, and in general can be attributed to a disorder-induced double resonance effect (see Chapter 3). However, there is no consensus on its origin. [Mathews99, Thomsen00, Vidano81, Baranov87, Katagiri88]

Table 6.2 First-order Raman bands and vibration modes reported for carbonaceous materials (vs = very strong, s = strong, m = medium, w = weak) [Sadezky05]

Band ^a	Raman shift (cm ⁻¹)			Vibration mode ^b
	Non-graphitizable carbon	Disordered graphite ^c	Highly ordered graphite ^d	
G	~ 1580 cm ⁻¹ , s	~1580 cm ⁻¹ , s	~1580 cm ⁻¹ , s	Ideal graphitic lattice (E _{2g} -symmetry)
D ₁ (D)	~ 1350 cm ⁻¹ , vs	~ 1350 cm ⁻¹ , m		Disordered graphitic lattice graphene layer edges, A _{1g} symmetry)
D ₂ (D')	~ 1620 cm ⁻¹ , s	~ 1620 cm ⁻¹ , s		Disordered graphitic lattice (surface graphene layers, E _{2g} -symmetry)
D ₃ (D'',A)	~ 1500 cm ⁻¹ , m			Amorphous carbon (Gaussian or Lorentzian line shape)
D ₄ (I)	~1200 cm ⁻¹ , w			Disordered graphitic lattice (A _{1g} symmetry), polyenes, ionic impurities

^a Alternative band designations of earlier studies are given in brackets

^b Lorentzian line shape unless mentioned otherwise

^c Polycrystalline graphite (< 100 nm) and boron-doped HOPG

^d Single graphitic crystal (> 100 nm) and HOPG

6.1.2.1 Raman spectra of new and aged electrodes

Raman spectra of electrodes from aged ultracapacitors do not show a clear relation with ageing conditions, or, ageing degree. Basically, all the spectra of the anodes aged under various ageing conditions from I to VI almost overlap and the same is true for the cathodes. Although there are small differences in the relative intensities, they are in the range of error of this method.* Here we take the result from one sample as an example.

Fig. 6.7 shows typical Raman spectra observed for new and aged activated carbon layers of electrodes, excited at $\lambda_0 = 632.8$ nm (1.96 eV). The first-order spectra generally exhibit two broad peaks with intensity maxima around 1316 cm⁻¹ and around 1596 cm⁻¹. Above 2000 cm⁻¹, some weak bands are visible.

As discussed above and summarized in Table 1, the structure and Raman spectra of activated carbon layers in the present work can be interpreted in terms of highly disordered graphitic structures. The intensity maxima at 1316 cm⁻¹ and 1596 cm⁻¹ as D₁ and G bands are analogous to those of graphite. The D₁ band appears at 1316 cm⁻¹,

but not at the above-mentioned value at around 1350 cm^{-1} , because the laser wavelength in the present study is 632.8 nm , different from the laser wavelength in earlier studies [Cuesta94, Sze01, Garrell91], normally 514 nm (2.4 eV).

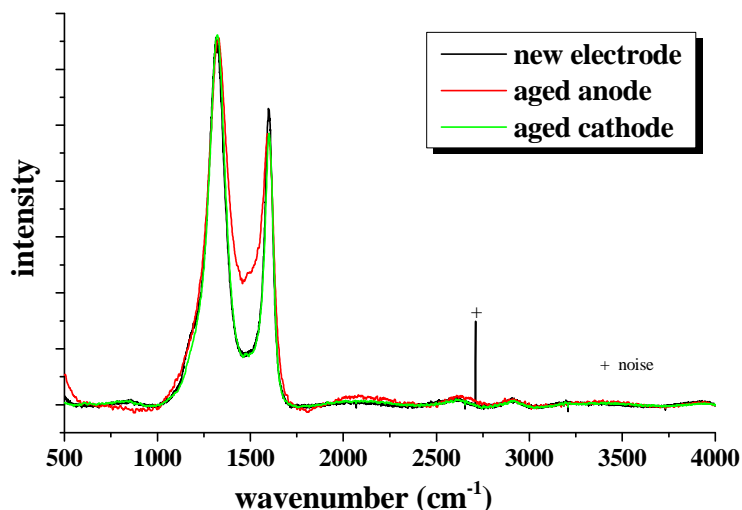


Figure 6.7 Raman spectra from new and aged-electrodes

Cuesta [Cuesta94], Jawhari [Jawhari94] and Sze [Sze01] suggested, that the peak at around 1596 cm^{-1} comprises not only the G, but also the D_2 band, known from graphitic lattices, but only Sze [Sze01] and Sadezky [Sadezky05] included it in spectral analyses by curve fitting. We also include the D_2 band in the curve fitting, and present it below as a clear support for the presence of the D_2 band.

Raman spectra from aged anodes show a higher valley at around 1500 cm^{-1} than that of new electrodes and aged cathodes. The high valley between the G and D_1 peak can be attributed to another band at appr. 1500 cm^{-1} , which has been designated D_3 band in several earlier studies (Table 6.2). It was suggested that the D_3 band is due to a statistical distribution of amorphous carbon on interstitial places in the disturbed graphitic lattice, or in other words, that it originates from the amorphous carbon fraction of carbon blacks or activated carbons (organic molecules, fragments or functional groups). [Cuesta94, Jawhari95, Sadezky05] That means whenever activated carbons have more functionalities or organic impurities, the D_3 band should be enhanced. Therefore, this observation suggests that the fraction of amorphous carbon in aged anodes is higher than that in aged cathodes and new electrodes, which can be attributed to more complex functional groups formed during the ageing on

anodes. Details will be discussed in the chemical composition characterization part of this work (Chapter 6.2).

A peak at 1200 cm^{-1} can be found in the Raman spectra as a shoulder on the D_1 peak at about 1350 cm^{-1} , which is designated as D_4 in Table 6.2. Dippel et al. observe this band at around 1190 cm^{-1} in Raman spectra of flame carbon black and tentatively attribute it to sp^2 - sp^3 bonds or C–C and C=C stretching vibrations, as found in surface enhanced Raman (SERS) experiments of polyene-like structures. [Dippel99, Ishida86] Sadezky et al. [Sadezky05] support the inclusion of a D_4 band with Lorentzian line shape at about 1180 cm^{-1} in their work, and find that the intensity of this peak increases with the increase of excitation laser wavelength, which explains why this peak was never reported in earlier Raman research performed with $\lambda_0 = 514\text{ nm}$. Raman spectra of the polycyclic aromatic hydrocarbon (PAH) hexabenzocoronene (HBC) are collected with $\lambda_0 = 632\text{ nm}$ in their work and show a clear peak at 1250 cm^{-1} , but no significant D_3 band, which is in good agreement with theoretical calculations for the vibration modes of HBC and other PAHs [Mapelli99] The results from the present study show that the shoulder peak at 1180 cm^{-1} is obviously observable on new electrodes. After ageing, this peak becomes much weaker on anodes while doesn't show significant changes on cathodes. To attribute this peak to a PAH-like structure in disordered graphitic structures of our samples appears more reasonable. Such a structure would be more reactive than other structures in the carbon. But since no further evidence can be found to support this, the assignment has to be preliminary. Two weak peaks above 2000 cm^{-1} can be observed. One is at around 2630 cm^{-1} , which can be assigned to the $2*D_1$ overtone. The other is at around 2922 cm^{-1} and can be assigned to the (D_1+G) combination. No visible change of these two peaks is observed after ageing.

6.1.2.2 Curve fitting and quantitative analysis

The five peaks G, D_1 , D_2 , D_3 and D_4 discussed earlier are all included for the curve fitting. Lorentzian shape is applied for each peak, as shown in Fig. 6.8. Fitting results are summarized in Table 6.3. The intensity of the defect-induced D band (corresponds to the D_1 band in above discussion) can be quantitatively compared to the intensity of the E_{2g} mode G band to yield the in-plane crystallite size (L_a) of graphite. L_a can be taken as a typical length scale for the ordered areas in graphite crystallites but should not be misinterpreted as the size of the graphene “flakes”. Tuinstra and Koenig

[Tuinstra70] note that the ratio of the intensity of the D band to that of the G band varies inversely with L_a (nm):

$$\frac{I(D)}{I(G)} = \frac{C(\lambda_0)}{L_a}$$

where, $I(D)$ = intensity of the D band (D_1 band in the above discussion)

$I(G)$ = intensity of the G band

$C(\lambda_0)$ = constant (e.g. 0.44 nm when $\lambda_0 = 488$ to 514 nm)

λ_0 = incitation laser wavelength

L_a = in-plane grain size of graphite crystallite (nm)

Later studies indicate that the value of $I(D)/I(G)$ is very sensitive to the excitation laser energy [Sinha90, Kastner94, Nikiel93]. For some graphite materials, when the excitation energy varies from 1.67 eV (742 nm) to 2.54 eV (488 nm), $I(D)/I(G)$ can vary from 0.95 to 0.23. So $C(\lambda_0)$ should be related to the excitation laser energy. Based on experimental data from earlier work, Matthews et al. give an empirical formula, whereas, for $400 \text{ nm} < \lambda_0 < 700 \text{ nm}$, C has a linear relationship with the excitation laser wavelength λ_0 : [Matthews99]

$$C(\lambda_0) = C_0 + \lambda_0 C_1$$

where, $C_0 = -12.6 \text{ nm}$, $C_1 = 0.33$.

From this, $C(\lambda_0 = 632.8 \text{ nm}) = 8.3 \text{ nm}$ can be reached.

We estimate the ratio between disordered carbon and crystalline carbon from $I(D_1)/I(G)$ as an evidence for the degree of disorder for the materials, as shown in Table 6.3. Values of $I(D_3)/I(G)$ are also given here.

In general, Raman spectra of new and aged electrodes show no significant differences in the in-plane crystalline size. After ageing, the $I(D_1)/I(G)$ ratio increases, and the in-plane crystalline size decreases a little on both anodes and cathodes, which means the disorder degree increases.

Moreover, the value of $I(D_3)/I(G)$ of anodes is much higher than that of new electrodes and aged cathodes. As discussed before, this result confirms that more functional groups form on aged anodes, which is consistent with the results from the chemical characterization of the present work and will be discussed later. It also suggests that functional groups can distort the graphitic lattice locally.

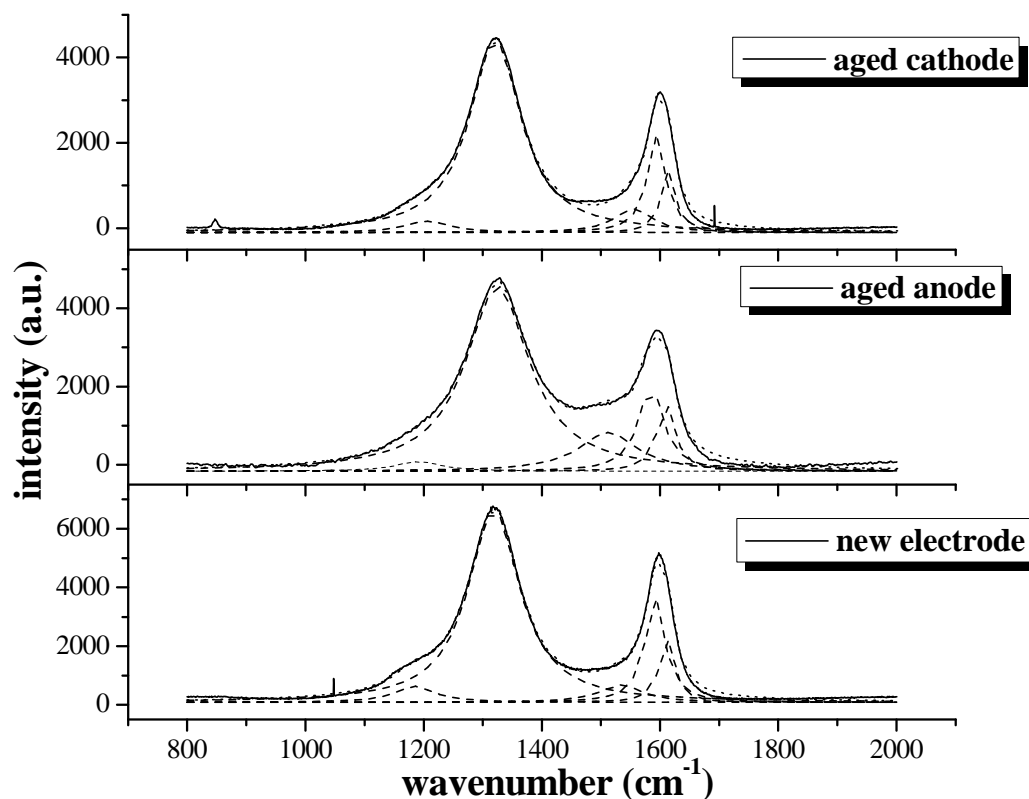


Figure 6.8 Curve fitting for Raman spectra from new and aged-electrodes

Table 6.3 Curve fitting results from new electrode and aged anode and cathode

Sample	Peak position (cm ⁻¹)					I(D ₁)/I(G)	I(D ₃)/I(G)	I(D ₄)/I(G)	La(nm)
	D ₁	D ₂	D ₃	D ₄	G				
New	1318	1611	1534	1185	1591	4.8	0.37	0.32	1.7
Anode	1324	1610	1511	1190	1584	5.5	1.06	0.21	1.5
Cathode	1321	1613	1555	1206	1594	5.6	0.5	0.28	1.5

Curve fitting also shows that the shoulder peak D₄ at about 1200 cm⁻¹ becomes much weaker on aged anodes compared to new electrodes and aged cathodes. As discussed before, this peak can be attributed to structures similar to PAHs, which might be very small flakes in activated carbons. The disappearance of this shoulder peak on aged anodes means this structure changes with ageing.

It might be too simple to estimate La from only one Raman spectrum: Raman spectra refer to the collective information of a rather small area at around several square micrometers in the laser beam, hence inhomogeneity of the material can cause the deviation of the data, and one has to be very cautious to take this as the basis for drawing conclusions. Beyssac et al. [Beyssac03] reported that the structural heterogeneity of carbonaceous materials like natural coal, cokes and anthracite limit the applicability of Raman microspectroscopy for characterization. However, they also found that this shortcoming can be compensated by adopting large probing laser spots of about 40 μm diameter. With the Raman microscope and operating conditions applied in the present study, the diameter of the laser spot ranges from 15 to 40 μm . From the information collected by scanning electron microscopy (SEM), the largest particle size of activated carbons is less than 5 μm , so the laser beam probes several primary particles. Therefore the recorded spectra should be to some degree representative for the investigated samples. Indeed, the spectra recorded at different positions on the surface of our samples mostly look very similar and can hardly be distinguished; all peak positions overlap very well. As already mentioned, we try to eliminate the deviation by taking the average of three spectra from each sample for above comparison and curve fittings.

(*The error is defined as the deviation found from the relative peak intensity of the spectra collected from the same sample. In the present work it is less than 10%. To eliminate this deviation, the average of three spectra collected from each sample is applied for analysis.)

6.1.3 Summary

From the results of the porosimetry and Raman spectroscopy, following conclusions can be drawn:

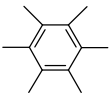
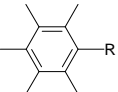
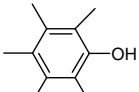
- Aged anodes suffer more from ageing than aged cathodes on both porous structure and microcrystallinity structure.
- Compared to new electrode, the specific area and pore volume of aged anode, decrease much more than aged cathode.
- For anodes, pores in the size range from 1.26 to 3.2 nm are more important than the pores in other size ranges for the capacity of ultracapacitors. The loss of these pores causes the capacity loss.

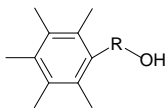
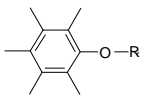
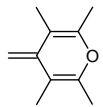
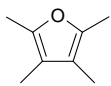
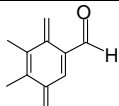
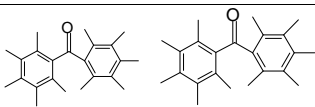
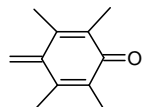
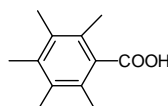
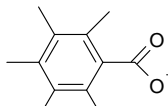
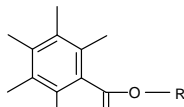
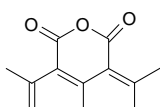
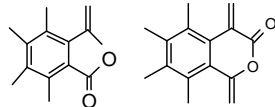
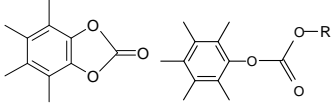
- For cathodes, the pores in the size range from 0.79 to 1.26 nm are blocked by the ageing products, however this is less significant for the capacity loss, compared to the observations from anodes.
- From the Raman spectra, the D₃ band, corresponding to functionalities or organic impurities in carbon on aged anode, is observed to enhance. This means aged anodes have a more disordered structure and probably an amorphous part, compared to new electrodes and aged cathodes.
- The in-plane grain size of aged electrodes is slightly smaller than that of new electrodes, which might result from the breaking of graphene sheets due to some ageing reactions.

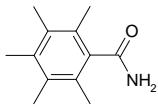
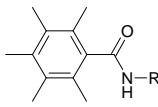
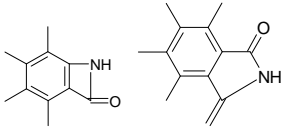
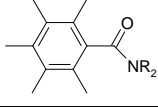
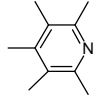
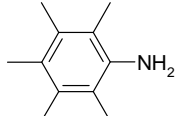
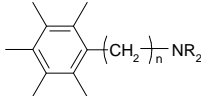
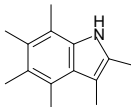
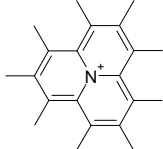
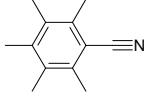
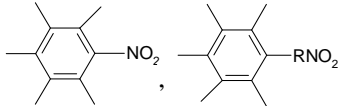
6.2 Chemical composition changes of electrodes

Before we enter into this part, a list of the functional groups involved in the present work are given in the Table 6.4 together with their XPS and IR assignments, which refer to those from organic molecules and polymers [Lin-Vien91, Socrates00, NIST03]. We intend to include all the possible functional groups that may exist in the system, which means not only the functional groups in activated carbons, electrolyte and other raw materials, but theoretically possible ageing reactions products. The assignments listed may not be straightforwardly applied for our results because, when the functional groups are connected to the graphene sheets, the binding energy and IR frequencies might deviate from those observed in the simple systems, which will be discussed later.

Table 6.4 List of functionalities and their assignments in XPS and IR

Groups	Name	XPS BE (eV)		IR bands (cm ⁻¹)
		C 1s	others	
	Graphitic carbon	Ring 284.6		Ring vib. 1620-1400(v)
	Alkyl	C-C, C-H 285.5 ± 0.5		CH str. 3100-2800(m); Ring vib. 1620-1400(v); CH in-plane def. 1480-1410(s)
	Phenol	C-OH 286.3 ± 0.3	532.3-533.6	OH str. Free 3620-3590(m), ass. 3250-3000(m); COH bending 1410-1300(m); CO str. 1260-1150(s);

	Alcohol	C-C, C-H 285 ± 0.5 C-OH 286.3 ± 0.3	532.3-533.6	OH str. free 3670-3580(v), ass. 3590-3230(v); OH def. (in-plane)1440-1260(m);CH str. 3000-2800(wm); CHdef.1480-1410(m); CCO str. 1090-1000(s)
	Ether	CH 285 ± 0.5 C-O-C 286.3 ± 0.3	532.3-533.6	CH str. 3000-2800; =C-O-C asym. 1310- 1210(vs), sym.1120-1020(s)
	Cyclic ether (six- membered)	C-O-C 286.3 ± 0.3	532.3-533.6	Ring =C-O-C= str. 1200- 1120(s), 1100-1050(s); C-O-C str. asym.1100- 1090(s), sym 820-805(m)
	Cyclic ether (five- membered)	C-O-C 286.3 ± 0.3	532.3-533.6	Ring =C-O-C= str. 1200- 1120(s)1100-1050(s); C-O-C str. asym 1080- 1060(s), sym 920-905(m)
	Aldehyde	C=O 287.5 ± 0.3	532.2 ± 0.3	CH str. 2820-2650 (w-m); CH bend ca. 1390 (w); C=O str. 1710-1685 (s)
	Ketone	C=O 287.5 ± 0.3	532.2 ± 0.3	C=O str. 1700-1670(vs.) singly conjugated, 1680-1640 (vs.) doubly conjugated
	quinoid	C=O 287.2 ± 0.3	C=O* 532.2 ± 0.3	C=O str. 1690-1550(vs.)
	Carboxylic acid	C=O 289.1 ± 0.3	C=O 532 ± 0.3 C-OH 533.5 ± 0.3	OH str. free 3580-3500(m), assoc. 3300-2500(m); C=O str. 1710-1660(vs.); C-O str. 1380- 1210 (ms); O-H bending 970-870(m);
	Carboxylate	C-O 289.1 ± 0.3	C=O 532 ± 0.3 C-OH 533.5 ± 0.3	CO ₂ ⁻ str. asym. 1650-1540(s) sym. 1450-1360(ms, br.)
	Ester	C*-O-C=O 286.6 ± 0.3 O=C*-O-C- 288.8 ± 0.3	C=O 532 ± 0.3 C-O-C 533.5 ± 0.3	CH str. 3000-2800(wm), def.1480-1350(wm); C=O str. 1735-1715(vs); C-O-C+C-C-O str. 1300- 1100 (s)
	Anhydride	O=C-O 289.4 ± 0.3	C=O 532.6 ± 0.3 C-O-C 533.7 ± 0.3	C=O str. sym.1860-1850(ms), asym. 1780-1760 (s); C-O-C+C-C-O str. 1150- 980 (s)
	Lactone	C*-O-C=O 286.6 ± 0.3 O=C*-O-C- 288.8 ± 0.3	C=O 532.2 ± 0.2 C-O-C 533.4 ± 0.2	C=O str. 1750-1715(six- membered ring)(s), 1795- 1740 (five-membered ring)(s)
	Carbonate	OCOO 290.7 ± 0.3	C=O 533.5 ± 0.5 O-C-O 535.5 ± 0.3	C=O str. 1780-1740 1850-1790 (five-membered ring)(s)

	Primary amide	C-N 286.6 ± 0.3 C=O 288.8 ± 0.3	N1s 399.8 ± 0.2 O1s 531.8 ± 0.2	C=O str. 1680-1640(amideI); NH ₂ str. asym. 3520-3350(ms), sym. 3400-3160(ms); NH ₂ def. 1640-1620(s); C-N str.1430-1390(wm); NH ₂ rock 1150-1100
	Secondary amide	C*NHC=O 286.6 ± 0.3 C=O 288.8 ± 0.3	N1s 399.8 ± 0.2 O1s 531.6 ± 0.2	C=O str. 1680-1630(amideI); NH str. 3490-3300(m); CNH str.-bend (amideII) trans 1570-1510(s), cis 1490-1400(s); CNH str.-open (Amide III), trans. 1310-1250(m), cis. 1350-1310(m)
	Lactam	C*NHC=O 286.6 ± 0.3 C=O 288.8 ± 0.3	N1s 399.8 ± 0.2 O1s 531.6 ± 0.2	NH str. 3200-3100(m); C=O str. 1750-1700(5-membered ring)(s),1780-1730(4-membered ring)(s); CNH str.-bend, cis. 1490-1440(w)
	Tertiary amide	C*N(CO)C* 286.6 ± 0.3 C=O 288.8 ± 0.3	N1s 399.8 ± 0.2 O1s 531.6 ± 0.2	C=O str. 1680- 1630(s); C-N str. 870-820(wm)
	Pyridine	C-N 286.3 ± 0.3	N1s 398.6 ± 0.4	C=C, C=N ring str. 1615-1570, 1520-1465, 1450-1410 (ms)
	Aromatic amines (anilines)	C-N 286.3 ± 0.3	C-NH ₂ 399.3 ± 0.3 C-N-R 399.8 ± 0.3	NH str. asym. 3500-3420(wm), sym. 3420-3340(wm); NH ₂ scissor. 1638-1602(s); C-N str. 1330-1260(wm)
	Amine	C-N 286.3 ± 0.3	399.2 ± 0.3	NH ₂ str. asym. 3380-3361(wm), sym. 3310-3289(wm); NH ₂ scissor. 1627-1590(s) C-N str. 1250-1000(m)
	Pyrrole derivative	C-N 286.3 ± 0.3	398-399	NH str. 3500-3000(s, br); C=C, C=N ring vib. 1580-1540(m),1510-1460(m), 1430-1380(m)
	Quaternary N	C-N 285.8 ± 0.3	401-402	C=C, C=N ring vib. 1580-1540(m),1510-1460(m), 1430-1380(m)
	Cyano	-CN 287 ± 0.3	400 ± 0.3	N≡C str. 2242-2230(s)
	Nitro	C-NO ₂ 286.3 ± 0.3	405.5 ± 0.3	NO ₂ str. asym. 1555-1487(vs.), sym. 1357-1318(vs)

CH_3CN	Acetonitrile	CH 285 ± 0.3 CN 287 ± 0.3	400 ± 0.3	CHstr. 3000-2800; Nitrile CNstr. 2270,2210(s); CH def. 1450-1405(mw); CHwag 1365-1230(mw); C- C str. 1100-885(m)
Et_4NBF_4	TEATFB	CH 285 ± 0.3 CN 286 ± 0.2	N1s 401.5 ± 0.3 B1s 194.3 ± 0.3 F1s 686.6 ± 0.3	CH str. 3000-2800; B-F str. asym. ca. 1160(vs.); C-H def. ca. 1485, 1410, 850; C4N ⁺ str. asym. 1060-1030
	Poly-acetonitrile	CH 285 N-C*≡N 286.3 ± 0.3	N 1s 398-399	CH str. 2990; C=N str. 1690-1630(w); CH def. 1450-1405(mw); C-H wagging 1365-1230(mw); C-C str. 1100-885(m)
$\text{CH}_3\text{CN}\cdot\text{BF}_3$	Adduct of acetonitrile and BF_3	CH 285 ± 0.2 CN 287.3 ± 0.3	N1s 401.6 ± 0.3 B1s 194.3 ± 0.3 F1s 687 ± 0.3	Nitrile CN str. 2254, 2200; B-F str. asym.1260-1125(s), sym. 1030-800(s); B-N str. 1550-1330(s)
$-(\text{CF}_2)_n-$	PTFE	292 ± 0.3	F1s 689 ± 0.3	C-F str. Asym. 1300-1100(s), sym. 1200-1060(s),
	Carboxylic acid fluoride	No data available	No data available	C=O str. 1900-1790 (vvs); C-F str. 1290-1010(s)
		ring 287.8 CF ₃ 293.6 ± 0.3	F1s 691 ± 0.3	C-F str. 1340-1290(m), sym. 1190-1150(m), 1155-1115(m)
		ring 287 ± 0.3 C-F 292 ± 0.3 CH _n F _(3-n) 286-288	F-C 689.8 ± 0.3 CH _n F _(3-n) 686-688	Ring and C-F str. 1270-1100(v); -CHF ₂ , C-F str. asym. 1205-1105, sym. 1125-1055 -CH ₂ F, C-F str. 1100-900
$\text{R}_3\text{N}\cdots\text{BF}_3$	BF_3 adducts	C-N 286 ± 0.3	N1s 401.4 ± 0.3 F1s 685.8 ± 0.3 B 1s 194.3 ± 0.3	C-N str.1250-1000(wm) B-F str. asym.1260-1125(s), sym. 1030-800(s)
		No data available	No data available	B-C str. 1280-1250 B-F str. asym.1500-1410(s), sym. 1300-1200(s)
		No data available	No data available	C-O-C str. 1300-1000 B-F str. asym.1260-1125(s), sym. 1030-800(s)
		No data available	No data available	B-F str. asym.1260-1125(s), sym. 1030-800(s)

Symbols used

R	alkyl	v	variable
w	weak	m	medium
s	strong	wm	weak to medium
vw	very weak	br.	broad
ms	medium to strong	str.	stretching
def.	deformation	vs	very strong
asym.	asymmetric	sym.	symmetric
ass.	Associated		

Notes: Contrary to common notation in organic chemistry, a line connected to a benzene ring, does not stand for a methyl group, but for a C-C bond in an extended graphene sheet.

6.2.1 Elemental analysis

Elemental analysis is widely applied as a routine characterization method for carbonaceous materials research. It is fast and easy to achieve fairly precise results for the C, H and N content in the studied materials. Table 6.5 gives the CHN elemental analysis results from new and aged electrodes. As already discussed in Chapter 3, the absolute error of this method is 0.3% by weight. Detection limits are generally 0.01 to 0.1%. The samples are washed and dried carefully before sending to the measurement (as introduced in Chapter 4) to prevent the interference from water. All results are the average from three measurements.

As introduced in Chapter 2, the electrodes are composed of several ingredients, but not only the activated carbon, so the carbon content from the electrodes is low compared to pure activated carbon (normally contains more than 90% C as shown in Chapter 8 of the present work). The percentage not associated with C, H or N is often considered to be oxygen in carbonaceous materials, whereas this is not applicable for the present study, because the electrodes contain F from the binder. So “others” in the table corresponds to the content of both F and O.

Table 6.5 Elemental analysis result from new and aged electrodes (%)

Sample	C	H	N	Others
New electrode	88.7	0.4	--	10.9
Aged anode	86.4	0.8	1.5	11.3
Aged cathode	89.5	0.8	0.3	9.4

From the data, it is apparent that there is a significant increase of the N content on aged anodes compared to new electrodes and aged cathodes. Since the samples are washed carefully before being measured, N is not from adsorbed electrolyte (Et_4N^+ or

acetonitrile). The results from not rinsed samples also prove that without rinsing the N content on two aged electrodes does not significantly differ. This is expected because during the polarization Et_4N^+ should not accumulate much at the anode. So the influence from the electrolyte can be excluded, and a preliminary conclusion can be drawn: New species with high N content are formed on anodes during ageing. The content of N on new sample is not detectable by this method, which is probably because the content is lower than the detection limit (around 0.1%). The N content on the cathodes is low, but not zero, which is comparable with the results from the activated carbons that will be described in Chapter 8. We intend to consider this as the contamination. At the same time, the amount of “others” (F and O) increases on anodes while it decreases on cathodes. This could mean that ageing also influences the oxygen functional groups in activated carbon and the fluorine in the binder. To figure out the details of these changes, we correlate data from other methods, which will be discussed later in this chapter.

Normally elemental analysis requires powder samples to avoid errors from incomplete combustion and inhomogeneity. In the present work, the electrodes are foils and cannot be broken up into small particles because of the cohesive agent inside. This might bring about some error to the results. It also limits the feasibility of the experiment so only several samples were measured for obtaining an overview and no systematic data were collected. Still, the data presented above can be taken as an important indication of the elemental composition changes before and after ageing, when they are confirmed by independent data, as will be shown next.

6.2.2 X-ray photoelectron spectroscopy (XPS)

XPS is an important method widely applied for the characterization of the surface of carbonaceous materials. Since the 1970's, it has been used to characterize various carbonaceous materials such as activated carbon fibres, [Proctor82, Kozlowski84, Kozlowski85, Takahagi84, Desimoni90, Mahy94, Gardner95, Zielke96, Alexander94, Alexander95, Alexander96, Pamula03, Moyer89, Pittman99] graphite, [Hammer80, Menachem97] coals, [Cheung82] carbon black, [Papirer94] and activated carbons [Jansen95, Stańczyk95, Polovia97, Nakajima97, Hontoria95].

The complexity of the chemical characteristics of carbonaceous materials makes the interpretation of XPS data not straightforward. Ideally, carbon/oxygen chemical shift data should be obtained from standard surface functional groups for suitably prepared

samples, as the examples shown in Fig. 6.9. But unfortunately such standard model groups cannot easily be prepared because of their complicated synthesis, and often several unwanted groups are found additionally. Therefore the chemical shifts associated with these surface groups have to be obtained from chemical shift measurements for rather different simple carbon compounds, and from theoretical calculations.

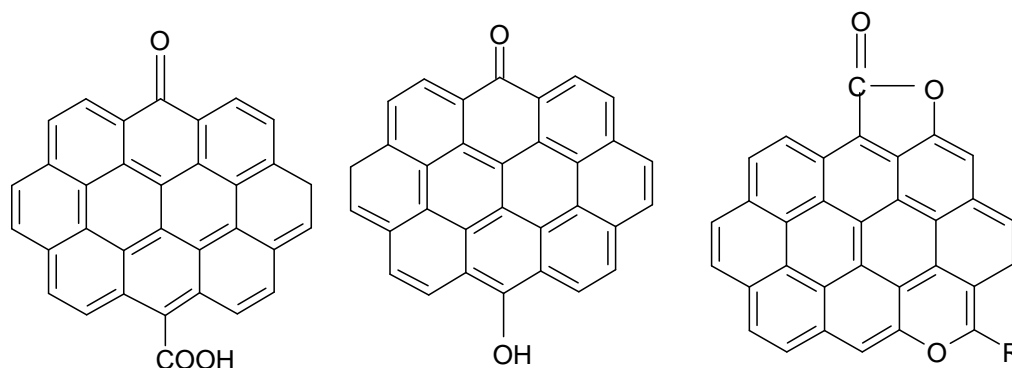


Figure 6.9 Possible model compounds for XPS research

A comprehensive study of carbon/oxygen shifts mainly in polymer systems was carried out by Clark and co-workers. [Clark75, Clark77, Clark78, Clark76, Clark79] An additive C 1s shift toward higher binding energy, of approximate 1.5 eV per single C-O bond, is suggested for a whole range of compounds. The corresponding O 1s shifts are not as easily understood as the C 1s shifts, mainly because the width of the O 1s signal is generally greater than that of the corresponding C 1s signal, leading to less well resolved O 1s peak envelopes.

Proctor and Sherwood [Proctor82] tried to calculate the chemical shifts in carbon fibre spectra and found that the shifts are much more complex than those found in polymers, because the chemical environment is much less predictable. Sherwood and co-workers [Proctor82, Kozlowski84, Kozlowski85, Kozlowski87] investigated carbon fibres in depth and proposed that the chemical shift of 1.6 ± 0.1 eV from the “graphitic peak” at 284.6 eV can be assigned to C-O in alcohol, that $2.1 \text{ eV} \pm 0.1 \text{ eV}$ can be assigned to C=O in ketone and quinoid groups, and that $4 \text{ eV} \pm 0.1 \text{ eV}$ correspond to C=O in carboxylic acid/ester (-COOR) groups. Carbonate groups normally have higher chemical shifts around $6.0 \text{ eV} \pm 0.1 \text{ eV}$, but the peak at this position might also carry contributions from a $\pi\text{-}\pi^*$ shakeup satellite. In addition, a high shift observed at 6.9 eV was found to disappear when there was any significant amount of surface functionality. This can be explained as a plasmon satellite, which

may appear when the photoelectrons escape from the surface and are subject to plasmon excitation (5 ~ 20 eV) (originating from the periodic oscillations of charge density in conductive media) . [Kozlowski84] This effect is intrinsic to the photoemission process and commonly observed in the XPS of simple metals. Correspondingly, the O1s peak at around 531.1 – 531.8 eV is assigned to C=O groups and 532.3 – 533.6 eV to C-O-C and/or C-OH groups. Later on, XPS studies of other carbonaceous materials gave comparable results, and more data were collected, e.g., that adsorbed water has an O1s peak at 535.5 – 536.1 eV.

When nitrogen is imported into the system, the assignment of C 1s becomes more complicated because the binding energy of C bound to N almost overlaps with that of C bound to C. Most of the chemical shifts of C 1s discussed above might have contributions from C-N species and cannot be easily distinguished. In this case, the analysis of N1s spectra is more meaningful for the assignment. From previous research, the following assignments are available: 398.4 eV \pm 0.2 eV is assigned to pyridine moieties; 399 – 400 eV can be assigned to primary amides (-CONH₂) and/or nitrile (-CN), 400.5 eV \pm 0.2 eV can be assigned to aromatic amines (aniline) and secondary amides; quaternary nitrogen can be found at 401 – 402 eV, and nitro groups have much higher shifts above 405 eV. [Kapteijn99, Marletta88, Lahaye99]

XPS spectra of new and aged electrodes

New and aged electrodes from capacitors aged under various conditions were dried and measured with XPS. From the survey scans, F, O and C are found on new electrodes and aged cathodes, while F, O, N and C are found on aged anodes. This result is consistent with the results from the elemental analysis, hence limiting the possibility of considerable errors as discussed in Chapter 6.2.1.

Narrow scans of the F 1s, O 1s, N 1s and C 1s regions were collected, too. The peak positions were calibrated with graphitic carbon at 284.6 eV. Deconvolution of the peaks was carried out with a lineshape of 30% Gaussian and 70% Lorentzian, which is considered to be closest to the XPS natural lineshape. The deconvoluted results show that the binding energy of each component of the C 1s peak varies slightly (\pm 0.3eV) from sample to sample, which is expected because of the large variation of local environment as the surface functionality changes. This phenomenon was also observed by several other researchers [Proctor82, Azais03]. But the results are still well comparable and reproducible for the samples from various ageing degrees. The content of each elements changes with ageing, as the intensity of each deconvoluted

peak, but these cannot be quantitatively compared to the ageing degree. This observation is similar to that from former methods (Chapter 6.1.1 and 6.1.2) applied in the present work. We here focus on the spectra from a single sample (as shown in Fig. 6.10) for an in-depth discussion of the binding energy changes.

On the new electrode, the C 1s signal can be deconvoluted into peaks at 284.6 eV, 285.8 eV, 287.3 eV, 288.2 eV, 290 eV, 292.1 eV, 294.2 eV and 296.2 eV.

284.6 eV is assigned to graphitic carbon in the structure; 285.8 eV can be assigned to C-H or C-C groups at the edge of graphene sheets. 287.3 eV can be assigned to -C=O in ketone and quinoid groups, while 288.2 eV correspond to C=O in carboxylic acid and ester functionalities. The higher chemical shifts at 290 eV might stem from the overlap of the chemical shift from -C=O in lactones, carboxylic acids and esters with $\pi\text{-}\pi^*$ shakeup satellites. Since a fluoropolymer is applied as binder in the electrode, the peak at 292.1 eV should be due to $\text{-CF}_2\text{-CF}_2\text{-}$. A strong tail at higher binding energy contains two peaks at 294.2 eV and 296.2 eV, and is not easy to interpret. Some researchers assigned the peak at 293.5 - 294.2 eV to -CF_3 groups [Beamson00, Koenig02, Wilson01, Yoshihara02, Wu01], but few data for the peak at even higher chemical shift is available. The peak at 296.7 eV was only once reported for the gas tetrafluoromethane [Gelius70], which cannot exist in the present work.

The O 1s peak of the new electrode can be deconvoluted into two peaks at 533.3 eV and 531.5 eV. The peak at 533.3 eV can be assigned to oxygen singly bound to sp^2 carbon (phenol, cyclic ether, lactone) and/or sp^3 carbon (ether, alcohol), and 531.5 eV can be assigned to oxygen doubly bound to carbon, which is linked to aromatic rings (quinoid, ketone, lactone, aldehyde).

In the F 1s spectrum of the new electrode, apart from the strong peak at 689 eV corresponding to $\text{-CF}_2\text{-CF}_2\text{-}$, three peaks at higher binding energy are also observed and difficult to assign. Since only peaks with binding energy higher than 689 eV are observed, fluorine species from other fluoropolymers like $(\text{CH}_n\text{F}_{2-n})_n$ can be excluded here. One presumption is that the fluoropolymer binder suffers changes of its chemical characteristics or imports some contaminants during the electrode processing (such as slurry stirring up, blending and extruding). [Mushiake00] This might be true because both C1s and F1s peaks at high chemical shifts disappear with ageing, as shown later.

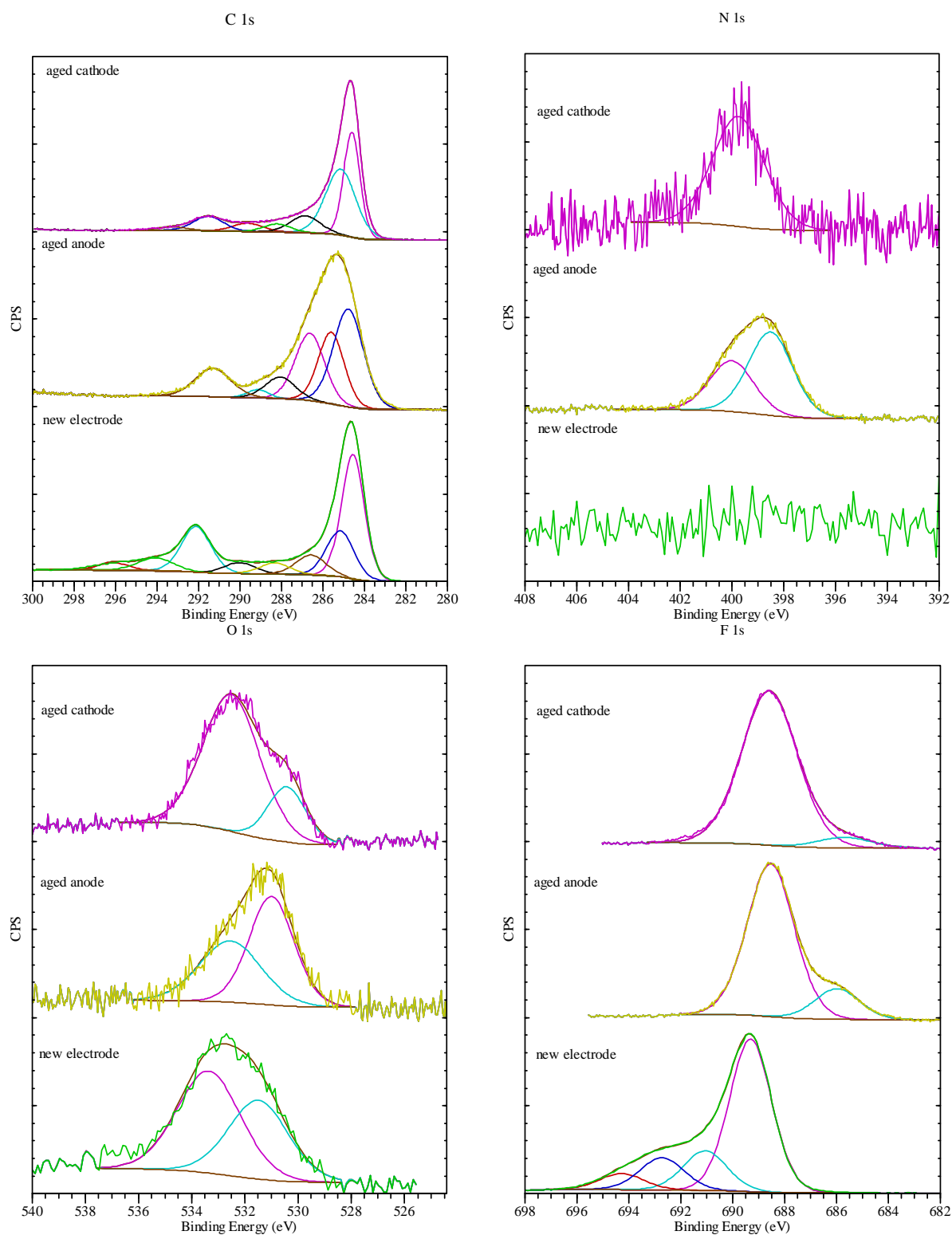


Figure 6.10 XPS spectra from new electrode and aged anode and cathode

At the aged anode, the C 1s signal can be differentiated into 284.6 eV, 285.5 eV, 286.6 eV, 288.2 eV, 289.2 eV and 291.3 eV. Since nitrogen species are present, the interpretation of the C1s peak becomes more complicated as discussed before. It can be seen that the intensities of peaks at around 285.5 eV, 286.6 eV, 288.2 eV increase compared to new samples, while the graphitic carbon signal at 284.6 eV decreases a lot. The peak at 285.5 eV can be assigned to C-H and C-C at the edge of graphene sheets, as well to C-N bonds (in amines); the peak at 286.6 eV can be an overlap of –C=O in quinoid and keton groups, C-O-C, C-N (in amides), nitrile groups and -C=N in polyacetonitrile; the peak at 288.2 eV can be correlated to -C=O bond in aldehyde, carboxylic acid, ester and amide functionalities; the peak at 289.3 eV can be assigned to C=O in carboxylic acid, ester and lactone functionalities. The peak at 291.3 eV belongs to the fluoropolymer binder. The intensity of this peak decreases compared to the new electrode. This phenomenon has been observed in the modification of fluoropolymer surfaces with physical or chemical methods. After plasma treatment [Fu04, Koenig02, Wilson01], radiation grafting [Adem05] or degradation [Hoflund04, Everett05, Everett05, Li05], the single peak of the fluoropolymer broadens and weakens, and other peaks at lower binding energies (289 eV, 288 eV) corresponding to -CH₂CF₂-, -CHFCH₂- and -CHFCHF- are found. So the peaks at lower binding energies should count in the contribution from these species.

The N1s peak of the aged anode is differentiated into two peaks at 398.8 ± 0.2 eV and 400.2 ± 0.2 eV. The peak at 398.8 ± 0.2 eV can be assigned to pyridine moieties (-C=N-C-), amines(C-NH₂), and C=N in polyacetonitrile (-CN), the peak at 400.2 ± 0.2 eV to amides. The peak at 401 – 402 eV, which correlates with quaternary nitrogen, is not observed thereby the influence from the electrolyte salt (Et₄N⁺) can be excluded.

The O1s peak at the aged anode has two peaks at around 533.0 eV and 531.2 eV. Although these are close to those on the new electrode, the assignment should be different because of the findings from C 1s peak and IR results discussed later. We intend to assign the peak at around 533.0 eV to C-O-C (ether), C-OH groups (phenol) and C-O single bond in carboxylic acid, ester and lactone functionalities. The peak at 531.2 eV is assigned to C=O in carboxylic acid, ester and lactone.

The F1s peak at the aged anode is narrower than that of a new electrode and contains two chemical shifts: 688.8 ± 0.2 eV which can be assigned to CF₂-CF₂ in fluoropolymer (this is consistent with the C 1s signal at around 291.3 eV); 685.8 ± 0.2

eV which might come from the degradation like $\text{CF}_2\text{-CHF-}$ and/or $\text{-CH}_2\text{-CHF}$ from the contaminants in binder as mentioned above.

On the aged cathode, the deconvoluted C1s peaks are at about 284.6 eV, 285.5 eV, 286.8 eV, 288.2 eV, 289.6 eV, 291.5 eV and 293.2 eV. Since there is little nitrogen, these peaks are assigned exclusively to C-C or C-O species. The peak at about 285.2 eV can be assigned to C-H and C-C bonds at the edge of graphene sheets; the peak at about 286.8 eV to -C=O in ketone and quinoid groups, as well as C-O-C in ether, C-OH in phenol and alcohol groups; the peak at around 288.2 eV correlates to -C=O bond in aldehyde, carboxylic acid and ester functionalities; the peak at 289.6 eV, other than the -C=O in carboxylic acid, ester and lactone functionalities, can also be assigned to CH_2CHF , etc. The peak at 291.5 eV belongs to the fluoropolymer binder, and the intensity of this peak becomes much weaker, which suggests severe degradation of fluoropolymer binder compared to that on the aged anode. A weak peak at 293.2 eV can be observed, which might result from the contaminants as discussed for the new electrode.

The components of the O 1s peak at the aged cathode are at around 533 eV and 531.8 eV and can be assigned similar to those at the aged anode.

Although there is an N 1s signal found on aged cathode, the signal to noise ratio indicates that the content is very low. In some of other samples this peak disappears totally so it can be ignored to be discussed in detail here.

The components of the O 1s peak at around 533 eV and 531.8 eV can be assigned similar to those for the aged anodes.

F 1s signal at the aged cathode is “pure”, i.e. it contains one clearcut main peak, compared to the new electrode and aged anode. The peak with binding energy at about 688.8 eV corresponds to fluoropolymer. A small tail is found at lower binding energy around 686 eV, which can be assigned to the degrading product as described before.

XPS is only a semi-quantitative method and the deconvolution can import some artificial effects, so the quantitative analysis cannot be taken for precise comparison. But for a primary analysis of the relative concentration, the data show good consistency and can be considered as convincing.

As shown in the spectra, the relative amount of elements changes after ageing. Elemental atomic concentration is calculated from the spectra and listed in Table 6.6.

The oxygen content on both aged anode and cathode increased while the fluorine content on both ends decrease.

Table 6.6 Atomic concentration (%) of elements in electrodes

	New electrode	Aged anode	Aged cathode
F	35	20.7	17.7
O	1.4	2.3	2.5
N	0	12.5	--
C	63.6	64.5	79.8

Furthermore, the atomic concentration calculated from deconvoluted peaks in the C 1s envelop is listed in table 6.7. From the data in the table, the ratio of graphitic carbon decreases after ageing both on both anodes and cathodes. This indicates that the graphitic structure is partially broken during ageing and transformed to another state.

The peak at 285.5 ± 0.3 eV increases both on aged anodes (9.9%) and aged cathodes (26.2%), and becomes especially large on cathodes. From the assignment of this peak, the increase on aged anodes might be partly from C-C bonds at the edge of graphene sheets and/or from C-H species, and partly from C-N species. On cathodes, this peak refers to C-C bonds at the edge of graphene sheets and/or C-H bonds.

The peak at 287 ± 0.3 eV increases on both ends, but much more on anodes (17.6%) than that on cathodes (4.4%). This peak combines several possibilities of C-N species. The increase of this peak on anodes can be explained by the enrichment of nitrogen. On cathodes, only very limited amounts of oxygen species form, so the increase is not as significant.

The absence of the peak at 289.3 ± 0.3 eV and the rather small peak at 288 ± 0.3 eV might prove that in new electrodes, the carbonyl group in carboxylic acids, anhydrides or esters are rare, and that oxygen functionalities exist mainly as quinones or ketones. After ageing, the contents of these two peaks increases on both anodes and cathodes: the anodic contribution is likely due to carbonyl groups in amides, carboxylic acids and esters or C=N bond, while the cathode features contributions from carbonyl groups in carboxylic acids or esters.

Since the atomic concentration of oxygen on anodes and cathodes is very similar, the higher contribution of the peaks at 287 ± 0.3 , 288 ± 0.3 and 289.3 ± 0.3 eV on aged anodes should mainly result from C-N moieties in amides and from -C=N moieties.

Table 6.7 Atomic ratio (%) of different components of peak C 1s in electrodes

Binding energy	Assignment	New electrode	Aged anode	Aged cathode
284.6	Graphitic carbon	48.7	34.3	33
285.5 ± 0.3	C-H, C-C at the edge of graphene sheets and C-N	11.8	21.7	38
286.8 ± 0.3	-C=O quinoid, ketone, C-OH, C-O-C, C=N-C	5.2	22.8	9.6
288.2 ± 0.3	-C=O in ketone, carboxylic acid and ester, amide; C=N-C bond, CHFCH ₂	2.5	7.5	4.2
289.3 ± 0.3	-C=O in carboxylic acid and ester, amide; CHFCH ₂ , CF ₂ CH ₂		2.0	4.8
290.2 ± 0.3	-C=O in carboxylic acid and ester, amide; and π-π* transition	4.4		
291.7 ± 0.3	-CF ₂ - in fluoropolymer	18.6	11.7	8.4
294.2 ± 0.3	CF ₃	6		2
296.2 ± 0.3	No available interpretation	2.8		

The decrease of the peak at 291.7 ± 0.3 eV, corresponding to fluoropolymers, can be explained as the degradation of binder. The peaks at even higher binding energy disappear after ageing, which might mean these species are the active species taking part in the ageing reactions.

6.2.3 Attenuated total reflection Fourier transform infrared (ATR-FTIR)

Numerous IR spectroscopic studies have been conducted on various forms of carbon, including coals [Puente98, Iglesias98], carbon blacks [Rositani87], chars [Starsinic83, Zhuang94] carbon films [Zawadzki89, Zawadzki78, Zawadzki81] and activated carbons. [Ishizaki81, Danderkar98, Valente04] However, IR spectra of carbon materials are difficult to obtain because of the problems in sample preparation, poor transmission, uneven light scattering related to large particle size, and so forth. [Socrates00] Moreover, the electronic structure of carbon materials results in a very broad absorption band extending from the visible region to the infrared. Fortunately, some of these problems can be overcome by improving sample preparation (e.g., carbon films) as well as by using relatively new IR techniques such as attenuated total reflection Fourier transform IR spectroscopy (ATR-FTIR) [Ohwaki95, Ohwaki95, Sellitti90, Shin97, Nakahara95] and diffuse reflectance Fourier transform IR spectroscopy (DRIFT). [Yang95, Mul98, Fabián04, Figueiredo99, Fanning93]

Besides the technical difficulties in obtaining IR spectra of carbon materials, their interpretation is often an additional problem because not all of the observed absorption bands may be assigned unequivocally to specific molecular motions of functional groups. Band assignments have been made based on model compounds and on expectations of the types of functional groups present. Over the years, there have frequently been disagreements regarding band assignments, and the fact that these bands can be quite broad makes the situation more complicated. Therefore, it is not uncommon that some band assignments differ substantially among the published IR studies on carbon materials.

Fanning and Vannice [Fanning93] analyzed data from earlier results and found that a consensus could be reached regarding the assignment of band frequencies to different functional groups. Their summary of the principal groups along with the range of frequencies associated with them are listed in Table 6.8.

Table 6.8 Principal functional groups on carbon surfaces and their corresponding infrared assignments [Fanning93]

Groups	Assignment regions (cm ⁻¹)		
	1000-1500	1500-2050	2050-3700
C-O stretching of ethers	1000-1300		
Ether bridge between rings	1230-1250		
Cyclic ethers containing COCOC	1025-1141		
Alcohols:			
C-OH stretch	1049-1276		
O-H bend/stretch			3200-3640
Phenolic groups:			
C-OH stretch	1000-1220		
O-H bend/stretch	1160-1200		2500-3620
Carbonates: carboxyl-carbonates	1100-1500	1590-1600	
Aromatic C=C stretching		1585-1600	
Quinones		1550-1680	
Carboxylic acids (COOH)	1120-1200	1665-1760	2500-3300
Lactones	1160-1370	1675-1790	
Anhydrides	980-1300	1740-1880	
Ketenes (C=C=O)			2080-2200
C-H stretch			2600-3000

Most of the data from later work are consistent with Fanning's summary. Fuente et al. [Fuente03] employed quantum chemical methods to calculate vibrational frequencies of a large set of polyaromatic model compounds to assign the vibrational motions in the 1400-1900 cm⁻¹ range and proposed that the relative order of the vibrational C=O frequencies in wavenumbers (cm⁻¹) is: five-membered ring lactone (>1830) >

anhydride (1810-1740) \approx six-membered ring lactone (1790) $>$ lactol (O=C-O-C-OH connected to aromatic ring) (>1780) $>$ carboxylic acid (>1750). They also found that the C=O stretching vibrations of the carboxylic acid and lactone models are not influenced by the size of the graphene platelet, while the corresponding wavenumbers of the lactol and anhydride models are clearly lowered (20-30 cm^{-1}) by increasing the number of carbon rings. These observations suggest that C=O vibrations of anhydride groups on carbon materials could result in a broad IR band (1740-1810 cm^{-1}), whereas the bands due to “isolated” carboxylic acid and lactone groups should be sharper, more intense, and less sensitive to conjugation. This is helpful for the assignment of various functional groups.

Apart from hydrogen and oxygen, nitrogen can often be found in carbon materials. As the oxygen functional groups like carboxylic acid, hydroxyl, etc., can influence the acidity and wettability of carbon significantly, the presence of nitrogen-containing surface groups may also considerably influence the surface acidity and affinity towards ions. For example, amine groups may decrease the acidity. [Jankowska91, Abotsi90, Jankowska85, Jankowska83] Much effort has been spent on applying IR to characterize the nitrogen species on activated carbon surface. [Biniak97, Valente04, Fabián04, Mangun01, Zawadzki03] However, vibration frequencies from N-containing surface groups often overlap with those from O functional groups or graphene sheets. For example, C=C, C=O and C=N in plane vibrations are found in the same range between 1615 and 1570 cm^{-1} [Socrates00], and the C-N stretching mode is in the range of 1300 to 1000 cm^{-1} which is similar to the range for the C-O stretching mode. Hence, the assignment of IR bands needs extra caution and sometimes the cooperation with the results from other methods such as XPS applied in the present work. [Ohwaki95, Mangun01, Sullivan00, Hontoria-Lucas95, Pamula03]

Infrared Spectra of new and aged electrodes

In the present work, attenuated total reflection infrared (ATR-IR) has been applied for the characterization of surface of new and aged electrodes. IR spectra from aged anodes and cathodes show characteristic differences from new electrodes, and anodes show more and larger differences than cathodes. The wavenumbers of the IR bands are well reproducible for most of the samples from various ageing conditions. However, similar to the observations in XPS, the relative intensity of these bands varies with the samples and cannot be directly connected to the ageing degree. As for

XPS, hereinafter the spectra from a single sample are focused on to make an in-depth discussion.

The relative intensity variation can also be found when measuring different positions of the same sample, which might be due to spatial inhomogeneity of ageing. Generally, the signal from the “outer surface” of electrodes is stronger than that from “inside” (after stripping off with adhesive tape, see Fig. 6.11) which means the chemical or electrochemical changes mainly happen close to the interface of the electrodes and separator.

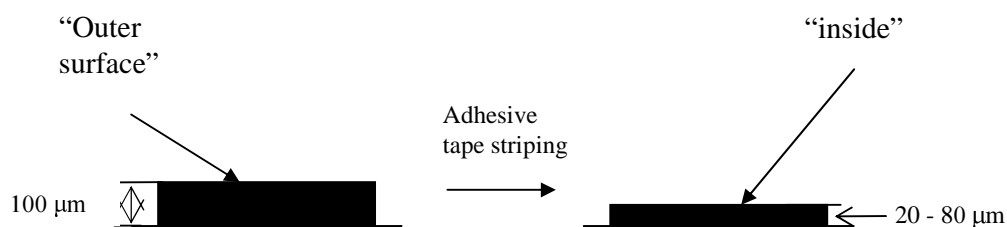


Fig 6.11 The “outer surface” and “inside” for measurement

Overview spectra in the range from 4000 to 700 cm^{-1} are shown in Fig. 6.12. As already discussed in the Chapter 3 for this method, the effective penetration depth is usually a fraction of a wavelength and in a conductive solid it is inversely proportional to the wavenumber, so the absorbance is higher at low wavenumbers. Hence the overall shape is based on a sloping baseline. [Ohwaki95, Foster68, Borghesi90, Sellitti90] All spectra shown here are the “original” results of the division of the single beam spectrum from each sample to that from the background (air), see Chapter 3. To avoid artifacts, no mathematical treatment such as baseline correction has been done. For this reason, these spectra offer the chance to do semi-quantitative comparisons based on the relative intensity of each characteristic band. For example, from the spectra it can be seen that the double bands at 1220 cm^{-1} and 1154 cm^{-1} which stem from fluoropolymer binder decrease on both anode and cathode after ageing, but to different extent.

The spectrum from the new electrode shows only three bands, 1580 cm^{-1} , 1220 cm^{-1} and 1154 cm^{-1} . Bands at 1220 cm^{-1} and 1154 cm^{-1} are sharp and can be clearly assigned to the fluoropolymer binder in the electrode. These two bands can also be found on the aged anode and cathode, while as mentioned above, the relative intensity becomes lower.

The band at 1580 cm^{-1} is broad and strong. This peak is a prominent feature in the IR spectra of active carbons, chars, coals, and so forth. [Puente98, Iglesias98, Rositani87,

Zawadzki89, Ishizaki81] The assignment of this peak is full of controversy, it can be attributed to either oxygen functional groups or ring vibrations of the basal plane of graphitic carbon (as shown in Fig. 6.7). Intriguingly, presence and intensity of this band are strictly related to the concentration of surface oxides, but an IR calculation [Frisch98] using carbon with attached oxygen groups does not support an assignment to carbonyl-type species. A widely accepted hypothesis assigns the 1580 cm^{-1} band to C=C stretching modes of polyaromatic systems [Socrates00, Fanning93, Georgakopoulos03] whose IR intensity would be reinforced by oxygen functional groups, most likely because of an increase in the dipole moment associated with these ring vibrations [Fuente03]. Sometimes this band is assigned to C=C stretching modes of polyaromatic systems combined with C=O stretching mode from quinoid functional groups [Biniak97, Figueiredo99]. Till today, the relationship between the nature of oxygen functional groups and the intensity of this band is largely unknown. In the present work we intend to apply the latter assignment.

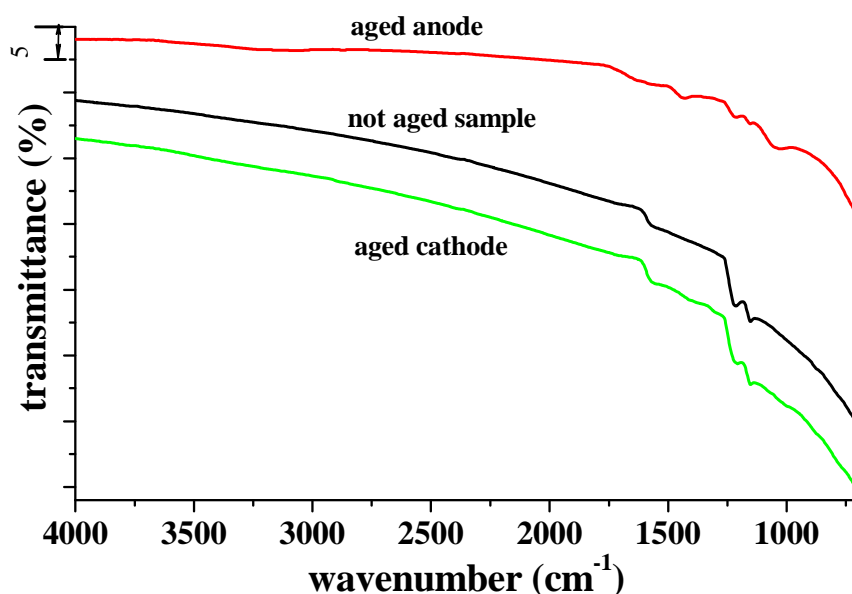


Figure 6.12 IR spectra for the new and aged samples

On the aged anode, other than the bands observed in the new electrode, several other bands can be distinguished, i.e. a broad band between 3600 and 3000 cm^{-1} , a broad band between 1750 and 1600 cm^{-1} of which the maximum is at around 1660 cm^{-1} , a strong band at 1436 cm^{-1} , a weak band at 1350 cm^{-1} and a broad band between 1110

and 1000 cm^{-1} . Fig. 6.13 gives the comparison of new and aged electrodes in the range from 4000 to 2600 cm^{-1} , and from 2000 to 800 cm^{-1} .

In the present work, both elemental analysis and XPS results indicate that N species exist on aged anode. Thus the broad band between 3600 and 3000 cm^{-1} can be assigned to O-H or N-H stretching modes. The bands at around 3600 to 3350 cm^{-1} are normally from free O-H stretching modes in phenolic or carboxylic acid structures; they can also be due to free N-H stretching modes from primary amide or amine groups. Bands in the lower range from 3400 to 3200 cm^{-1} can be assigned to the combination of the stretching vibration from associated O-H groups and the stretching vibration from associated N-H groups. At around 3100 - 3050 cm^{-1} there is a band which can be due to the stretching vibration of aromatic hydrocarbons, or an overtone from C-N-H stretch-bend vibration in secondary amides. C-H stretching mode can also be found in the region from 3100 to 2800 cm^{-1} , and is hard to distinguish from the former two bands. [Socrate00, Lin-Vien91]

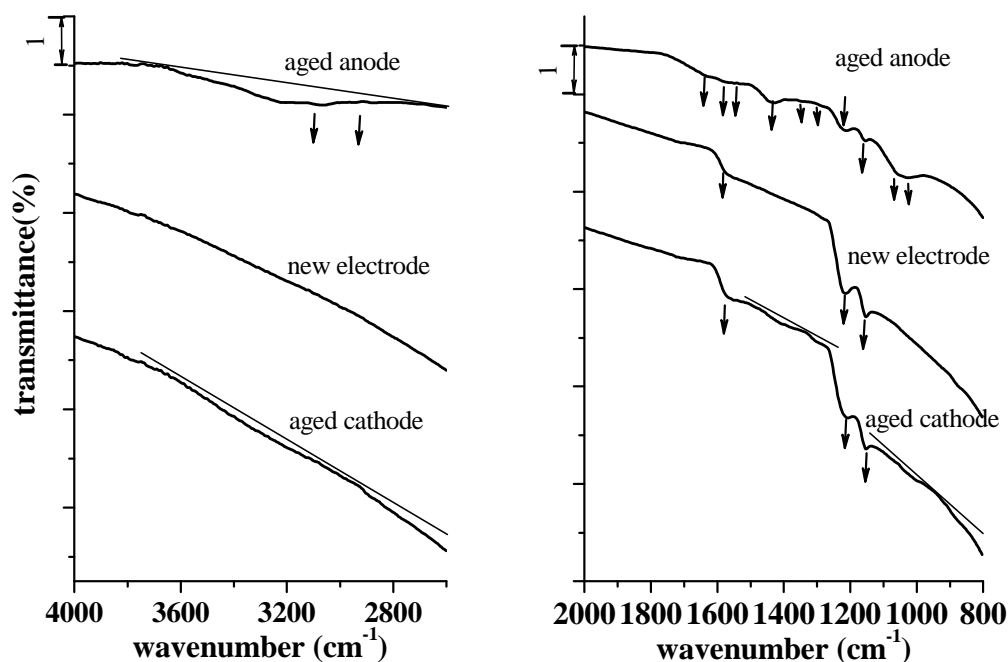


Figure 6.13 IR spectra in the regions 4000 - 2600 cm^{-1} and 2000 - 800 cm^{-1} for the new and aged samples. Between 1800 and 1600 cm^{-1} , the C=O stretching mode of carbonyl groups can normally be found. The C=O stretching mode from anhydrides is usually found at higher wavenumbers from 1740 to 1800 cm^{-1} , which in the present work cannot be observed. Carboxylic acids and lactones show this band from 1660 to 1790 cm^{-1} ,

ketones and quinoids from 1550 to 1700 cm^{-1} . Moreover, amides have a C=O band usually in the region 1630 to 1695 cm^{-1} , which is defined as amide I band. Another possibility is from C=N stretching modes, which show up at slightly lower energy than C=O modes and are hard to distinguish especially for unknown chemical composition. The broadness of the band in this region means an overlap of these vibrations and the co-existence of functionalities like carboxylic acids, lactones, ketones, amides and pyridinic structures. The band at about 1580 cm^{-1} discussed above remains observable.

Another discernable band at 1540 cm^{-1} can be correlated to the C-N-H stretch-bend mode, which is normally called amide II band from (trans-monosubstituted secondary amides).

The band in the region of 1460 to 1400 cm^{-1} can be assigned to a mixing of C-OH in-plane bending vibrations from carboxylic acid and phenol groups, C-N-H bending vibrations in cis-amides, C-H deformations, and possibly from aromatic C-C stretching modes.

The band at lower wavenumbers around 1370 cm^{-1} and 1340 cm^{-1} (weak intensity) are considered to be from O-H deformation vibrations, C-N stretching modes in amides, and C-O stretching modes in lactones might also contribute.

In the range of 1300 to 1000 cm^{-1} , there is also a broad band and two maximum can be found at around 1060 and 1035 cm^{-1} . The band in this region is often explained as C-O stretching mode from ether, ester, or phenol groups. The deformation of N-H can also be seen in this region, and when $-\text{NH}_2$ exists in the structure, there should be a doublet in the range of 1150-950 cm^{-1} . C-H in-plane bending on aromatic rings is also found here. In the present work we intend to assign this band to a mixing of the above-mentioned vibrations because none of them can be absolutely excluded from the results.

The spectrum from the aged cathode shows much less changes compared with that of the aged anode. But in the spectral regions from 3500 to 3000 cm^{-1} and from 1300 to 1000 cm^{-1} , broad and weak bands can be observed. A band at around 1420 cm^{-1} can also be found. Since the results from both elemental analysis and XPS show that there is little N on cathode, these bands mainly result from carbon and oxygen species. The bands between 3600 and 3000 cm^{-1} can be assigned to O-H stretching vibration in phenol and carboxylic acid groups. Since no peak is easily observable in the range from 1800 to 1600 cm^{-1} range which corresponds to the vibration of carbonyl groups,

the content of carboxylic acid should be very low. C-H stretching mode might also be present because a weak peak is discernable in the lower region from 3000 to 2800 cm^{-1} . The band at about 1420 cm^{-1} can be assigned to a mixing of C-OH in-plane bending and/or C-H deformation modes. The band around 1300 to 1000 cm^{-1} is due to C-O stretching mode in phenol groups and/or C-H in-plane bendings on aromatic rings. The spectrum of the aged cathode features a broad and weak band from 1000 to 800 cm^{-1} , which might be due to the C-H out-of-plane bendings.

The observed IR bands from new and aged electrodes are summarized in Table 6.9.

Table 6.9 IR bands (cm^{-1}) obtained and related assignments

New electrode	Aged anodes	Aged cathodes	Assignment
	3600 – 3000 (br.)	3600 – 3000 (br., w)	N-H, O-H str.
	3100 – 2800	3100 – 2800*	C-H str. C-N-H str. o.t., ar. OH
	1750 – 1600 (br.)		C=O str. (ketone, ester, amides), C=N str.
1580	1580	1580	C=C str. conj. C=O str.
	1540		C-N-H str.-bend
	1436 (s)	1420 (w.)*	C-OH in-plane bend, C-N-H bend, C-H def., C=C str.(ar.)
	1350 (w)		O-H def., C-N, C-O str.
1220 (sh., s.)	1220 (sh.)	1220 (sh.)	CF ₂ asym. str.
1154 (sh., s.)	1154 (sh.)	1154 (sh.)	CF ₂ sym. str.
	1110 – 1000 (br.)	1110 – 1000 (br., w)	C-O str.
		1000 – 800 (br., w.)	C-H bend.

Symbols used

w	weak	br.	broad
str.	stretching	def.	deformation
asym.	asymmetric	sym.	symmetric
sh.	Sharp	o.t.	overtone

* only corresponds to functional groups with C, H and O

From the results discussed above, carbonyl groups from quinone-like structures on anodes are transformed into carbonyl groups in carboxylic acids, lactones and phenols. Moreover, N-containing species form, which would possibly have amide like structures.

On cathodes, only new oxygen functional groups like carboxylic acids, phenols and lactones form. However, their amount is much lower than that on anodes according to the intensity of the bands.

6.2.4 Summary

From the results of IR and XPS (refer to Table 6.7 and 6.9), following conclusions can be drawn:

- IR and XPS results prove that not only new elements are present, but indeed covalently linked functional groups are formed. The functionalization of carbon takes place during ageing, instead of simple physisorption processes.
- On new electrodes, only small amounts of oxygen species exist, and are mainly in the form of quinoids, ketones and ethers.
- After ageing, more oxygen moieties are formed, which can be in the form of phenol, carboxylic acids and esters (lactones). These species exist on both aged anode and cathode.
- Nitrogen from pyridine moieties (-C=N-C-), amines(C-NH₂), polyacetonitrile, amides (lactams) form on aged anodes. They should be the ageing products from electrolyte decomposition, which will be discussed in detail in the following chapter for ageing mechanism analysis.
- The increase of the content of oxygen functional groups with ageing might suggest that oxygen groups are not preferable for the stability of the ultracapacitors.

* Even if consider the occurrence of the minima in DFT pore size distribution as an artifact or noise, one can realize that the frequency of this noise is of molecular dimension which is near the resolution limit of any adsorption-based characterization method. Regarding quantitative estimates of pore volumes, it was shown that fluctuations of the differential PSD have a small effect on the shape of the cumulative PSD and thus more stable values of pore volumes are obtained for larger intervals of pore sizes. All these prove the reliability of this method.

Chapter 7

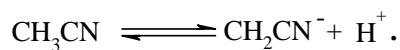
Ageing mechanisms of the ultracapacitors

According to the observations and discussions in Chapter 6, the chemical species in the not aged system and the functional groups produced on aged anodes and cathodes after ageing can be summarized as follows (see Table 7.1).

Table 7.1 Chemical species in not aged system and functional groups on aged anodes and cathodes

Not aged system	Aged anode	Aged cathode
Electrode: C-C at edge of graphene sheets & C-H species, carbonyl groups in ketone and quinoids, ether group C-F species incl. CF ₂ , CF ₃ Electrolyte: (CH ₃ CH ₂) ₄ N ⁺ BF ₄ ⁻ , CH ₃ CN	C-C at the edge of graphene sheets & C-H species Amide (primary and secondary), polyacetonitrile, amines, pyridinic structure carboxylic acid, phenol, ester, C-F species (incl. CH _n F _{2-n})	C-C at the edge of graphene sheets & C-H species, phenol (main), ester and carboxylic acid (minor), C-F species (incl. CH _n F _{2-n})

All the components in the not aged system may contribute to the ageing. The electrolyte salt and acetonitrile should be the two main factors contributing to the electrochemical or chemical processes on electrodes. As introduced in the corresponding section of Chapter 2, the oxidation potentials of BF₄⁻ and PF₆⁻ are higher than that of the solvent. Hence the oxidation potential limit of the present system is due to the solvents rather than the salts. This might be due to the fact that acetonitrile may act as a proton source as follows:



Acetonitrile is a very weak Bronsted acid, the pK_a value of it is 25 [Wade04]. However, the proton is an active moiety that can further excite many electrochemical processes, and thus may promote the deprotonation of acetonitrile. The residual part of acetonitrile can take part in other reactions, contributing to ageing, as discussed later.

On the other hand, ultracapacitors should theoretically be a closed system; water and oxygen intrusion cannot occur. Nevertheless, in reality the system is never completely sealed and there is always the permeation of acetonitrile and gas evolution, as proven by the observation of the weight loss and gas evolution of the ultracapacitors [Hahn04, Hahn05]. In this case, it cannot be excluded that water and oxygen from air can diffuse into the system during the ageing. At the same time, even though the electrolyte is in battery grade solution, (high purity), impurities like HF from the salt and water from the solvent may exist in trace amount. Water might also be trapped in the pores of the activated carbon, in the separator and in the aluminium foil, and be difficult to remove completely during the drying step of the ultracapacitor manufacturing process.

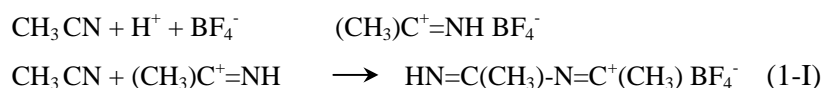
All of these factors have to be taken into consideration for the ageing mechanisms.

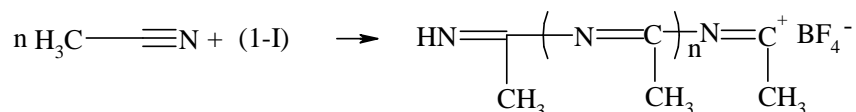
7.1 Anodic reactions

On the aged anode, nitrogen moieties have been found. In the presently studied system, the N sources can be found in electrolyte, both in the solvent (acetonitrile) and in the cation (Et_4N^+) of the salt. However, it is expected that most cations accumulate at the end of cathode in the charging state and will not contribute much to the anodic process. As introduced in Chapter 2, acetonitrile belongs to the most common class of aprotic solvents for electrochemical use, and has been studied in various systems. [Krtil93, Foley88, Portis72, Tourillon79, Billon59/60] BF_4^- or PF_6^- anions can considerably improve the anodic stability of acetonitrile compared to ClO_4^- with Pt as working electrode. [Mann69, Portis72, Fleischmann68] However, similar stability is expected when sufficient conditions are supplied, e.g. being polarized at sufficiently high voltage for a long time. Presumably, the active species of activated carbons can stimulate some of the processes, too.

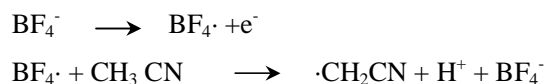
The possible anodic processes in BF_4^-/ACN system are listed below. The effects and possibility of the reactions are discussed separately. Hereinafter “A” is used to stand for the anodic process.

A-1. Polymerization of acetonitrile

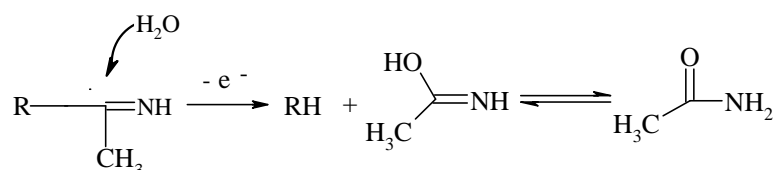




Protons can be produced by the solvent, as shown at the beginning of this chapter. Based on the results from Tourillon [Tourillon79], the deprotonization can also be promoted by the BF_4^- as follows,



The water impurity can result in the consecutive reaction, i.e. end groups can be attacked and lead to various fragments including acetamide. (in which R = polymer chain of polyacetonitrile).

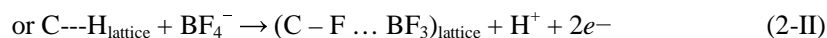
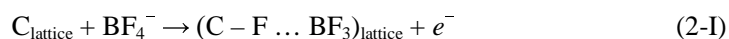


Effects and possibility:

The results from Chapter 6 indicate that the large micropores (1.26 to 2 nm) and small size mesopores (2 to 3.2 nm) are blocked by the polymer, thus resulting in capacity loss.

The porosity loss and the nitrogen enrichment on the anode have been clearly evidenced even in the least aged ultracapacitors. The XPS and IR characteristics of polyacetonitrile correspond well to the observations. This suggests that in the present system this reaction can take place with mild ageing conditions and would be the major contribution for the capacity loss. Presumably, the Lewis acidic functional groups connected to the graphene sheets can attract the lone pair electrons on nitrogen in acetonitrile to shift the electron cloud and promote the deprotonation. The strength of the interaction can be related to the electrophilicity, which is supposed to be COOH (carboxylic acid) > $(\text{C}=\text{O})\text{OR}$ (esters) > $(\text{C}=\text{O})\text{H}$ (aldehydes) > $(\text{C}=\text{O})$ (ketones and quinoids).

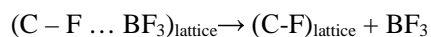
A-2. Tetrafluoroborate anions can react with the activated carbon electrode in the following way, similar to a glassy carbon electrode [Chandrasekaran90]



As discussed in mechanism A-1, BF_4^- can first release a charge to form a BF_4^\bullet radical (which is very reactive). So the fluorination might also be fulfilled by the attack of BF_4^\bullet radical on the carbon lattice, which would be:



However, the boron is not observed on the aged anodes in the present study, we presume that after fluorination, BF_3 may diffuse away but not adhere to the electrodes.



Thus only carbon fluoride is formed on the anode.

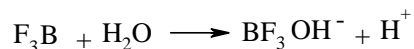
Effects and possibility:

The mechanism proposed by the researcher is analogous to the formation of graphite fluoride compounds prepared by passing fluorine into a graphite matrix. It is, to some degree, similar to the intercalation and might bring about the expansion of the distance between two graphene sheets. When the effects accumulate seriously, the lattice structure will be influenced, thus resulting in the decrease of conductivity and contributing to the increase of the ESR. Furthermore, this reaction produces protons, which is harmful to the whole system.

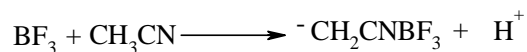
Activated carbons and carbon blacks are rich in active edge sites and there is an abundance of BF_4^- . The factors facilitate the onset of this reaction. The F 1s peak observed in XPS spectra at lower binding energy (around 686 eV) can be correlated to these species.

A-3. Subsequent to the mechanism A-2, BF_3 , as a strong Lewis acid, can interact with many other species due to its unique six-electron shell. One possibility is to form adduct with CH_3CN since nitrogen has a lone pair. $\text{CH}_3\text{CN}\cdot\text{BF}_3$ was observed to emerge at relatively low potential (1.0V vs. Ag/Ag^+) by the in-situ infrared spectra-electrochemical study, and the signal became stronger with the potential increase. [Foley88, Backer05]

Moreover, it can react with trace water to release a proton:



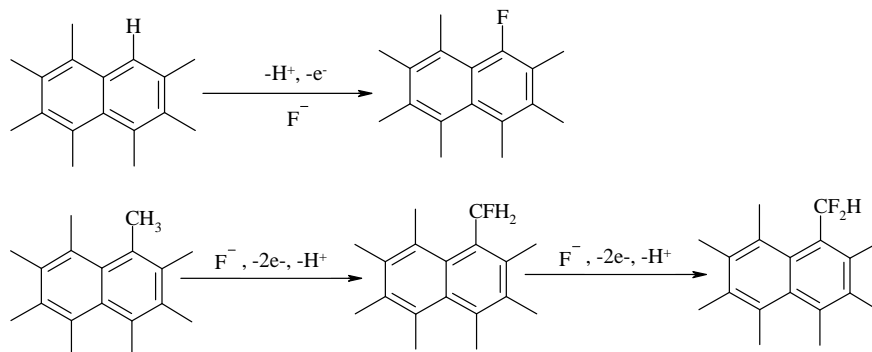
Considering the content of water, this reaction should not be significant. However, a similar reaction might also happen with acetonitrile,



Effects and possibility:

The reaction in which BF_3 further stimulates the deprotonation of acetonitrile is very harmful to the system. This can promote the anodic polymerization of acetonitrile and other side reactions that need protons. According to conditions observed in the prior studies mentioned above, as well as the abundance of the species, this reaction is supposed to be very likely and can happen even without high potential and high temperature.

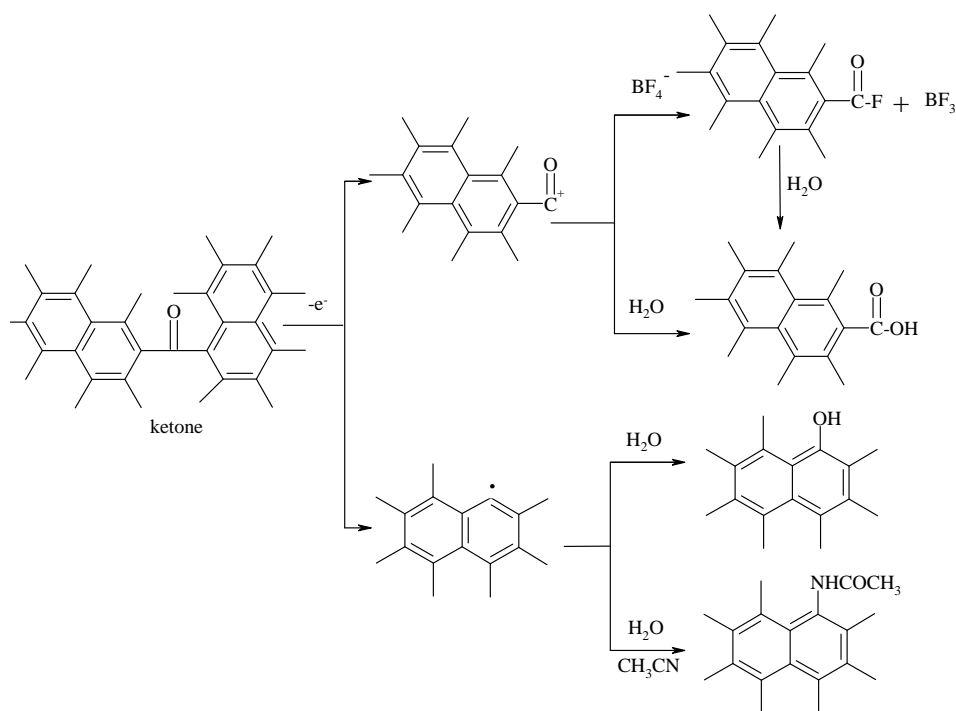
A-4. Anodic partial fluorination of aromatic compounds was first reported in 1970 [Rozhkov70]. In that case, tetraethylammonium fluoride was applied as the electrolyte in acetonitrile. In the present work, similar reactions might also occur but with the hydrogen or alkyl groups at the edge of graphene sheets in activated carbon. The products may contribute to the F 1s peak at around 686 eV, too.



Effects and possibility:

The import of the fluorine species in this way will bring about similar effects and observations as discussed in mechanism A-2. However, the intercalation is not so significant for this reaction. It is hard to avoid when fluorine ions exist in the system, and the amount can be determined by the quantity of fluorine ions.

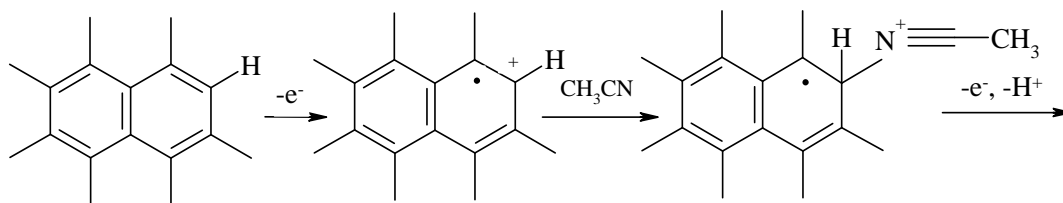
A-5. Koch et al. [Koch73] studied the anodic fluorination of benzyl ketones with tetrafluoroborate salts in acetonitrile at Pt, and found the following reactions at high potential (2.0V vs. Ag/Ag^+). The acid fluoride should be the main products because of the abundance of the functional groups in the activated carbon and the BF_4^- in the electrolyte. However, it is not stable in the presence of trace water and easily forms carboxylic acid.

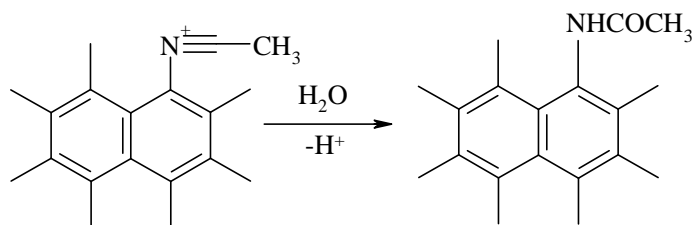


Effects and possibility:

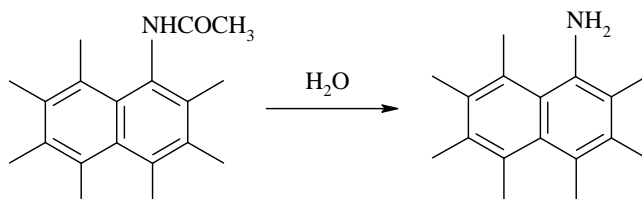
This reaction breaks the connection of two graphene sheets, which should be stressed because it may have some influence on microcrystallinity characteristics, as observed in Raman spectra. Moreover, the continuity of the electron transfer between two graphene sheets is broken. Two edges with active sites are produced to further react with other species as shown above. The products are observed on the anodes in the present study, such as carboxyl acid group, phenol group and secondary amide, even in the weakly aged samples. This indicates they do not need high potential or temperature to be produced. However, the amount should be related to the water content of the system.

A-6. The acetamidation might happen on the carbon surface with hydrogen connected to the edge plane of graphene sheets.





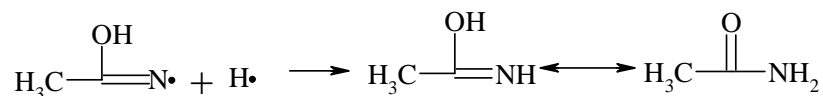
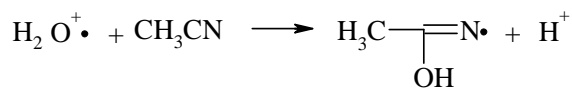
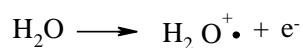
If water exists, the secondary amide might be hydrolyzed to amine structure, but this process needs relatively extreme conditions like high acidity.



Effects and possibility:

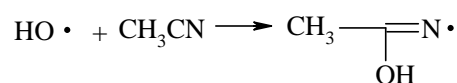
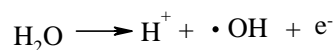
This reaction is to some degree, like the functionalization of the graphene sheets, and it releases protons at the same time. Both are harmful to the system. The surface acidity is changed by the formation of secondary amide and amine groups. The products are observed on the aged anodes from weakly aged ultracapacitors, which suggests that this reaction can happen under mild conditions. The amount of the products can be determined by the water content.

A-7. Although water cannot directly hydrolyze acetonitrile, it can react with acetonitrile as follows:



Here the hydrogen radicals may be taken from the surface of activated carbons.

This reaction can also be excited by the HO \cdot and then the first two reactions proceed in the following way:



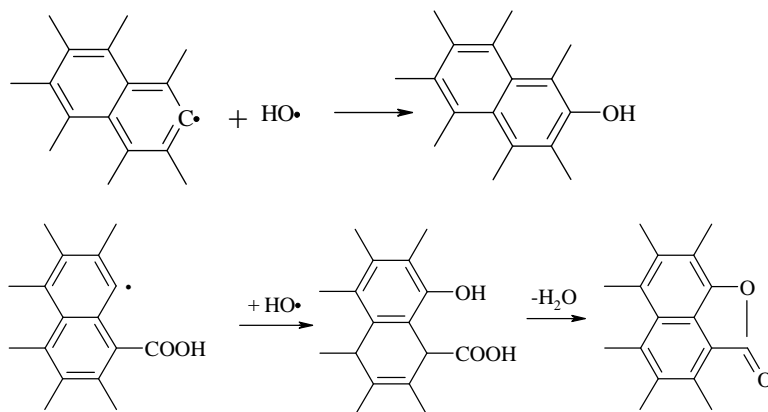
Effects and possibility:

The reactions may stimulate the deprotonation of acetonitrile, which is harmful to the system. Since it is excited by water, it doesn't need demanding conditions like high potential. The content of water in the system will determine the extent of this reaction.

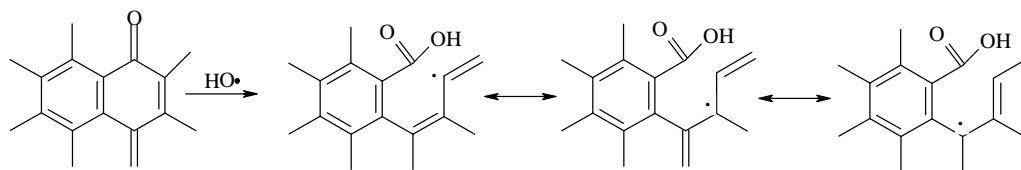
A-8. The intermediates mentioned in mechanism A-7 like H_2O^+ and $\text{OH}\cdot$ are all very reactive radicals. $\cdot\text{OH}$ is well known to be the most reactive oxygen-centered radical and particularly indiscriminate in its choice of reactant.

At the same time, quite a few unpaired electrons, such as delocalized π electrons and localized-unpaired σ exist on the carbon surface (Fig. 2.11). Their amount is normally proportional to the surface area, and can be correlated to the content of oxygen functional groups. Donnet [Donnet68, Donnet73] asserted that these radicals are not so reactive as the typical radicals known in organic chemistry for two reasons: one is that they are not easy to approach in normal conditions, the other is, they cannot migrate since they are attached to the graphene sheets (steric hindrance). However, ageing is a long term process and other active species may have enough time to approach these sites.

The $\cdot\text{OH}$ can bond itself to the radicals in activated carbons to produce phenol groups.



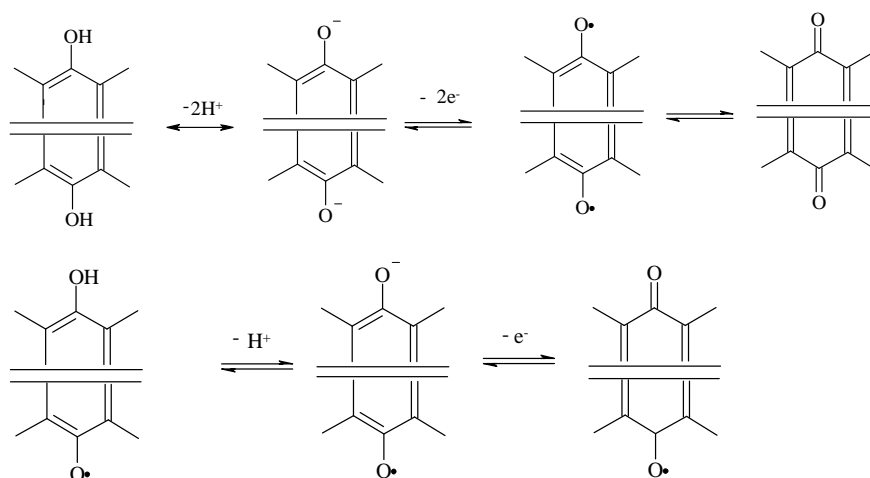
Or, the radical can cleave a C-C bond at the edge of graphene sheet and move on to the graphene sheet and be stabilized. Afterwards, the radical on the graphene sheet may react further, like abstracting H from CH_3CN .



Effects and possibility:

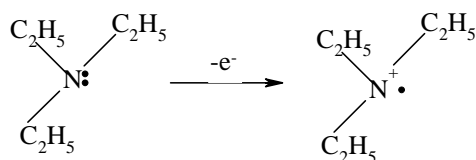
The population of the phenol, carboxylic and ester groups on the edge of graphene sheets may distort the graphene sheets and influence the conductivity. At the same time, the surface properties of activated carbons will be more active with these functional groups (see the discussion in mechanism A-1). The products contribute to the observation of the oxygen functional groups on aged anodes from weakly aged ultracapacitors. The amount of these products is also determined by the water content.

A-9. Phenol groups that exist on activated carbon surfaces can be oxidized to quinoid as follows:

**Effects and possibility:**

This is a counter reaction of the reduction of quinoid groups on the cathode. The main negative effect of this reaction might be the release of protons. On the other hand, it recovers the quinoid groups on the activated carbon surface. This reaction does not need demanding conditions to fulfill.

A-10. Triethylamine (C_2H_5)₃N produced from the cathodic process, discussed in the cathodic section below, can migrate slowly back to anode. (C_2H_5)₃N on anode easily forms its radical cation, which is comparatively stable



The radical can then diffuse to the separator and oxidize other substances (back reaction) without the presence of the electrode.

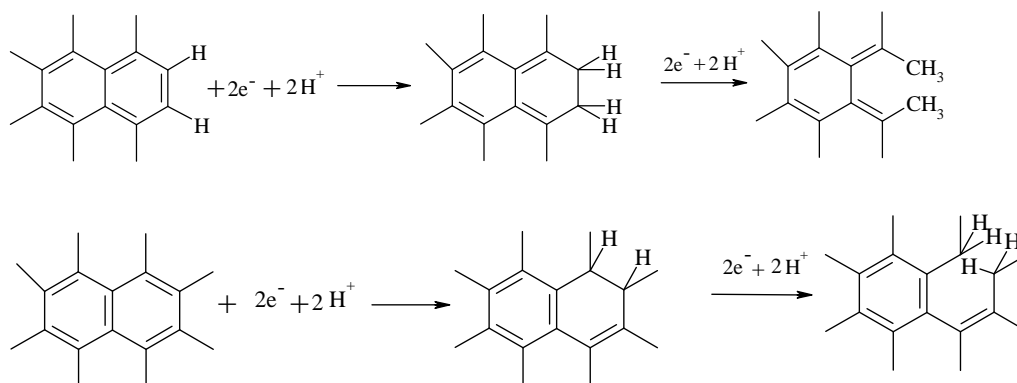
Effects and possibility:

This process is unfavourable since the product can further react with other species even without the existence of the electrode, e.g., to deprotonate the acetonitrile. Since there is abundance of Et_4N^+ cations in the system, the yield of $(\text{C}_2\text{H}_5)_3\text{N}$ can be high and may contribute significantly to the ageing process.

7.2 Cathodic reactions

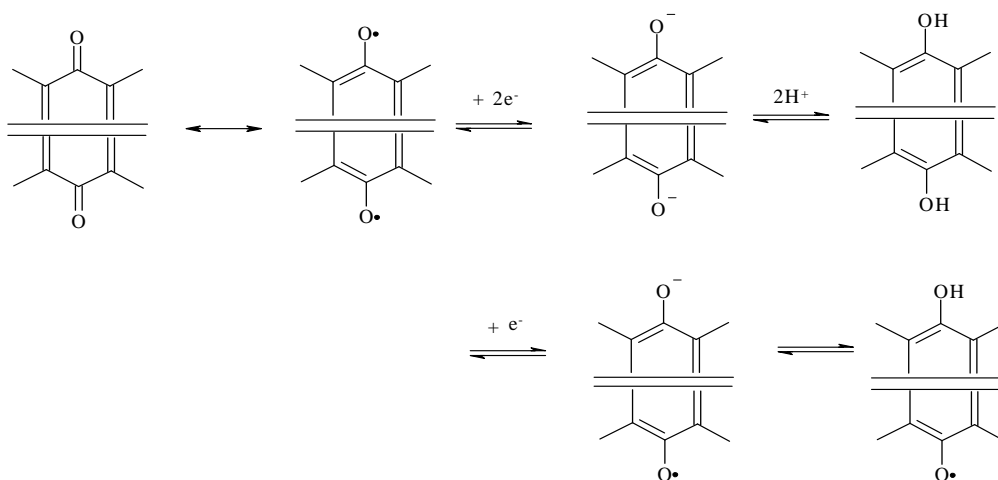
The species involved in cathodic processes should mainly be the cations (Et_4N^+) and solvent. Similar to section 7.1, the possible cathodic processes are discussed hereinafter, and cathodic process is symbolized as “C”.

C-1. The C=C bond on the edge or on the outer surface of graphene sheets is expected to be reduced with the addition of two protons. The C-C bonds formed can be broken to form two methyl groups at the edge of graphene sheets.

**Effects and possibility:**

In both reactions, the first step brings the structure to a state that can react further, because the C-C single bond in the structure is easy to be broken. In this case, the extent of graphene sheets can be broken, thus the ordering of graphene sheets is disturbed and cause the decrease of the conductivity. On the other hand, more active species like hydrogen and methyl groups at the edge of graphene sheets are formed. The XPS results presented in Chapter 6 indicate that the content of C-C bond at the edge of graphene sheets and C-H bond increases significantly on aged cathodes. This strongly suggests that this mechanism gives the main contribution for the chemical composition changes on the cathode.

C-2. Quinoid groups on the surface of activated carbons can be reduced as follows,

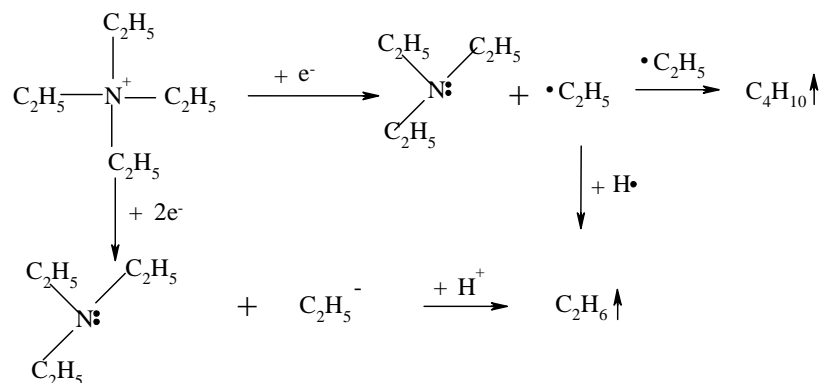


Effects and possibility:

This process may consume the protons in the system and thus be favourable to slow down the ageing process. According prior studies, phenol group is one of the main products on aged cathodes. It is well documented citations and does not need extreme conditions to proceed.

C-3. The cathodic behaviour of quaternary ammonium salts has been widely studied. [Finkelstein59, Finkelstein65, Simonet77, Bernard79, Swenson83, Kariv-Miller84, 85, 86, Svetlicic86, Mayell63, Gedye80] The electrochemical cleavage of quaternary ammonium salts can occur and will generate hydrocarbons and tertiary amines. It was found that a series of quaternary ammonium salts containing the alkyl group could be decomposed electrolytically to yield varying alkanes and alkenes. This mechanism can be applied to explain the observation in the present study as well. The overall change involved in the electrochemical decomposition of the Et_4N^+ can be summarized accordingly as follows:

a. Gas evolution from one alkyl group cleavage – formation of ethylene and butane:

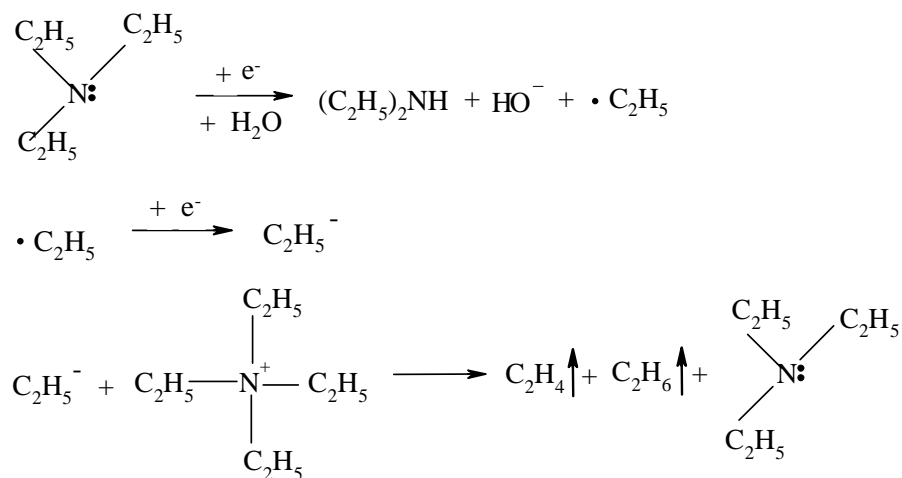


Protons can be taken from the acetonitrile as mentioned before, and hydrogen radicals can be taken from the edge of graphene sheets.

Effects and possibility:

This reaction is highly unfavourable for the ultracapacitor system because the gas evolution will bring about the increase of internal pressure, destroying the sealing of the system and promoting other aging problems like solvent evaporation. Since there is plenty of Et_4N^+ and the cleavage of one of the alkyl groups is observed in the aqueous system, the potential required for this reaction is low, which means it can happen in the weakly aged ultracapacitors. Since all these processes happen in the liquid phase, results from solid electrodes, presented in the present work, cannot give strong evidence for them. However, previous gas evolution studies [Hahn04, Hahn05] may prove that they occur.

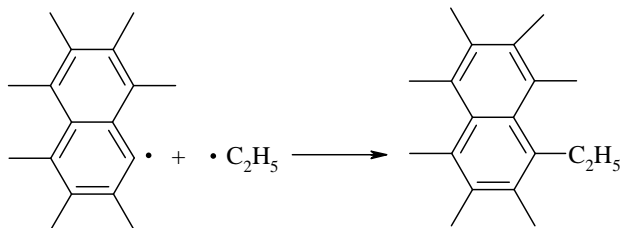
b. The Et_3N : can cathodically react with water to form $\text{C}_2\text{H}_5\cdot$ and OH^- , which attack the Et_4N^+ further to generate ethylene and ethane.



Effects and possibility:

The effect of this reaction is similar to the discussion for above reaction. However, this reaction is excited by water, so the amount should be determined by the content of water impurity.

C-4. The ethyl radical produced near activated carbons can attach to their σ radicals, as discussed in mechanism A-8.



Effects and possibility:

This reaction may consume the ethyl radicals produced in the system, thus reducing the probability of gas evolution. This reaction is positive for the system. The XPS and IR characteristics of this structure are similar to the products from the mechanism C-1. However, this reaction is not easy to realize because the σ radicals on activated carbons are not easy to approach.

C-5. It is already mentioned at the first beginning of this chapter that acetonitrile can release protons.



Consecutively, the protons can accumulate to the cathode and be reduced to hydrogen.



Water can also be reduced to release H_2 , however, the contribution should mainly be from acetonitrile in the present work.

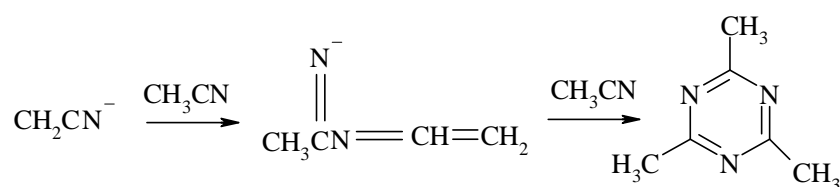
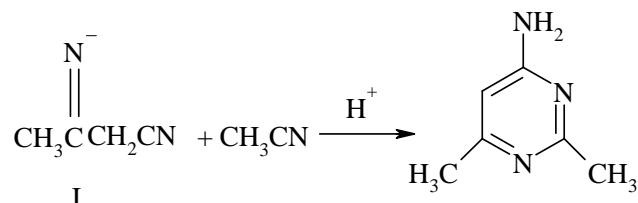
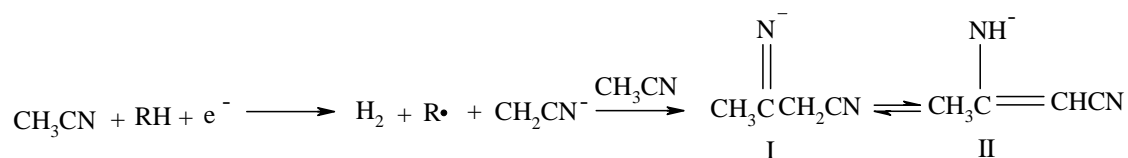
Effects and possibility:

This reaction certainly contributes to the gas evolution and internal pressure accumulation. According to the gas evolution study, hydrogen may be a major product of the cathodic gas evolution in acetonitrile system. [Hahn04, Hahn05] Moreover, it is not observed in propylene carbonate system, which further supports the assertion that the proton source should be acetonitrile and not water. Considering the abundance of acetonitrile, this reaction may be significant for the ageing.

C-6. The reduction behaviour of acetonitrile has been studied with tetraalkylammonium salt as electrolyte [Pons82, Foley87, Fleischmann73]

It was found that acetonitrile can be reduced to a tautomeric mixture of dimers of acetonitrile (I and II shown below) and be observed by in-situ IR measurement. If the

electrolysis is held at high negative potentials for extended period of time, the trimers can be produced.



R = graphene sheets

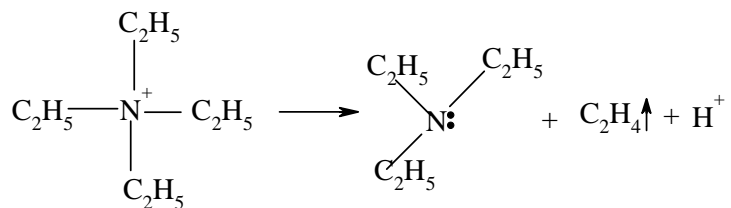
Effects and possibility:

The negative effect of mechanism C-6 is the hydrogen evolution and deprotonation of acetonitrile. The products of this reaction are not observed, which might be due to the fact that these products migrate into the electrolyte but do not deposit on the electrodes, or that they are in small quantities. The consecutive reactions were observed to start at very negative potential (-2.2 V vs. Ag/Ag⁺) with the presence of water, which conditions are not easy to fulfill in the present system.

7.3 Non-electrochemical reactions

Apart from the electrochemical reactions discussed above, some non-electrochemical reactions may come about. Here “NE” is taken as the symbol for non-electrochemical reactions.

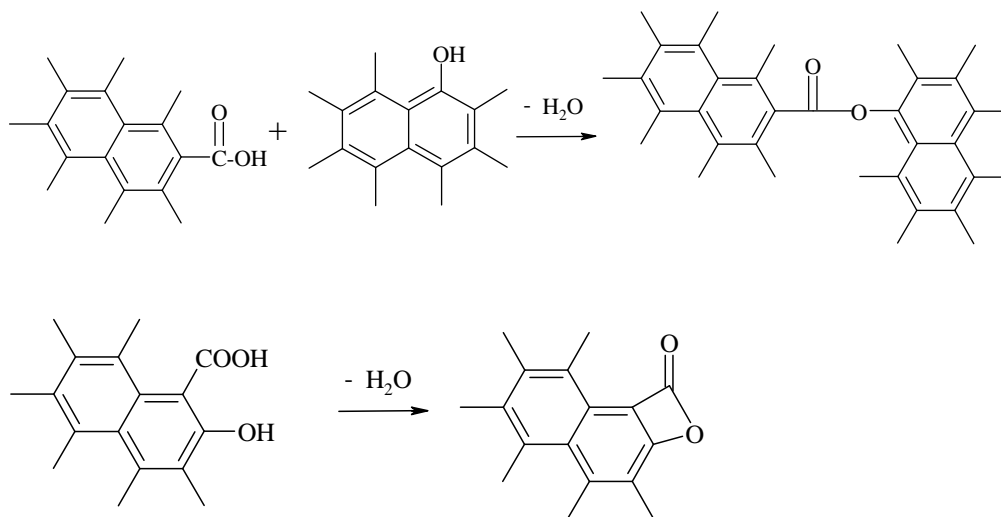
NE1. Hofmann elimination can occur on the Et₄N⁺ to produce ethylene, triethylammonium and proton.



Effects and possibility:

This reaction has very negative effect for the system, because it can bring about gas evolution and release protons at the same time. It can arise in mild conditions, e.g., in Bronsted basic condition and with mild heating (150 °C), and the evolution of ethylene might promote the reaction. So it is supposed to happen when the ultracapacitors are heated.

NE2. Carboxylic acid groups and phenol groups on the activated carbons can condense, which takes place either between the graphene sheets or along the edge of graphene sheets. This process happens during the production of activated carbon when the carbonization is carried out to release water.

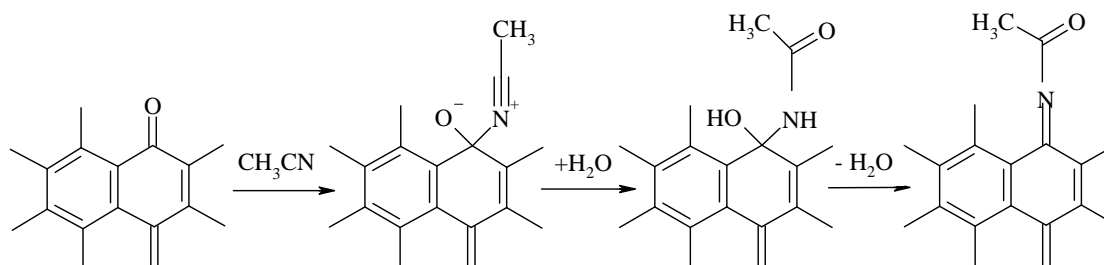


Effects and possibility:

Through this reaction, two graphene sheets can be connected, or COOH and OH can be condensed into a ring. Both effects have some positive influences. However, this reaction has the negative effect to produce water. Since the results in the present work prove that there are not plenty of carboxylic acid and phenol groups in the not aged samples, this reaction should be minor in the first stage of polarization. The carboxylic acid and phenol groups generated through other reactions during ageing,

as discussed before, can take part in this reaction afterward thereby enhancing its likelihood.

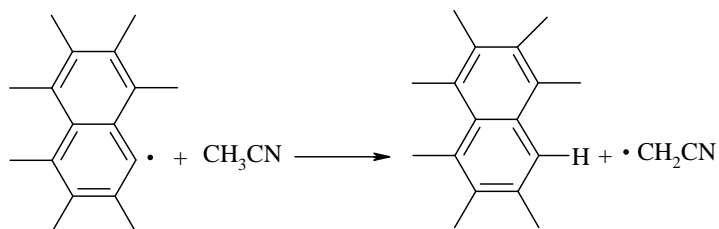
NE3. When carbonyl groups exist, which is the case for the electrode in the present study (carbonyl groups exist in ketone and quinoid groups), the following reaction may occur [Lund01]



Effects and possibility:

Similar to the discussion above, the formation of the amide group may influence the surface acidity of the activated carbons, but it is hard to predict whether it is positive or negative for the performance of the ultracapacitors. Moreover, the N species observed on aged anodes are mainly from polyacetonitrile, primary and secondary amides, but not the third amide, which might suggest that this reaction happens rarely in the ultracapacitor system.

NE4. If the acetonitrile approaches radicals existing on the activated carbon surfaces as introduced above, a hydrogen can be taken from acetonitrile to attach to the graphene sheets and the radical is transformed to acetonitrile.



Effects and possibility:

The generated acetonitrile radicals are active to further react with other species. This is a negative effect. The abundance of the species and the time scale of ageing facilitate the occurrence of this reaction.

7.4 Summary

We have discussed the possible electrochemical and non-electrochemical reactions in the present system to analyze the ageing processes. Although some of the reactions might call for critical conditions, the unique characteristics of activated carbons and time scale of ageing can allow these to occur.

Oxygen-containing functional groups can affect the ageing reactions from two perspectives: On one hand, various oxygen-containing functional groups can promote some reactions. On the other hand, a higher amount of functionalities means that more electroactive sites can be found on the graphene sheets in activated carbons (e.g. the radicals on graphene sheets) to stimulate other reactions.

Impurities like water and F^- are very active and may take part in some of the ageing reactions as discussed above.

According to the observation and mechanism analysis, some reactions can happen under mild conditions and do not need high potential and high temperature at the same time. So it might be worthwhile to carry out research to further figure out the essential conditions for each reaction, for example, to age the ultracapacitors only at various temperature without potential loading or to age them only with potential loading but no heating.

Some phenomena observed in the present work are still not easy to understand such as the influence from fluoropolymer binder. As the binder for the activated carbon layer of electrodes, this material brings about some interesting questions, such as whether the original material may have several kinds of fluorine species which can be active for the ageing reactions and disappear from the electrode after ageing. Based on the data and background of the present work, we cannot give a satisfactory explanation.

Another point that has to be mentioned is that we did not take into account other impurities that might exist in the system, like Fe^{2+} , Cu^{2+} , K^+ and halide ions like Cl^- , that might be contained in activated carbons and electrolytes, or in the separator and the casing materials. These species might also contribute to ageing.

Chapter 8

Ageing effects on individual components of electrodes of ultracapacitors

In the above chapters, we focused on the observations from electrodes and discussed the ageing mechanisms based on them. However, the electrode is a mixing of several components including activated carbon powders, conductive agents, binders, etc., and the complexity makes the analysis of the problems more complicated. The ageing effect on each component of electrodes is still not clear, especially the existence of fluoropolymer binders interferes the observation and analysis seriously. In this chapter, we try to “divide” the electrode and discuss the observation from the ageing experiments on activated carbons and conductive agents independently to identify the individual influence.

Porosimetry and Raman spectroscopy are applied for the structural characterization of the activated carbon samples; CHN elemental analysis, IR and XPS are applied for the chemical composition characterization.

For the conductive agents, Raman spectroscopy is applied for the structural characterization. The information of their chemical composition changes are collected by elemental analysis and IR.

8.1 Ageing effect on the activated carbons

As described in Chapter 4, three activated carbon samples provided by Epcos are chosen for ageing experiments, two (A and B) from natural precursors (coconut shell) and one (C) from synthetic resin precursor. The treatment and washing procedures refer to Chapter 4. Briefly, chemical ageing is to heat the samples in acetonitrile or electrolyte for a certain time period; electrochemical ageing is to polarize the samples at 3 V for a certain time period; afterwards the aged samples are thoroughly rinsed by acetonitrile in order to completely remove the salt adsorbed in the pores; before the measurement, the samples are dried in vacuum oven (80°C, 10^{-3} Torr) overnight to remove residual solvent and water in pores. To simplify the description, samples without ageing treatment are called as-received powders, samples collected from the anodic and cathodic ends of the electrochemical ageing experiments are called aged anode powders and aged cathode powders, respectively.

8.1.1 Microstructural changes

No significant influences were observed from porosimetry and Raman spectra on the activated carbon powders after chemical ageing. However, it was observed that electrochemical ageing had some influences on the microstructure, especially the pore structure.

8.1.1.1 Pore structure – porosimetry

In Fig. 8.1, N_2 adsorption isotherms from aged and not aged samples of three powders are given, the specific area and pore volume loss are also given to do the comparison. Detailed data can be found in Table 8.1. The calculation of these parameters and discussion of the methods refer to the corresponding part in Chapter 6.

Table 8.1 Pore characteristics of activated carbon powders

Sample		S_{BET} (m^2/g)	S_{DR} (m^2/g)	V_{mic} (cm^3/g)	V_{total} (cm^3/g)
A	as-received	1988	2015	0.72	0.98
	aged anode	528	496	0.18	0.35
	aged cathode	1691	1874	0.67	0.77
B	as-received	1721	1812	0.64	0.75
	aged anode	372	361	0.13	0.25
	aged cathode	1107	1195	0.42	0.55
C	as-received	2101	2182	0.77	0.92
	aged anode	888	1005	0.36	0.4
	aged cathode	1580	1732	0.62	0.69

The shape of the isotherms is consistent with that from microporous materials, which is similar to the observation of the electrodes. Since there are no other inert ingredients like conductive agents and fluoropolymer binders, both the specific area and the pore volume of pure activated carbon powders are much higher than those of electrodes, as well the change is more significant. As discussed in Chapter 3 and Chapter 6, BET, DR and DFT are three widely applied methods for the calculation of specific area and pore volume. From the results we achieved from the electrodes, the consistency of the data from these three methods is good, which can also be observed from the data presented here.

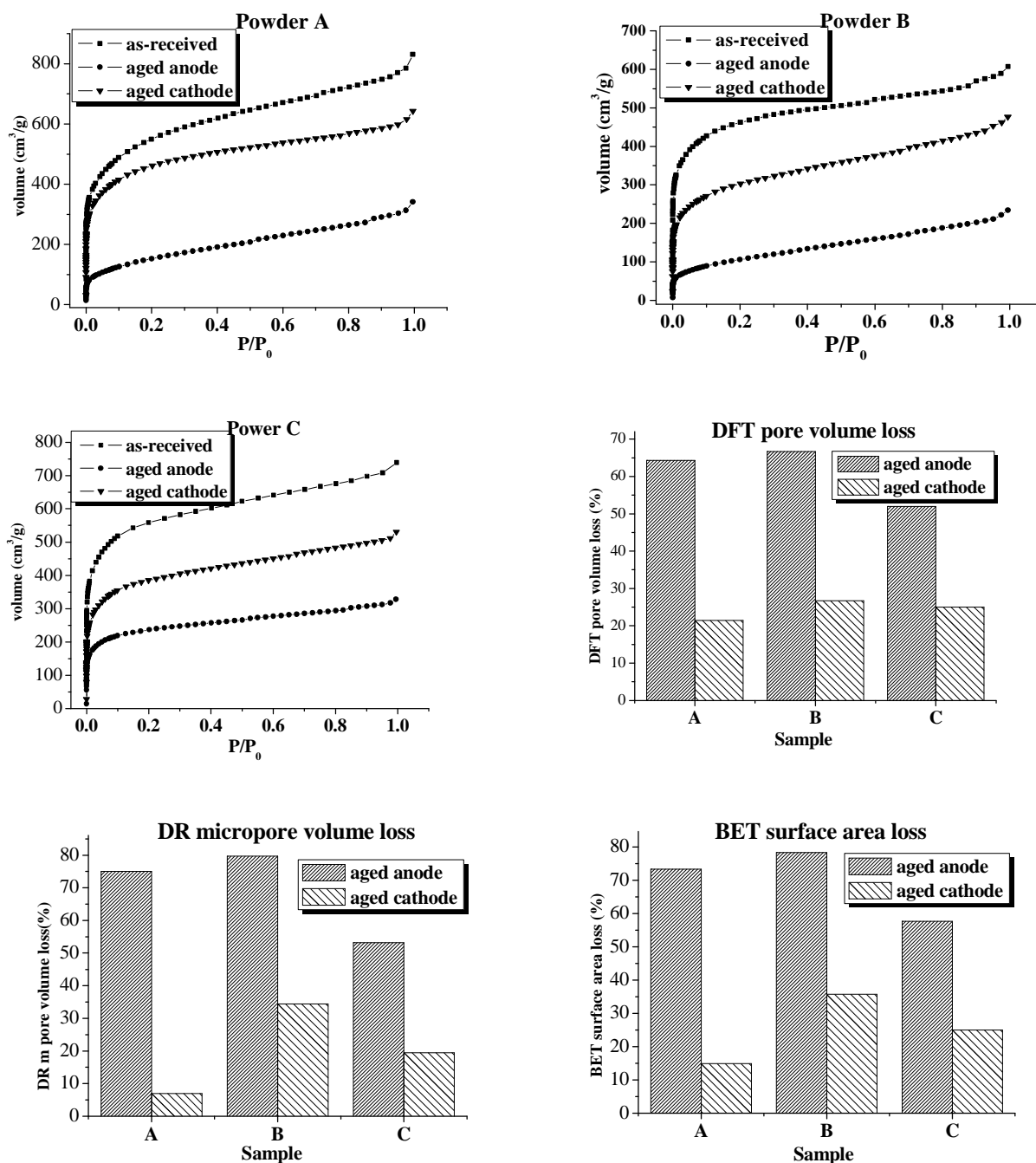


Figure 8.1 Pore characteristics comparison of powder samples

As shown in Table 8.1 and Fig. 8.1, after electrochemical ageing, all three activated carbon powder samples show asymmetric pore structure changes — aged anode powders suffer more from ageing in terms of surface area, pore volume and micropore volume than aged cathode powders, which is consistent with what observed in the electrodes of ultracapacitors.

For aged anode samples, powder B shows the highest porosity loss, and the next is powder A, while powder C suffers the least.

For aged cathode samples, generally the porosity loss is much less than age anode ones. Powder B still has the highest value. However, powder A shows higher stability on this end than powder C especially from the point of micropore volume. However, this might be due to the error from the experiment.

DFT pore size distribution histograms of the powders are calculated. As introduced in Chapter 6, this method covers the pore size range from 0.5 nm to 5 nm, which corresponds to the relative pressure from 7.7×10^{-6} to 0.7. The content of the pores in various pore size ranges can be obtained from the histogram. The results are given in Fig. 8.2. The absolute volume of the pores in various size ranges are calculated according to the pore content and the total pore volume (see Table 8.1) and given in Table 8.2.

In the histograms, there is always a sharp minimum at about 1 nm, which can be attributed to the intrinsic shortcoming of the pore model used in the DFT calculations [Jagiello04, Jagiello98, Olivier97].

If one compares the pore size distribution histogram of three as-received activated carbons, it can be seen that the content of pores in various size ranges from them does not show significant differences. All of them have high content of micropores in the size range from 0.5 to 2 nm.

Fig. 8.2a shows the pore size distribution changes after ageing for powder A. The content of pores in micropore range from 0.5 to 2 nm of aged anodes decreases strongly. The decrease of the pores in this range gives main contribution to the shrinkage of the total adsorption capacity and pore volume. The content of small mesopores from 2 to 3.2 nm does not show obvious change while the content of mesopores from 3.2 to 5 nm and even large range increases a lot, which might be an effect of the decrease of micropore content. Almost the same phenomenon can be found for powder B as shown in Fig. 8.2b.

The pore size distribution change on aged cathodes from powder A and B are not so obvious as that on aged anodes. Only the content of pores in the size range from 0.5 to 0.8 nm shows a little decrease, which might be due to the spatial confinement of cations (Et_4N^+) from electrolyte similar to that discussed in Chapter 6. The content of pores in other size ranges does not show obvious changes.

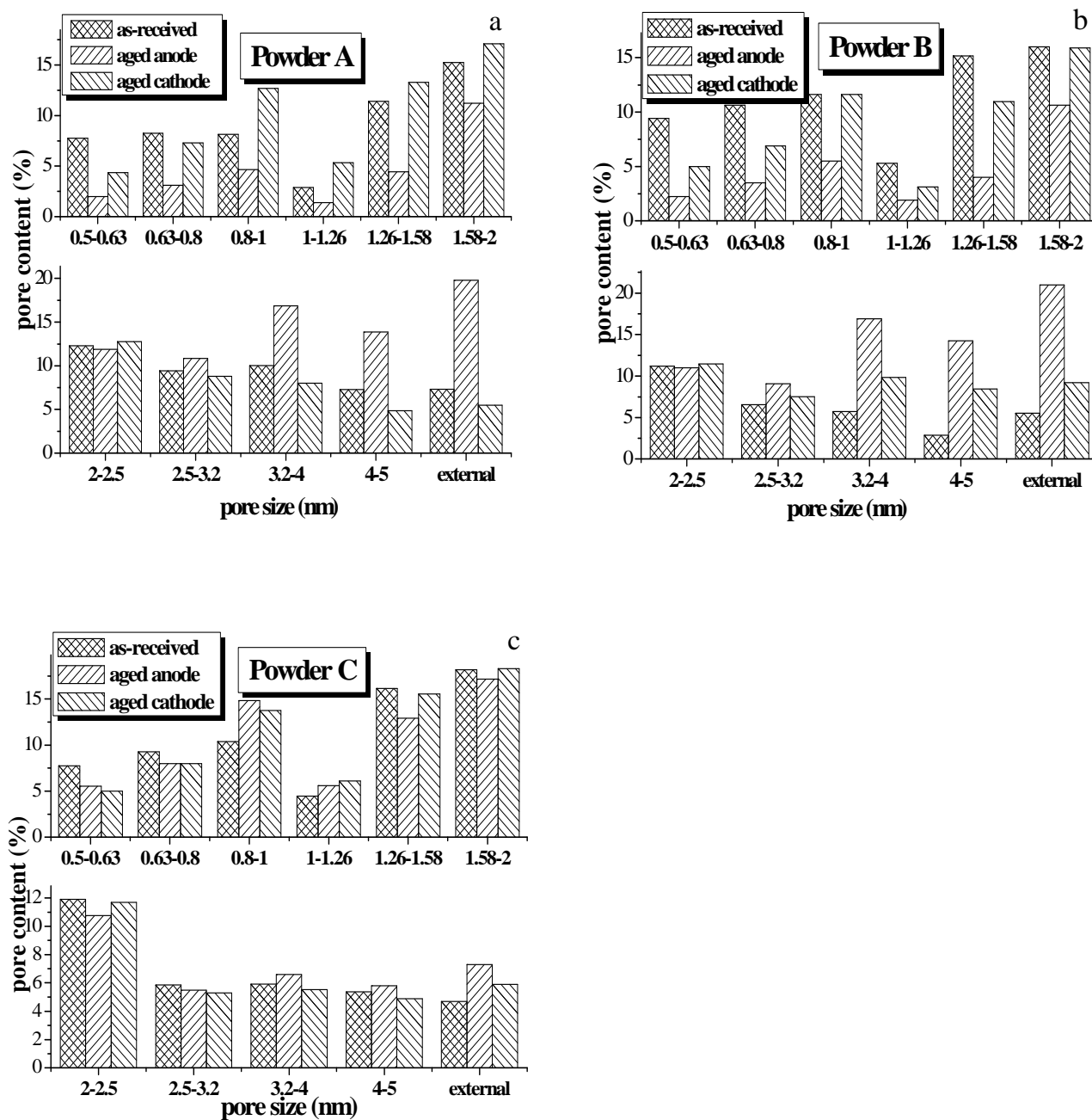


Figure 8.2 Comparison of the DFT pore size distribution histogram

While for powder C, the observation is quite different, see Fig. 8.2c. The pore size distribution does not show the asymmetric change on aged anode and aged cathode here, as well the change of the content of micropores is not so significant as powder A and B. Basically the characteristics of pore size distribution is similar to the as-received sample.

The observation that ageing influences powder A and B more than powder C might be due to the fact that the former two are from the natural precursors and the latter one is from synthetic resin precursor. As introduced in Chapter 2, the properties of activated carbons from natural precursors are not well reproduced as those from synthetic resins and expected to have less homogeneous porous structure because of their diverse natural textile. Meanwhile the chemical composition of natural precursors is more complex and difficult to control during the manufacture.

As discussed in the ageing mechanisms, the functional groups in activated carbons can be active for the anodic ageing process – some of them can promote the polymerization of the solvent and the products can block the pores. If the functionality can be controlled effectively so that less active ones exist and distribute more homogeneously, ageing process might be impeded and products distribute more homogeneously instead of accumulating to block the micropores and small mesopores, which are important for the capacity as we found from the results of electrodes.

Table 8.2 Absolute volume of the pores in various pore size ranges

	Powder A			Powder B			Powder C		
0.5-0.63	0.074	0.007	0.033	0.07	0.006	0.027	0.072	0.022	0.035
0.63-0.8	0.08	0.01	0.06	0.08	0.009	0.038	0.085	0.032	0.055
0.8-1	0.078	0.016	0.1	0.09	0.014	0.064	0.096	0.06	0.095
1-1.26	0.03	0.005	0.04	0.04	0.005	0.017	0.041	0.022	0.043
1.26-1.58	0.11	0.015	0.1	0.12	0.01	0.06	0.15	0.052	0.1
1.58-2	0.15	0.04	0.13	0.12	0.027	0.087	0.17	0.069	0.13
2-2.5	0.12	0.04	0.1	0.084	0.027	0.063	0.11	0.043	0.08
2.5-3.2	0.09	0.04	0.07	0.05	0.023	0.041	0.054	0.022	0.04
3.2-4	0.1	0.06	0.06	0.04	0.042	0.054	0.054	0.026	0.038
4-5	0.07	0.05	0.04	0.022	0.036	0.046	0.050	0.023	0.034
external	0.07	0.07	0.04	0.041	0.053	0.051	0.043	0.03	0.041

8.1.1.2 Microcrystallinity changes – Raman spectroscopy

Raman spectra from as-received powders and aged anode and aged cathode powders are collected with $\lambda_0 = 632.8$ nm (1.96 eV). The results are given in Fig. 8.3.

Detailed discussion about the characteristic Raman bands from carbonaceous materials has been given in Chapter 6. Generally, five bands can be observed for highly disordered carbon materials: G band at about 1580 cm^{-1} , which corresponds to ideal graphitic lattice stretching vibration; D_1 band at about 1350 cm^{-1} , which corresponds to the breathing vibration mode due to the broken symmetry of graphitic lattice; D_2 band at around 1620 cm^{-1} , which is normally assigned to E_{2g} symmetry vibration in surface graphene layers with disordered graphitic lattice; D_3 band at around 1500 cm^{-1} , which is also called the “valley band” and can be correlated to the amorphous carbon species (the abundance of functionality) in activated carbons; D_4 band close to 1200 cm^{-1} , which is considered to be from the disordered graphitic lattice with structure similar to polyaromatic hydrocarbon moieties [Mapelli99]. Further discussion refers to Chapter 6.

The spectra shown in Fig. 8.3 are similar to what has been observed for the electrodes in Chapter 6 and can be interpreted in terms of highly disordered graphitic structures. The first-order spectra generally exhibit two broad peaks with intensity maxima around 1316 cm^{-1} and around 1596 cm^{-1} . Above 2000 cm^{-1} , some weak bands are visible.

Raman spectra of powders A and B show that after ageing, the G band at 1590 cm^{-1} becomes weaker, which might contribute to the decrease of the content of the ideal graphitic lattice. But the change is not so obvious, and if taking the error of this method into account, the structure change is trivial. The Raman spectra from as-received powder and aged anode and aged cathode of powder C basically overlap, which might give another evidence for the higher stability of this material compared to other two powders.

The observation from Raman spectra of activated carbon powders indicates the ageing influence on microcrystallites in these powders is not significant. This might be explained by the speculation that the ageing conditions and ageing time are not sufficient to effectively change the microcrystalline structure of activated carbons.

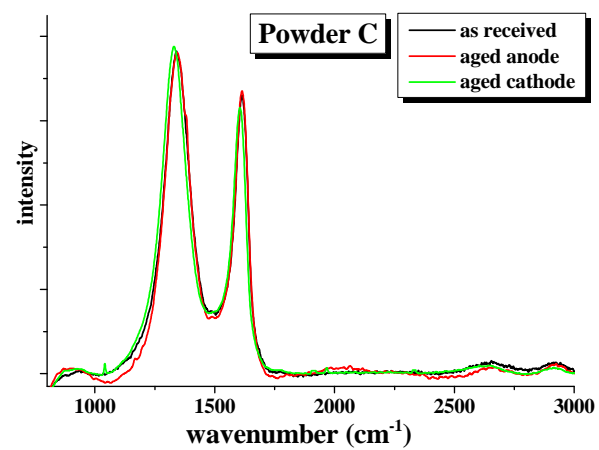
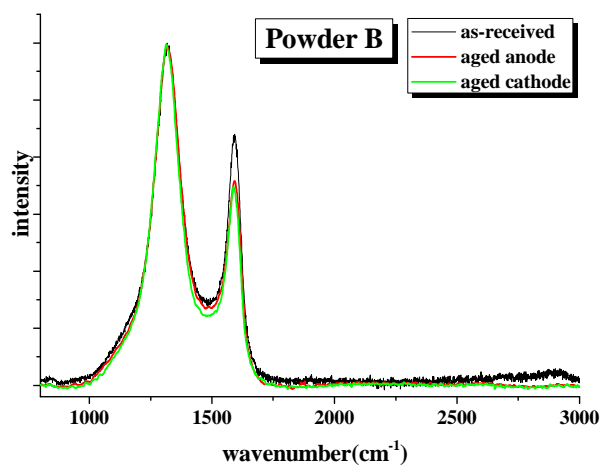
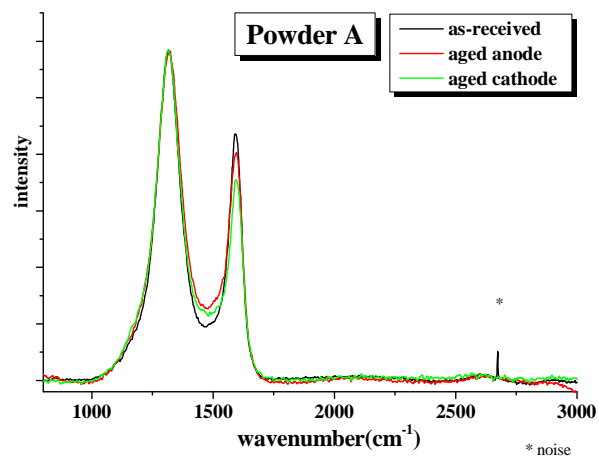


Figure 8.3 Raman spectra from as-received and aged powder samples

8.1.1.3 Summary

The results of microstructural characterization indicate that:

- All aged anode powders suffer more than aged cathode powders in terms of the specific area and pore volume.
- For the two activated carbons from natural precursors, the pore size distribution changes significantly after ageing. The micropore content of aged anode powders decreases considerably compared to as-received and aged cathode powders.
- The activated carbon from synthetic resin precursor shows better structural stability than those from natural precursors. This is indicated by less decrease of specific area and pore volume of aged anode powder, and the minor change of the pore size distribution of aged anode powder compared to the as-received powder.

8.1.2 Chemical composition changes

In Chapter 6, we summarized possible functional groups and assignments of their characteristic XPS peaks and IR bands, and applied these data to analyze the results collected from the electrodes. However, as discussed in section 6.2, the influence of the fluoropolymer binders is strong and veils some of characteristic changes of carbonaceous materials. The possible fluorination cannot be easily observed with the binders in presence.

In order to resolve this problem and to understand the chemical composition changes of carbon materials better, in this part of the work, ageing was done on individual carbonaceous materials: chemical ageing by heating the samples in solvent and electrolyte, as well as electrochemical ageing by polarizing the samples at 3 V.

With this operation, we can be sure that all the observations in this chapter are from the carbon material and electrolyte and exclude the influence of fluoropolymer binders. However, the absence of the fluoropolymer binders brings about some difficulties for the assembling and disassembling of the electrochemical cell: the quantity of the materials and the homogeneity of ageing might deviate from sample to sample (i.e., the ageing might depend on the exact location in the compressed powders). Furthermore, the mixing of the materials from anode and cathode is very difficult to prevent based on the currently used experimental set-up since we tried to assemble the powders directly in the Swagelock type lab cell without any extra container. This means there is only a separator between the anode powder and cathode powder. When the cell is disassembled, the loose powders close to the separator can

easily mix. As will be seen later in section 8.1.2.1, results from the elemental analysis are affected by this mixing seriously and appear to show results contradictory compared to those from electrodes (section 6.2.1). The results in this chapter have thus to be considered with caution

For this sake, we do not take the results in this part as quantitative analysis, rather, we only do a qualitative comparison of anodes and cathodes from each individual sample. The interpretation of the results was done with extra caution to prevent any kind of misunderstanding, e.g., one might have an impression that the content of N in aged cathode powders is unusually high and that this may involve some cathodic processes. Fortunately, results from IR are not influenced by the mixing much and show very good reproducibility. This might be due to the factor that the probing area of ATR-IR is smaller than that of XPS. The results from IR give a strong support for our announcement that some of the observations are from the effect of mixing but not real chemical or electrochemical processes, further prove the reliability for this part of work. Nevertheless, we would like to emphasize here the semiquantitative nature of this part of the work and will come back to this point again in sections 8.1.2.1 and 8.1.2.2 for a careful discussion.

8.1.2.1 Elemental analysis

Elemental analysis results of activated carbon powders are given in Table 8.3. For the as-received samples, no other elements are involved, “others” means oxygen. But for aged samples, the composition of the powder changes and “others” should include the influences from other elements like fluorine.

From the data, as-received samples have much higher carbon content compared to the electrode samples. Powder C has the highest carbon content while lowest oxygen content compared to other two. This further supports our assumption that the functionalities and composition of activated carbons from synthetic resins can be controlled better than those from natural precursors and would improve the stability of the samples. As well this can be correlated to the observation in structural changes.

Basically the structural and chemical stability of these three powders can be correlated to their purity, which is powder C > powder A > powder B. And most of the results are consistent with this order.

Table 8.3 Elemental analysis results of powder samples

Samples		C	H	N	Others
powder A	as-received	94.6	0.35	0.25	4.8
	aged anode	71.3	3	11.6	14.1
	aged cathode	80.4	2.1	6.2	11.3
powder B	as-received	91.8	0.55	0.29	7.4
	aged anode	67.7	2.7	9	20.6
	aged cathode	78.5	1.9	4.4	15.2
powder C	as-received	95.7	0.6	0.2	3.5
	aged anode	67.7	2.6	8.8	20.9
	aged cathode	83.9	2.5	4.8	8.8

The elemental analysis data from aged samples of all three powders show similar tendencies with the aged ultracapacitor electrodes (refer to Chapter 6), which is a higher N content on aged anodes. There is basically no N in as-received powders. As we discussed at the beginning of this section, the mixing affects the results of elemental analysis, a fairly high content of N is also found in aged cathode powders. However, for each sample, the content of N in aged cathode powders is much lower than in the aged anode powders. After a careful comparison with the XPS results, which will be shown in the next section and demonstrate that the chemical shifts of N 1s on aged anodes and aged cathodes are similar, we conclude that the N found on aged cathodes is from the powders mixing during cell disassembly. This means, N is practically produced solely on aged anodes.

8.1.2.2 XPS spectra of aged and not aged powders

Not aged activated carbon powders and electrochemically aged powder samples were measured with XPS. From the survey scans, only O and C are found on as-received powders, while F, O, N and C are found on aged anode and aged cathode powders and anodes show much higher N content than cathodes.

Narrow scans of F 1s, O 1s, N 1s and C 1s were collected. Data processing refers to the corresponding part in Chapter 6. The content of each element for the three

samples are given in Fig. 8.4a, the atomic concentration of various carbon moieties can be found in Fig. 8.4b. The assignment for each peak can be found in Table 8.4. The results from narrow scans of F 1s, O 1s and N 1s are summarized in Table 8.5.

As-received powders

The C 1s signal from three as-received powders are quite similar and can be deconvoluted into peaks at 284.6 eV, 285.2 ± 0.3 eV, 287 ± 0.3 eV, 288.2 ± 0.3 eV, 290 ± 0.3 eV and 291.5 ± 0.3 eV. The assignment for each peak can be found in Table 8.4 and for a detailed discussion we refer to Chapter 6. The content of graphitic carbon is the higher than that of all functional groups. And the content of C moieties at 285.2 ± 0.3 eV corresponding to the C-C bond at the edge of graphene layers and C-H species, is relatively higher than that of other species with higher binding energies. This is consistent with the findings from not aged electrodes.

O 1s peak of as-received powders can be deconvoluted into two peaks at 533.3 ± 0.3 eV and 531.5 ± 0.3 eV, which are similar to the findings in the not aged electrodes. The peak at 533.3 eV can be assigned to oxygen single bonds to sp^2 carbon (phenol, cyclic ether, lactone) or sp^3 carbon (ether, alcohol), and 531.5 eV can be assigned to oxygen double bond to carbon linked to aromatic rings (quinoid, ketone, lactone, aldehyde).

Aged anodes

As shown in Fig. 8.4, the chemical shifts of the C 1s signal from the aged anodes from the three powders are similar, while the relative abundance of each functional group shows slight differences. Generally speaking, graphitic carbon in all aged anode powders decreases significantly, especially for powder A and powder B. The amount of carbon moieties at 285.2 ± 0.3 eV, corresponding to C-C at the edge of graphene sheets, C-H and C-N species, increases on the aged anodes from powder A and powder B, but decreases a little for the aged anode from powder C.

The C 1s peaks at higher chemical shifts, corresponding to various C-O and C-N species, increases for all three powder samples, which points to the new C-N moieties formed during ageing. Combining this with the results of the binding energy of N1s at 399.3 ± 0.3 eV and at 400.6 ± 0.3 eV, one can assign these species to structures with -pyridine moieties (C=N-C), amines (C-NH₂), polyacetonitrile (-C=N-), and amides (lactams). Moreover, this is also an evidence for the formation of C-O species such as carboxylic acid, phenol and esters (including lactones), formed during ageing.

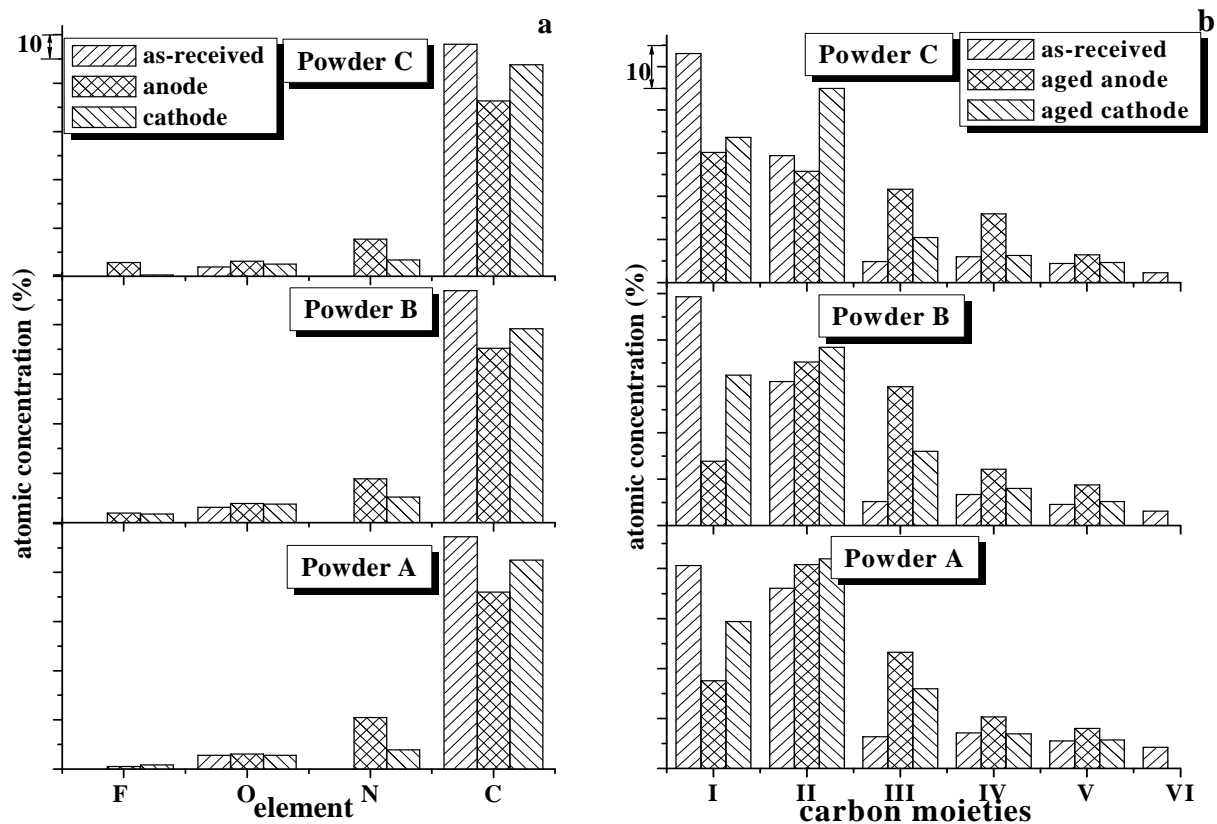


Figure 8.4 XPS results from powder samples a. atomic concentration of elements on not aged and aged powders, b. atomic concentration of various carbon moieties found on not aged and aged powders, where I = 284.6 eV, II = 285.2 ± 0.3 eV, III = 287 ± 0.3 eV, IV = 288.2 ± 0.3 eV, V = 290 ± 0.3 eV, VI = 291.5 ± 0.3 eV

Table 8.4 Binding energies of carbon moieties and assignments

	BE (eV)	Assignment
I	284.6	Graphitic C
II	285.2 ± 0.3	C-C on the edge of graphene sheets, C-H, C-N
III	287 ± 0.3	-C=O, quinone, ketone, C-OH, C-O-C, C=N-C
IV	288.2 ± 0.3	-C=O in ketone, carboxylic acid and ester, amide; C=N-C bond, CHFCH ₂
V	290 ± 0.3	O-C=O, in carboxylic acid and ester, amide; and π - π^* transition
VI	291.5 ± 0.3	Plasmon

The peak at 291.5 ± 0.3 eV which is normally assigned to the plasmon excitation, disappears on the aged anodes. This observation is consistent with that from former researchers [Proctor82, Kozlowski84, Kozlowski85, Kozlowski87]: whenever there is any significant amount of surface functionality, this feature disappears.

Table 8.5 Variation in N 1s, O 1s and F 1s of powders

	A		B		C	
	N 1s					
as-received	--	--	--	--	-	--
aged anode	399.4	400.8	399.5	400.6	399.3	400.6
aged cathode	399	400.5	399.5	400.6	399.3	400.6
	O 1s					
as-received	531.8	533.3	531.5	533.2	531.5	533.4
aged anode	531.5	533	531.8	533.4	531.5	533.5
aged cathode	531.5	533	531.8	533.1	531.5	533.5
	F 1s					
as-received	--	--	--	--	--	--
aged-node	686	688	686.3	688.6	686.3	688.3
aged cathode	686	688	686.3	688.2	686	688.2

N 1s signals can be deconvoluted into two peaks at 399.3 ± 0.3 eV and 400.6 ± 0.3 eV, as mentioned above, and the assignments refer to those given for the C 1s peaks. Since no peak in the range of 401 – 402 eV is observed, which is normally assigned to quaternary nitrogen, the influence from (crystallized and unreacted) electrolyte can be excluded, thus the samples are proven to be washed completely.

The O1s peaks from the aged anodes are quite similar, too. They do not shift much compared to the as-received samples. Combining this with the signals of C1s and N1s, the assignment for the peak at approximately 533.5 eV can be C-O-C (ethers), C-OH (phenol) and C-O single bonds in carboxylic acids or esters. The peak at 531.2 eV is assigned to C=O in carboxylic acids, esters and amides.

The F1s signal from powder samples is much weaker than that from electrodes, which is well understandable because no fluoropolymer binder is involved here. No boron signal is observed in XPS spectra, so the interference from electrolyte salts can be excluded. This peak gives a strong evidence of the fluorination of the activated carbon samples, as discussed in the mechanisms. The deconvoluted results show that the peak at about 686 eV occupies more content, which can be assigned to single F substituted carbon structures and the peak at higher binding energy 688 eV can be correlated to doubly or triply fluorinated C atoms.

Aged cathodes

The chemical shifts of the C 1s signal from the aged cathodes show differences from those of aged anodes (see Fig. 8.4). The cathodes from the three powders are quite similar. In general, the content of graphitic carbon of all aged cathodes decreases but not so much as that of aged anodes. The content of the carbon moieties with the binding energy at 285.2 ± 0.3 eV, corresponding to C-H and C-C species on the edge of graphene sheets, increases considerably on aged cathodes, which gives a strong support for the mechanism C-1 in section 7.2.

The C 1s peak at higher chemical shifts, corresponding to various C-O and C-N species increases as well, however the increase is much less than that observed on aged anodes, which is also consistent with the observation in electrodes. The peak at 291.5 ± 0.3 eV disappears as well, similar to the results for aged anodes, due to the increase of the functionality.

The other peaks of N 1s, O 1s and F 1s from aged cathodes cannot be well distinguished from those from aged anodes. We consider this as an effect of mixing the samples from anodes and cathodes. The N 1s peak is deconvoluted into two peaks for anodes and – at much lower overall intensity also for cathodes, which proved this consideration. One should also keep in mind is that this might also influence the results of C 1s, which means the difference discussed above would be even larger.

8.1.2.3 IR spectra of aged and not aged powders

Similar to the work on electrodes, attenuated total reflection infrared (ATR-IR) has been applied for the characterization of powder samples. IR spectra from aged anodes and cathodes show differences from the as-received samples and again anodes show more and larger changes than cathodes (see Fig. 8.5). However, due to the problem of sample mixing, the real difference might be even larger, i.e., some peaks on aged cathode should be even weaker.

As already discussed in Chapter 3 and Chapter 6, the sloping baseline of the spectra is characteristic of this method; the absorbance is higher at low wavenumbers than that at high wavenumbers. [Ohwaki95, Foster68, Borghesi90, Sellitti90]

As the spectra presented before, the spectra shown here are also the “original” results without additional mathematic treatment such as baseline correction (refer to section 3.2.2.2). Therefore it is possible to do semi-quantitative comparisons according to the relative intensity of each characteristic band.

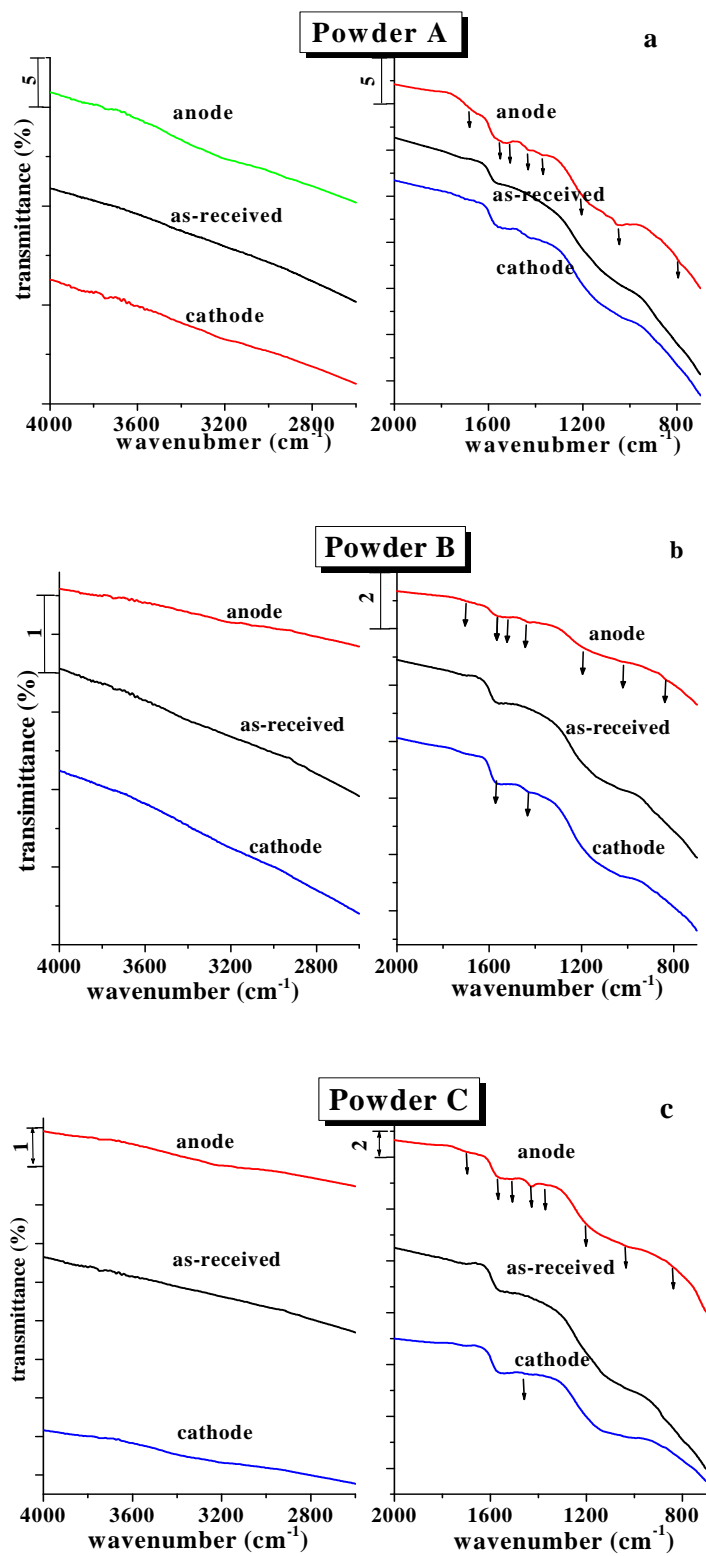


Figure 8.5 IR spectra of as-received, aged anode and aged cathode powders

All spectra from as-received powders have only two bands observable, one at around 1580 cm^{-1} and the other between 1300 and 900 cm^{-1} . Compared to the spectra from ultracapacitor electrodes, the band in the region from 1300 to 900 cm^{-1} is very broad since influence from the binder does not exist here.

The assignment for the band at 1580 cm^{-1} has been discussed in detailed in Chapter 6, and we intend to apply the interpretation of this band as the C=C stretching mode of polyaromatic systems conjugated with C=O stretching mode from quinoid functional groups [Biniak97, Figueiredo99]. The broad band between 1300 and 900 cm^{-1} can be assigned to C-O stretching mode from ether, ester, or phenol groups and C-H in-plane bending on aromatic rings.

On the aged anodes, other than the bands observed in as-received powders, several other bands can be distinguished, i.e., a broad band between 3600 and 3000 cm^{-1} , a broad band between 1750 and 1600 cm^{-1} of which the maximum is at around 1660 cm^{-1} , a strong band close to 1430 cm^{-1} , a weak band at around 1350 cm^{-1} , and a broad band between 1300 and 900 cm^{-1} with an observable increase of the relative intensity. All these can be considered to be consistent with the observation from the electrodes discussed in Chapter 6. We repeat the assignment here briefly:

The broad band between 3600 and 3000 cm^{-1} can be assigned to O-H or N-H stretching modes: bands at higher wavenumbers from 3600 to 3350 cm^{-1} are from free O-H stretching mode in phenolic or carboxylic acid structure and/or from free N-H stretching mode in primary amide or amine groups; bands in lower range from 3400 - 3200 cm^{-1} can be assigned to the overlap of the stretching vibration from associated O-H groups and associated N-H groups. At around 3100 - 3050 cm^{-1} , the stretching vibration of aromatic hydrocarbons and/or the overtone from C-N-H stretch-bend vibration in secondary amides can be found, along with the C-H stretching mode [Socrate00, Lin-Vien91]

The band between 1750 and 1600 cm^{-1} can be assigned to the overlap of the C=O stretching mode of carbonyl groups from carboxylic acids, esters (lactones), ketones and quinoids and amides, together with C=N stretching mode.

In the lower region, the band at about 1580 cm^{-1} discussed above is still observable but becomes weaker. Another discernable band at 1540 cm^{-1} can be correlated to the C-N-H stretch-bend mode in secondary amides. The band in the region of 1460 to 1400 cm^{-1} is normally attributed to the overlap of C-OH in-plane bend from

carboxylic acid and phenol groups, C-N-H bending vibration in cis-amides, C-H deformation and possibly also aromatic C=C stretching mode.

The bands at around 1370 cm^{-1} and 1340 cm^{-1} with weak intensity are considered to be from O-H deformation vibrations. C-N stretching mode in amides, and C-O stretching mode in lactone might also be found in this region.

The broad band in the region from 1300 to 900 cm^{-1} , is normally explained as C-O stretching mode from ether, ester, or phenol groups. The deformation of N-H as well C-H in-plane bending on aromatic rings can also be seen in this region.

The spectra from aged cathode powders show a high similarity with those from not aged powders. Even though the mixing might affect the results, IR results show very good identification for aged anodes and cathodes, which gives a strong evidence for our presumption that the N on aged cathode powders is from the mixing, but not produced from other cathodic processes. The observed bands are basically consistent with what found on the aged ultracapacitor cathodes, like the broad band between 3600 and 3000 cm^{-1} , the band at about 1420 cm^{-1} , as well the slightly increased band at lower wavenumbers from 1300 to 900 cm^{-1} , which can be attributed to the new oxygen functional groups like carboxylic acid, phenol and esters (lactones) formed on aged cathode powders.

The discussion above can be summarized as follows in Table 8.6.

Table 8.6 IR bands (cm^{-1}) obtained and related assignments

not-aged powders	aged anode powders	aged cathode powders	Assignment
	3600 – 3000 (br.)	3600 – 3000 (br.)	N-H, O-H str.
	3100 – 2800	3100 – 2800	C-H str. C-N-H str. o.t., OH str. (ar.)
	1750 – 1600 (br.)		C=O str. (ketone, ester and amides) , C=N str.
1580	1580	1580	C=C str. conj. C=O str.
	1540		C-N-H str.-bend
	1436	1420 (w.)	C-OH in-plane C-N-H bend, C-H def., C=C str.(ar.)
	1350 (w.)		O-H def., C-N, C-O str.
1300– 900	1300 – 900 (br.)	1300 – 900	C-O str.

Symbols used

w. weak

br. broad

str.	stretching	def.	deformation
asym.	asymmetric	sym.	symmetric
o.t.	overtone	ar.	aromatic

8.1.2.4 Summary

From the above, following conclusions are obtained:

- On as-received powders, only small amount of oxygen species exists and mainly in the form of quinoid, ketone and ether type.
- Ageing anodically produces N containing species, including pyridine moieties (-C=N-C-), amines (C-NH₂), polyacetonitrile, amides, and indeed covalently linked to graphene sheets.
- After ageing, more oxygen moieties are formed, such as phenol, carboxylic acid, esters (lactones), on both aged anode and cathode.
- XPS results indicate that more C-C bonds at the edge of graphene sheets and C-H species are formed on aged cathode powders than on aged anode powders.

8.2 Ageing effect on the conductive agents

As introduced in Chapter 4, three conductive agents are chosen for this part of work: A-B (acetylene black), K-A and K-B (ketjen black). To make the description simple and clear, they are encoded as A-B, K-A and K-B respectively. As defined in Chapter 8.1, the samples without any ageing treatment is called as-received samples, the samples collected from anodic and cathodic end are called aged anode samples and aged cathode samples, respectively. Electrochemical ageing was done by polarizing the samples at 3.0 V for a certain time period, details refers to chapter 4. Moreover, chemical ageing samples are called chem-aged sample. As described before, chemical ageing is to heat the samples in acetonitrile and electrolyte for a time period, respectively.

8.2.1 Microstructural changes

Since conductive agents mainly contribute to improve the conductivity of the electrodes, the study of microstructural changes of these materials in the present work mainly focuses on their micorcrystallinity change.

From the Raman spectra of chemically aged and electrochemically aged samples, no changes can be observed for K-A and K-B. And the Raman spectra and characteristic bands of these two materials are very similar to those of activated carbon powders.

While in the Raman spectrum of the as-received A-B, there is an obvious band at 2660 cm^{-1} (see Fig. 8.6), which is the overtone of the D_1 band at $1320\text{--}1350\text{ cm}^{-1}$ as discussed before. This band can be observed in high ordered graphite crystal but is absent in disordered graphitic materials. According to the results from other work, when C^+ ions are implanted in the high oriented pyrolytic graphite (HOPG) and the lattice structure is destroyed by sp^3 bonding, this overtone will become broad and weak. [Tan01] So the intensity of this band can be taken as a parameter for the disorder degree of the materials.

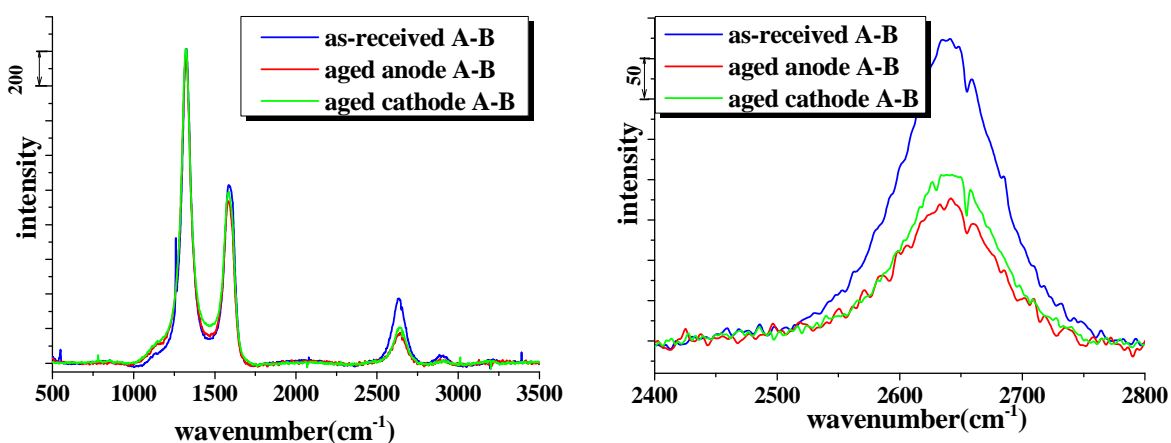


Figure 8.6 Raman spectra of as-received and aged A-B

A decrease of the band at 2660 cm^{-1} on aged anode and aged cathode is observed, as shown in Fig. 8.6, and this observation is also well reproducible for chem-aged-A-B. The attenuation of the overtone observed here can be explained as the increase of disorder in the structure through ageing. It might be due to the intercalation of small molecules or ions, thus result in the expansion of the lattice. However, current data are not enough to draw a conclusion for this. This process might also happen to activated carbons and other two carbon blacks. Nevertheless, the Raman spectra of activated carbons and other carbon blacks indicate they might have more disordered structure than A-B and the break of the order cannot be sensitively reflected.

8.2.2 Chemical composition changes

Elemental analysis and IR are carried out to characterize the as-received and aged conductive agents.

Elemental analysis results are given in the Table 8.7. If comparing these results with what we got from activated carbon powders, one can easily find the influence from ageing on the conductive agents is much less. However, only test verification is done here without reproduction, so it is possible to have errors in the results presented here. Among three samples, A-B has very high carbon content and almost no other elements, while K-A and K-B have less carbon and much more hydrogen and oxygen. The content of hydrogen in these two materials is even much higher than that found in activated carbons. After ageing, the chemical composition of A-B almost shows no difference and that of K-B has slight changes. However, the results of K-A indicate significant changes on aged anode: (1) Higher N content, although not so considerable as that observed on activated carbons; (2) The increase of the content of “others”, which is comparable to the observation from the activated carbon powders (but error possibly also influences).

Table 8.7 Elemental analysis results of conductive agents

Sample		C	H	N	Others
A-B	as-received	99	-	-	1
	aged anode	99.3	-	-	0.7
	aged cathode	99	-	-	1
K-A	as-received	93.5	0.8	0.2	4.5
	aged anode	75.5	1.5	2.3	20.7
	aged cathode	89.4	1.7	1.4	7.5
K-B	as-received	93.5	0.7	0.3	4.5
	aged anode	93.5	0.9	0.9	4.7
	aged cathode	93.3	0.9	0.7	5.1

IR spectra of three conductive agents are given in Fig. 8.7. As-received A-B shows almost no band, only one very weak and broad band between 1300 and 900 cm^{-1} can be discerned. The original chemical characteristics of K-A and K-B are similar, which shows a weak band at about 1580 cm^{-1} and a broad band between 1300 and 900 cm^{-1} . The band positions are similar to what observed on activated carbons, while the

relative intensity of the bands is lower compared to that obtained from activated carbons, which means lower content of these functional groups.

IR spectra from aged A-B and K-B indicate that no observable difference can be found from the as-received samples.

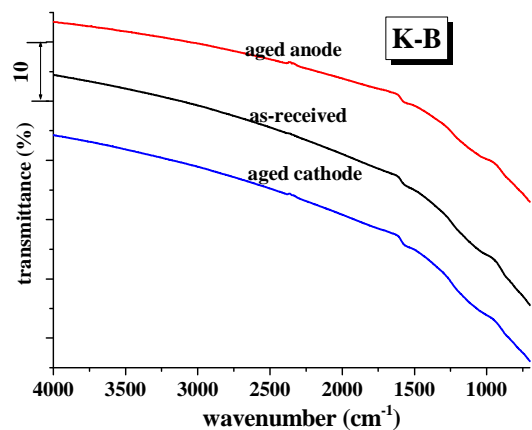
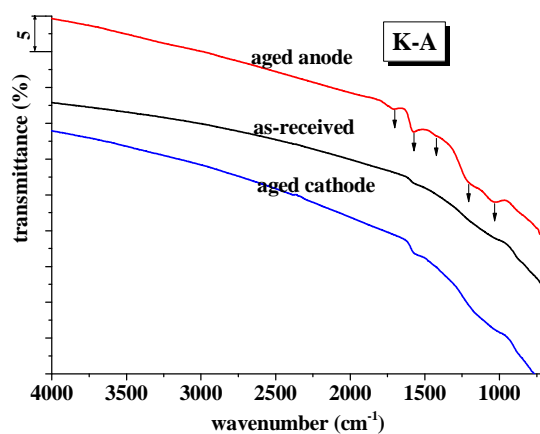
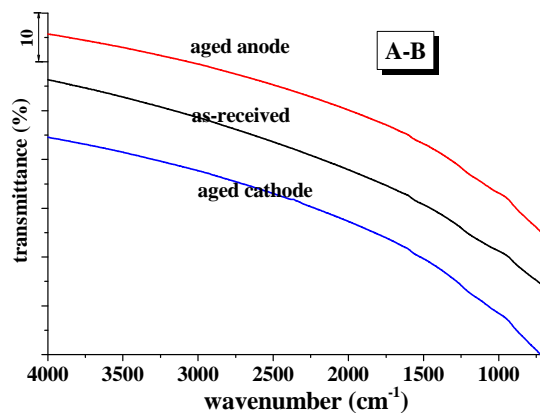


Figure 8.7 IR spectra of conductive agents

However, IR spectrum of aged anode K-A is much different from as-received K-A and aged cathode K-A. The spectra shows high similarity with the spectra from aged anode activated carbon powders: A band emerges in the region from around 1780 to 1600 cm^{-1} obviously; a discernable band at around 1430 cm^{-1} ; the intensity of the broad band between 1300 and 900 cm^{-1} can be observed to increase as well two maxima at around 1210 cm^{-1} and 1030 cm^{-1} appear. In accordance with the discussion before, these bands point to the formation of carboxylic acids, phenol, esters(lactones), amides and moieties with -C=N- stretching mode. And relative intensity of the band in aged cathode-K-A increases slightly and can be attributed to the formation of more oxygen functional groups.

The results from elemental analysis and IR of the conductive agents again give an evidence for the assumption we made before: the oxygen functional groups in the carbonaceous materials can promote the ageing processes.

8.2.3 Summary

The ageing effects on conductive agents demonstrate that:

- Acetylene black has lower oxygen content than Ketjen black.
- Ageing obvious causes the microcrystallinity changes in acetylene black, while influences Kejen blacks minor.
- Acetylene black has the best chemical stability for its high purity.

Chapter 9

Conclusions and perspectives

Ultracapacitors (UCs) with activated carbon electrodes currently have wide commercial applications, but further improvement can still be expected on the energy and power performance of the capacitors. Future progress calls for detailed information on ageing phenomena and mechanisms to figure out the essential strategies. The results from the present work can give some clues and suggestions.

In general, ageing has much stronger influences on the anode (positive end) than on the cathode (negative end).

Porosimetry results demonstrated a higher loss of the specific area and pore volume of aged anodes than aged cathodes. The relationship between the pore size distribution and the capacity loss of UCs suggests that the pores ranged from 1.26 nm to 3.2 nm in the anode are most important for the capacity of UCs, which is due to the fact that pores in this size range are essential for the mobility of ions and consequently govern the capacity of UCs. It is proposed that the ageing products on the anode will block this part of pores, thus resulting in the decrease of the capacity. Moreover, the increase of the D_3 band at approximate 1500 cm^{-1} in the Raman spectrum from aged anodes affirms the enrichment of functional groups or organic impurities. The evidence from structural changes points to the production of new chemical moieties on aged anodes.

The functionalization of carbon is further characterized and verified by XPS and IR. Phenol, carboxylic acid and esters (lactones) are found on both aged anodes and cathodes, while nitrogen from pyridine moieties ($-\text{C}=\text{N}-\text{C}-$), amines ($\text{C}-\text{NH}_2$), polyacetonitrile and amides are only found on aged anodes.

Ageing mechanisms are proposed based on above observations. Anodic polymerization of acetonitrile is a main source of relatively large molecules to block the micropores and small size mesopores. Anodic fluorination and acetamidation can happen with the existence of active species on the activated carbon surface, such as oxygen containing groups, hydrogens and radicals at the edge of graphene sheets. Compared to anodic processes, cathodic reactions are less diverse. However, gas evolution is an important side-effect of some cathodic processes, which would be stressed because it will cause the problem of internal pressure accumulation. On the

other hand, quinoid groups on the cathode can catch protons and slow down the ageing. Furthermore, non-electrochemical processes, such as Hoffman elimination and ester formation, also contribute to the ageing unavoidably.

From the mechanisms suggested, the activity of the activated carbon should be essential for the ageing, which is mainly determined by the existence of oxygen-containing functional groups. It was suggested that the high surface concentration of functional groups is not desirable because of their influence on the leakage current. [Kinoshita95] The results and mechanisms presented here demonstrate that they are harmful to the long term stability of UCs as well.

The above presumption is further confirmed by the results of the ageing test on individual components of UC electrodes. Carbon black with little oxygen shows best stability in terms of chemical composition. The activated carbon from the synthetic resin precursor with lower oxygen content shows higher structural and chemical stability than the activated carbons from natural precursors with higher oxygen content.

According to these findings, we propose some ways to improve the UC properties:

- To tailor the pore size distribution of the electrodes to optimize the capacity.

Pores in the size range from 1 to 3 nm would be preferable for the anode of UCs. This can be realized by using templates for production. However, the cost has to be taken into account.

- To decrease the content of functional groups as much as possible.

This can be done by heating the sample with the protection by inert gas. Another way is to choose purer carbon materials.

- To design UCs asymmetrically.

Anodes deteriorate faster with ageing than cathodes and they experience different ageing mechanisms. It should be feasible to use different activated carbons for the anode and cathode, or to use asymmetric recipes, e.g., to increase the quantity of the material on the anode, or to apply more stable materials only on the anode.

- To dry materials thoroughly.

Residual water is always dangerous for the non-aqueous electrochemical system. A thorough drying of the electrodes, electrolyte and other materials is important. Vacuum and heating are normally essential for the drying of electrodes, and one

should keep in mind to avoid destroying other materials in the electrodes like binders. Critical conditions of drying also mean a high cost.

Furthermore, there are several open questions from the present study.

The first one is, according to the observation and mechanism analyses in the present work, some ageing processes do not need high potential and high temperature simultaneously. The essential conditions for each reaction cannot be clarified and further work would be worthwhile.

The second one is the influences of fluoropolymer binders. The mechanisms behind some phenomena are still under investigation or call for more fundamental research, for example, the abnormal high binding energies of C 1s and F 1s observed in XPS and their disappearance after ageing.

The last question is based on the interesting observation from Ketjen blacks. They were proposed to be carbon blacks, however results from current work and the specifications offered by the suppliers showed that their properties are between those of activated carbons and carbon blacks. This kind of material can combine the advantages of high specific area of activated carbons and high conductivity of carbon blacks and thus has been proposed to be a capable candidate for the electrodes of UCs. [Takamura05] Further investigation and research on these materials may bring new findings to improve the properties of UCs.

References

- [Abotsi90] Abotsi, G.M.K. and Scaroni, A.W., *Carbon*, 28(1990): 79.
- [Adem05] Adem E., Avalos-Borja M., Bucio E., Burillo G., Castillon F.F. and Cota L., *Nucl. Instr. And Meth. B* 234(2005): 471
- [Albers92] Albers P., Deller K., Despeyroux B.M., Schaefer A. and Seibold K., *J. Catal.* 133(1992): 467
- [Alexander94] Alexander M.R. and Jones F.R., *Carbon* 32(1994): 785
- [Alexander94] Alexander M.R. and Jones F.R., *Surf. Interface Anal.* 22(1994): 230
- [Alexander95] Alexander M.R. and Jones F.R., *Carbon* 33(1995): 569
- [Alexander96] Alexander M.R. and Jones F.R., *Carbon* 34(1996): 1093
- [Alexandrou88] Alexandrou A., Cardona M. and Ploog K., *Phys. Rev. B* 38(1988): R2196
- [Al-Jishi82] Al-Jishi R and Dresselhaus S.G., *Phys. Rev, B* 26(1982): 4514
- [Arulepp04] Arulepp M., Permann L., Leis J., Perkson A., Rummaa K., Jänes A. and Lust E., *J. Power Sources* 133(2004): 320
- [Aukett92] Aukett P.N., Quirke N., Riddiford S. and Tennison S.R., *Carbon* 30(1992): 913
- [Aurbach90] Aurbach D., Youngman O. and Dan P., *Electrochim. Acta* 35(1990): 639
- [Aurbach91] Aurbach D., Daroux M., Faguy P. and Yeager E., *J. Electroanal. Chem.* 297(1991): 225
- [Aurbach99] Aurbach D. and Gofer Y., “*Nonaqueous Electrochemistry*”, Marcel Dekker, 1999
- [Azais03] Azais P., Ph. D dissertation “Causes of Ageing of Supercapacitors Based on Activated Carbon Electrodes and Organic Electrolyte”, Orléan, France, 2003
- [Backer05] Backer M.D., Berrier E., Martinon Y., Dujardin N., Dufour F., Peres J.P. and Jehoulet C., *J. Electrochem. Soc.* 152 (2005): A411
- [Bansel88] Bansel R.C., Donnet J.-B., and Stoeckli F., “*Active Carbon*”, Marcel Dekker, New York, 1988
- [Baranov87] Baranov A.V., Bekhterev A.N., Bobovich Y.S. and Petrov V.I., *Opt. Spectrosc. (USSR)* 62(1987): 613
- [Bard01] Bard A.J. and Faulkner L.A., “*Electrochemical Methods, Fundamentals and Applications*”, 2nd ed., John Wiley & Sons, 2001: 68

- [Barrett51] Barrett E.P., Joyner L.G. and Halenda P.P., *J. Am. Chem. Soc.* 73(1951):373
- [Beamson00] Beamson G. and Briggs D., “*The XPS of Polymers Database*”, SurfaceSpectra Ltd., 2000
- [Becker57] Becker H.E., *U.S. Patent 2800616*, to General Electric Co., 1957
- [Bernard79] Bernard G. and Simonet J., *J. Electroanal. Chem.* 96(1979): 249
- [Bernard82] Bernard G., Jubault M. and Simonet J., *J. Chem. Soc. Chem. Commun.* 13(1982): 759
- [Beyssac03] Beyssac O, Goffe´ B, Petitet J.P., Froigneux E., Moreau M. and Rouzaud J.N., *Spectrochim Acta Part A* 59(2003): 2267
- [Billon59/60] Billon J.P., *J. Electroanal. Chem.* 1(1959/1960): 486
- [Biniak97] Biniak S., Szymanski G., Siedlewski J. and Swiatkowski A., *Carbon* 35(1997): 1799
- [Boos70] Boos D.I., *U.S. Patent 3 536 963*, to Standard Oil, SOHIO, 1970
- [Borghesi90] Borghesi A. and Guizzetti G., in “*Handbook of Optical Constants of Solids II*”, eds. Palik E.D., Academic Press, Boston, 1990: 449
- [Brunauer38] Brunauer S., Emmett P.H. and Teller E., *J. Am. Chem. Soc.* 60(1938):309
- [Burgess71] Burgess K.A., Scott C.E. and Hess W.M., *Rubber Chem. and Tech.* 44(1971): 230
- [Byrne95] Byrne J. F. and Marsh H., Introductory overview, in “*Porosity in Carbons: Characterisation and Applications*” eds., Patrick J. W., Arnold, London 1995:1
- [Cabot05] Cabot Corporation, <http://www.cabot-corp.com/>, 2005
- [Carcknell95] Cracknell R.F., Gubbins K.E., Maddox M. and Nicholson D., *Acc. Chem. Res.* 28(1995): 281
- [Cerdeira86] Cerdeira F., Anastassakis E., Kauschke W. and Cardona M., *Phys. Rev. Lett.* 57(1986): 3209
- [Chandrasekaran90] Chandrasekaran M., Noel M. and Krishnan V., *Talanta*, 37(1990): 695
- [Cheung82] Cheung T.T.P. *J. Appl. Phys.* 53(1982): 6857
- [Ciemieki84] Ciemieki K.T. and Auborn J.J., *Proceedings of the Symposium of Lithium Batteries*, 1984
- [Clark75] Clark D.T., *Macromol. Chem. R.M.C.C.*, 12(1975): 191
- [Clark76] Clark D.T. and Thomas H.R., *J. Polym. Sci., Pol. Chem.* 14 (1976): 1671

- [Clark77] Clark D.T., *Phys. Scripta*. 16 (1977): 307
- [Clark78] Clark D.T., *J. Polym. Sci., Pol. Chem.* 16(1978); 791
- [Clark79] Clark D.T. and Dilks A., *J. Polym. Sci., Pol. Chem.* 17(1979): 957
- [Colthup90] Colthup N.B., Daly L.H. and Wiberley S.E., “*Introduction to Infrared and Raman spectroscopy*”, 3rd ed., Academic Press, San Diego, 1990
- [Conway90] Conway B.E., in “*Proc. 34th Intl. Power Sources Symposium*”, Catalog no. 90CH 2863-9, Institute of Electrical and Electronics Engineers, New York (1990): 319
- [Conway99] Conway B.E., “*Electrochemical Supercapacitors: Scientific Fundamentals and Technological Applications*”, Kluwer Academic/Plenum Publisher”, New York, 1999
- [Cotton66] Cotton F.A. and Wilkinson G., “*Advanced Inorganic Chemistry —A comprehensive Text*”, 2nd ed., Interscience, New York, 1966: 240
- [Cuesta94] Cuesta A, Dhamelincourt P, Laureyns J, Martinez-Alonso A, Tson JMD. *Carbon* 32(1994):1523
- [Dahm96] Dahm C.E. and Peters G.D., *J. Electroanal. Chem.* 402 (1996): 91
- [Dandekar98] Dandekar A, Baaker R. T. K. and Vannice M. A., *Carbon* 36(1998):1821
- [Dawson96] Dawson J.C. and Adkins C.J., *J. phys.: Condens. Matt.* 8(1996):8321
- [Desimoni90] Desimoni E., Gasella G.I., Morone A. and Salvi A.M., *Surf. Interface Anal.* 15(1990): 627
- [Dippel99] Dippel B, Jander H and Heintzenberg J. *Phys Chem Chem Phys* 1(1999): 4707
- [Dollimore64] Dollimore D. and Heal G.R., *J.Appl. Chem.* 14(1964):109
- [Donnet68] Donnet J.B., *Carbon* 6(1968):161
- [Donnet73] Donnet J.B., Rigaut M. and Fursteberg R., *Carbon* 11(1973): 153
- [Donnet76] Donnet J.B. and Voet A., “*Carbon black: Physics, Chemistry, and Elastomer Reinforcement*”, Dekker, New York, 1976
- [Dresselhaus81] Dresselhaus M.S. and Dresselhaus S.G. *Adv. Phys.* 30(1981): 290
- [Dresselhaus82] Dresselhaus M.S. and Dresselhaus S.G. “*Topics in applied physics*”, vol. 51. Springer-Verlag, Berlin 1982: 3
- [Dubinin47] Dubinin M.M. and Radushkevich L.V., *Dokl. Akad. Nauk. SSR* 55(1947): 331
- [Dubinin60] Dubinin M. M., *Chem. Rev.* 60 (1960): 235

- [Dubinin75] Dubinin, M.M., *Progress in Surface and Membrane Science* 9(1975): 1
- [Einstein05] Einstein A., *Ann. Phys.* 17(1905): 132.
- [Endo01] Endo M., Maeda T., Takeda T., Kim Y.J., Koshiba K., Hara H. and Dresselhaus M.S., *J. Electrochem. Soc.* 148(2001): A910
- [Endo02] Endo M., Kim Y.J., Ohta H., Ishii K., Inoue T., Hayashi T, Nishimura Y., Maeda T. and Dresselhaus M.S., *Carbon* 40(2002): 2613
- [Everett05] Everett M.L. and Hoflund G.B., *J. Polym. Sci. A: Polym. Chem.* 43(2005): 552
- [Everett05] Everett M.L. and Hoflund G.B., *J. Phys. Chem. B* 109(2005): 16676
- [Fabián04] Fabián S.G., Amelia M.A. and Juan M.D., *Micropor. Mesopor. Mat.* 75 (2004): 73
- [Fanning93] Fanning, P.E. and Vannice, M.A. *Carbon* 31(1993): 721
- [Figueiredo99] Figueiredo J.L., Periera M.F.R. and Freitas M.M.A., *Carbon* 37(1999): 1379
- [Finkelstein59] Finkelstein M., Petersen R.C., Ross S.D., *J. Am. Chem. Soc.* 81(1959): 2361
- [Finkelstein65] Finkelstein M., Petersen R.C., Ross S.D., *Electrochim. Acta* 19 (1965): 465
- [Fleischmann68] Fleischmann M. and Pletcher D., *Tetrahedron Lett.*, (1968): 6255
- [Fleischmann73] Fleischmann M., Mengoli G. and Pletcher D., *J. Electroanal. Chem.* 43(1973): 308
- [Foley88] Foley J.K., Korzeniewski, C. and Pons S., *Can. J. Chem.* 66(1988): 201
- [Foster68] Foster P.J. and Howarth C.R., *Carbon* 6(1968): 719
- [Franklin51] Franklin R., *Proc. R. Soc. London, Ser. A* 209 (1951): 196
- [Freeman70] Freeman E.M., Siemieniewska T., Marsh H. and Rand B., *Carbon* 8(1970):7
- [Frisch98] Frisch, M.J., Trucks, G.W., Schlegel, H.B., Scuseria, G.E., Robb, M.A., Cheeseman, J.R., Zakrzewski, V.G., Montgomery, J.A., Jr., Stratmann, R.E., Burant, J.C., apprich, S., Millam, J.M., Daniels, A.D., Kudin, K.N., Strain, M.C., Farkas, O., Tomasi, J., Barone, V., Cossi, M., Cammi, R., Mennucci, B., Pomelli, C., Adamo, C., Clifford, S., Ochterski, J., Petersson, G.A., Ayala, P.Y., Cui, Q., Morokuma, K., Malick, D.K., Rabuck, A.D., Raghavachari, K., Foresman, J.B., Cioslowski, J., Ortiz, J.V., Stefanov, B.B., Liu, G., Liashenko, A., Piskorz, P., Komaromi, I., Gomperts, R., Martin, R.L., Fox, D.J., Keith, T., Al-Laham, M.A., Peng, C.Y., Nanayakkara, A.,

- Gonzalez, C., Challacombe, M., Gill, P. M.W., Johnson, B.G., Chen, W., Wong, M.W., Andres, J.L., Head-Gordon, M., Replogle, E.S. and Pople, J.A, *Gaussian 98, revision A.6*; Gaussian,Inc.: Pittsburgh, PA, **1998**
- [Fu04] Fu R.K.Y., Mei Y.F., Wan G.J., Siu G.G., Chu P.K., Huang Y.X., Tian X.B., Yang S.Q. and Chen J.Y., *Surf. Sci.* 573(**2004**): 426
- [Fuente03] Fuente E., Menéndez J.A., Díez M.A., Suárez D. and Montes-Morán M.A., *J. Phys. Chem. B*, 107(**2003**): 6350
- [Ganesh05] Ganesh V., Pitchumani S., Lakshminarayanan V., *J. Power Sources*, in press
- [Gardner95] Gardner S.D., Singamsetty C. S. K., Booth G. L. and He G. R., *Carbon* 33(**1995**): 587-595
- [Garrell91] Garrell R.L., Herne T.M., Szafranski C.A., Diederich F., Ettl F. and Whetten R.L. *J. Am. Chem. Soc.* 113(**1991**): 6302
- [Gedye80] Gedye R.N., Sadana Y.N. and Eng. R., *J. Org. Chem.*, 45(**1980**): 3721
- [Gelius70] Gelius U., Heden P.F., Hedman J., Lindberg B.J., Manne R., Nordberg R., Nordling C. and Siegbahn K., *Phys. Scripta* 2(**1970**):70.
- [Georgakopoulos03] Georgakopoulos A., Iordanidis A., Kapina V., *Energ. Source*, 25(**2003**): 995
- [Gottesfeld87] Gottesfeld S., Redondo A., and Feldberg S.W., *J. Electrochem. Soc.* 134 (**1987**): 271
- [Gottesfeld91] Gottesfeld S., in “*Proc. First Intl. Seminar on Double-Layer Capacitors and Similar Energy Storage Devices*”, eds. Wolsky S. P. and Marincic N., Florida Educational Seminars, Boca Raton, Fla. **1991**
- [Grasseli91] Grasseli J.G., Bulkin B.J., in “*Analytical Raman Spectroscopy, Chemical Analysis Series*”, Vol. 114, J. Wiley & Sons, New York, **1991**
- [Gryglewicz05] Gryglewicz G., Machnikowski J., Lorenc-Grabowska E., Lota G. and Frackowiak E., *Electrochim. Acta* 50(**2005**): 1197
- [Gubarev91] Gubarev S.I., Ruf T., and Cardona M., *Phys. Rev. B* 43(**1991**): 1551
- [Gusev97] Gusev V.Yu., O’Brien J.A. and Seaton N.A., *Langmuir* 13(**1997**): 2815
- [Gusev97] Gusev V.Yu. and O’Brien J.A., *Langmuir* 13(**1997**): 2822
- [Hahn05] Hahn M., Koetz R., Barbieri and Gallay R., Presentation at the Conference “*Carbon for Energy Storage and Environment Protection*”, Orlean, France, **2005**

- [Hahn04] Hahn M., Barbieri O., Campana F. and Koetz R., *The 14th International Seminar on Double Layer Capacitors and Hybrid Energy Storage Devices*, Florida, **2004**
- [Hammer80] Hammer G.E., Drzal L.T., *Appl. Surf. Sci.* 4(**1980**): 340
- [Heidenrich68] Heidenreich R.D., Hess W.M. and Hess L.L., *J. Appl. Cryst.*, 1(**1968**):1
- [Hendra91] Hendra, P., Jones C., Warnes G., “*Fourier Transform Raman Spectroscopy: Instrumental and Chemical Applications*”, Prentice-Hall, Englewood Cliffs, **1991**
- [Henning66] Henning G.R., in “*Chemistry and physics of Carbon*” vol.2, eds. Walker P. L. Jr., Marcel Dekker, New York, **1966**: 1
- [HP72] Hewlett-Packard Co., *ESCA Spectrometer System 5950A Operating and Service Manual*, **1972**: 4
- [Hoflund04] Hoflund G.B. and Everett M.L., *J. Phys. Chem. B* 108(**2004**): 15721
- [Hontoria95] Hontoria-Lucas C., López-Peinado A.J., López-González J.D., Rojas-Cervantes M.L. and Martín-Aranda R. M., *Carbon* 33(**1995**): 1585
- [Hontoria-Lucas95] Hontoria-Lucas C., Lopez-Peinado A.J., Lopez-Gonzalez J.de D., Rojas-Cervantes M.L., Martin-Aranda R.M., *Carbon* 33(**1995**):1585
- [Horvath83] Horvath G. and Kawazoe K., *J. Chem. Eng. Japan*, 16(**1983**): 470
- [House71] House H.O., Feng E., and Peet N.P., *J. Org. Chem.* 35(**1971**): 2371
- [Iglesias98] Iglesias, M.J., de la Puente, G., Fuente E., Pis. J.J., *Vib. Spectrosc.* 17(**1998**): 41
- [Ishida86] Ishida H., Fukuda H., Katagiri G. and Ishitani A, *Appl. Spectrosc.* 40(**1986**): 32
- [Ishizaki81] Ishizaki C. and Marti I., *Carbon* 19(**1981**): 409
- [Jagiello04] Jagiello J. and Thommes M., *Carbon* 42 (**2004**): 1227
- [Jagiello98] Jagiello J, Tolles D. in “*Fundamentals of Adsorption*”, eds. Meunier F., Elsevier, Amsterdam, **1998**: 629
- [Jankowska83] Jankowska H. and Starostin L., *Przem. Chem.* 62(**1983**): 624
- [Jankowska85] Jankowska H., Starostin L., Pinkas, K. and Przybytniak G., *Przem. Chem.* 64(**1985**): 429
- [Jankowska91] Jankowska H., Swiatkowski A., Starostin L. and Tawrinienko-Omicynska, J., “*Adsorption of Ions on Activated Carbon*” (in Polish), PWN, Warsaw, **1991**

- [Jansen95] Jansen R.J.J. and van Bekkum H., *Carbon* 33(1995): 1021
- [Janz61] Janz G.J. and Ives D.J.G., in “*Reference Electrodes: Theory and Practice*”, eds. Ives D.J.G. and Janz G.J., Academic Press, New York, 1961: 270
- [Jawhari95] Jawhari T, Roid A, Casado J. *Carbon* 33(1995): 1561
- [Kapteijn99] Kapteijn F., Moulijn J.A., Matzner S. and Boehm H.P., *Carbon* 37(1999) : 1143
- [Kariv-Miller84] Kariv-Miller E., Nanjundiah C., Eton J. and Swenson K.E., *J. Electroanal. Chem.* 167(1984): 141
- [Kariv-Miller85] Kariv-Miller E., Lawin P.B. and Vajtner, *J. Electroanal. Chem.* 195(1985): 435
- [Kariv-Miller86] Kariv-Miller E. and Svetlicic V., *J. Electroanal. Chem.* 205(1986): 319
- [Kastner94] Kastner J., Pichler T., Kuzmany H., Curran S., Blau W., Weldon D.N., Delamesiere M., Draper S. and Zandbergen H., *Chem. Phys. Lett.* 221(1994): 53
- [Katagiri88] Katagiri G, Ishida H and Ishitani A., *Carbon* 26(1988): 565
- [Kauschke87] Kauschke W., Sood A.K., Cardona M. and Ploog K., *Phys.Rev. B* 36 (1987): 1612
- [Kawashima95] Kawashima Y. and Katagiri G., *Phys. Rev. B* 52(1995): 10053
- [Kinoshita88] Kinoshita K., “*Carbon Electrochemical and physicochemical properties*”, John Wiley and Sons, 1988
- [Kinoshita95] Kinoshita K. and Chu X., “*The electrochemical Society Proceedings*”, Vol. 95-29, 1995: 176
- [Kittel96] Kittel C., “*Introduction to Solid State Physics*”, 7th eds., John Wiley & Sons, 1996
- [Knight89] Knight D.S. and White W.B., *J Mater. Res.* 4(1989): 385
- [Kock73] Kock V.R., Miller L.L, Clark D.B., Fleischmann M., Joslin T. and Pletcher D., *Electroanal. Chem. Interf. Electrochem.*, 43(1973): 318
- [Koenig02] Koenig U., Nitschke M., Pilz M., Simon F., Arnhold C. and Werner C., *Colloid Surface B*, 25(2002): 313
- [Koetz00] Koetz R. and Carlen M., *Electrochim. Acta* 45 (2000):2483
- [Kozlowski84] Kozlowski C. and Sherwood P.M.A, *J. Chem. Soc., Faraday T.* 1 80(1984): 2099
- [Kozlowski85] Kozlowski C. and Sherwood P.M.A, *J Chem. Soc., Faraday T.* 1, 81(1985): 2745

- [Kozlowski87] Kozlowski C. and Sherwood P.M.A., *Carbon* 25(1987): 751
- [Krtil93] Krtil P., Kaven L. and Novák P., *J. Electrochem. Soc.* 140(1993): 3390
- [Laheye99] Lahaye J., Nanse G., Bagreev A. and Strelko, *Carbon* 37(1999): 585
- [Laheye99] Lahaye J., Nanse G., Fioux Ph., Bagreev A., Broshnik A., and Strelko V., *Appl. Surf. Sci.* 147(1999): 153
- [Langmuir18] Langmuir I., *J. Am. Chem. Soc.* 40 (1918): 1368
- [Lastoskie93] Lastoskie C., Gubbins K.E. and Quirke N., *J. Phys. Chem.* 97(1993): 4786
- [Leon94] Leon C. A.L. and Radovic L.R., in “*Chemistry and Physics of Carbon*”, Vol. 24, eds. Thrower P.A., Marcel Dekker, New York, 1994: 213
- [Lespade84] Lespade P, Marchand A, Couzi M. and Cruege F., *Carbon* 22(1984): 375
- [Li05] Li C.D., Yang D.Z. and He S.Y., *Nucl. Instr. And Meth. B* 234(2005): 249
- [Lin-Vien91] Lin-Vien D, Colthup N.B., Fateley W.G. and Grasselli J.G., “*The Handbook of Infrared and Raman Characteristic Frequencies of Organic Molecules*”, Academic Press, 1991
- [Lowell04] Lowell S., Shields J.E., Thomas M.A., Thommes M., “*Characterization of Porous Solids and Powders: Surface Area, Pore Size and Density*”, Kluwer Academic Publishers, 2004
- [Lozano-Castellós03] Lozano-Castelló D., Cazorla-Amorós D., Linares-Solano A., Shiraiishi S., Kurihara H. and Oya A., *Carbon* 41(2003): 1765
- [Lund01] Lund H., *Practical Problems in Electrolysis*, in “*Organic Electrochemistry*”, eds. Lund H. and Hammerich O., Marcel Dekker, 2001: 269
- [Lust02] Lust E., Nurk G., Jänes A., Arulepp M., Permann L., Nigu P. and Möller P., *Condens. Mat. Phys.* 5(2002): 307
- [Lust03] Lust E., Nurk N., Jänes A., Arulepp M., Nigu P., Möller P., Kallip S., Sammelseg V., *J. Solid State Electrochem.* 7(2003): 91
- [Lust04] Lust E., Jänes A., Arulepp M., *J. of Electroanal. Chem.* 562 (2004): 33
- [Mahy94] Mahy J., Janneskens L.W., Grabandt O., Venema A. and van Houwelingen G.D.B., *Surf. Interface Anal.* 21(1994): 1
- [Mangun01] Mangun C.L., Benak K.R., Economy J., Foster K.L. *Carbon* 39(2001): 1809
- [Mann69] Mann C.K., in “*Electroanalytic Chemistry*”, vol.3, eds. Bard A.J., Marcel Dekker, Inc., New York, 1969

- [Mann70] Mann C.K. and Barnes. K.K., “*Electrochemical reactions in nonaqueous systems*”, Dekker, New York, **1970**
- [Mapelli99] Mapelli C., Castiglioni C., Meroni E., Zerbi G., *J. Mol. Struct.* 480–481 (1999): 615
- [Marletta88] Marletta G., Oliveri C., Ferla G., and Pignataro S., *Surf. Interf. Anal.* 12(1988): 447
- [Marsh65] Marsh H. and Seimieniewska T., *Fuel* 44(1965): 355
- [Marsh67] Marsh H. and Seimieniewska T., *Fuel* 46(1967): 441
- [Marsh70] Marsh H., *Carbon* 25(1987): 49
- [Martin83] Martin R.M. et al., in “*Light Scattering in Solids I*”, eds. Cardona M., Topics in Applied Physics Vol. 8, Springer, Berlin, **1983**: 79
- [Mathews99] Matthews M.J., Pimenta M.A., Dresselhaus G., Dresselhaus M.S. and Endo M., *Phys. Rev. B* 59(1999): R6585
- [Mayell63] Mayell and Bard A.J., *J. Am. Chem. Soc.*, 85(1963): 421
- [Menachem97] Menachem C., Peled E., Burstein L., Rosenberg Y., *J. Power Sources* 68(1997): 277
- [Mernagh84] Mernagh T.P., Cooney R.P., Johnson R.A. *Carbon* 22(1984): 39
- [Midgley91] Midgley D. and Torrance K., “*Potentiometric Water Analysis*”, 2nd ed., Wiley, New York, **1991**
- [Miller86] Miller R.C., Kleinmann D.A., and Gossard A.C., *Solid State Commun.* 60(1986): 213
- [Moreno-Castilla97] Moreno-Castilla C., López-Ramón N.V., Carrasco-Marín F., *Carbon* 35(1997): 1799
- [Moyer89] Moyer D. J.D. and Wightman J.P., *Surf. Interface Anal.* 14(1989): 496
- [Mul98] Mul G., Neeft J.P.A., Kapteijn F., Moulun J.A., *Carbon* 36(1998): 1269
- [Mushiake00] Mushiake N., Inoue K, *US Patent 6134760*, **2000**
- [Nakahara95] Nakahara M. and Sanada Y., *J. Mater. Sci.* 30(1995): 4363
- [Nakajima97] Nakajima T. and Koh M., *Carbon* 35(1997): 203
- [Nakamizo74] Nakamizo M, Kammereck R and Walker P.L. Jr., *Carbon* 12(1974): 259
- [Neimark97] Neimark A.V. and Ravikovitch P.I., *Langmuir* 13 (1997): 5148
- [Neimark98] Neimark A.V., Ravikovitch P.I., Gruen M., Schueth Ferdi and Unger K.K., *J. Colloid Interf. Sci.* 207(1998):159

- [Nelson05] Nelson P. and Neat R., *Presentation at the "22nd International Battery Seminar & Exhibit, Primary & Secondary Batteries - Small Fuel Cells - Other Technologies"*, Florida, **2005**
- [Nemanich77] Nemanich, R.J., Lucovsky G. and Solin S.A., *Mater. Sci. Eng.* 31(**1977**): 157
- [Nemanich79] Nemanich R.J. and Solin S.A., *Phys. Rev. B* 20(**1979**): 392
- [Nikiel93] Nikiel L. and Jagodzinski P.W., *Carbon* 31(**1993**): 1313
- [NIST03] NIST X-ray Photoelectron Spectroscopy Database 20, Version 3.4, <http://srdata.nist.gov/XPS/>
- [Oberlin84] Oberlin A., *Carbon* 22(**1984**): 521
- [Ohwaki95] Ohwaki T. and Ishida H., *Appl. Spectrosc.* 49(**1995**): 341
- [Ohwaki95] Ohwaki T. and Ishida H., *J. Adhesion.* 52(**1995**): 167
- [Olivier95] Olivier J.P., *J. Porous Mater.* 2(**1995**): 217
- [Olivier97] Olivier, J.P., Paper presented at the 1997 AIChE Annual Meeting, Los Angeles, 1997
- [Pamula03] Pamula E and Rouxhet P.G., *Carbon* 41 (**2003**):1905
- [Papirer78] Papirer E., Guyon E. and Perol No., *Carbon* 16(**1978**): 133
- [Papirer94] Papirer E., Lacroix R., Donnet J.B., Nanse G. and Fioux P., *Carbon* 32(**1994**): 1341
- [Pittman99] Pittman Jr. C.U., Jiang W., Yue Z.R., Gardner S., Wangl L., Toghiani H., Leon Y leon C. A., *Carbon* 37(**1999**): 1797
- [Polovia97] Polovia M., Babić B., Kaluderović B and Dekanski A., *Carbon* 35(**1997**): 1047-1052
- [Pons82] Pons S. and Khoo S.B., *Electrochimica Acta*, 27(**1982**): 1161
- [Portis72] Portis L.C, Roberson, J.C. and Mann C.K., *Anal. Chem.* 44(**1972**): 294
- [Póscik98] Póscik I., Hundhausen M., Koos M., Berkese O., and Ley L., in "Proceedings of the XVI International Conference on Raman Spectroscopy", eds. Heyns A. M., Wiley-VCH, Berlin, **1998**: Ref. [12], p. 64
- [Proctor82] Proctor A. and Sherwood P.M.A, *J. Electron Spectrosc.* 27(**1982**): 39-56
- [Proctor82] Proctor A. and Sherwood P.M.A, *Surf. Interface Anal.*, 4(**1982**): 212
- [Puente98] de la Puente G., Iglesias, M.J., Fuente, E. and Pis, J.J., *J. Anal. Appl. Pyrolysis* 47(**1998**): 33
- [Qu98] Qu D., Shi H., *J. Power Sources* 74(**1998**): 99

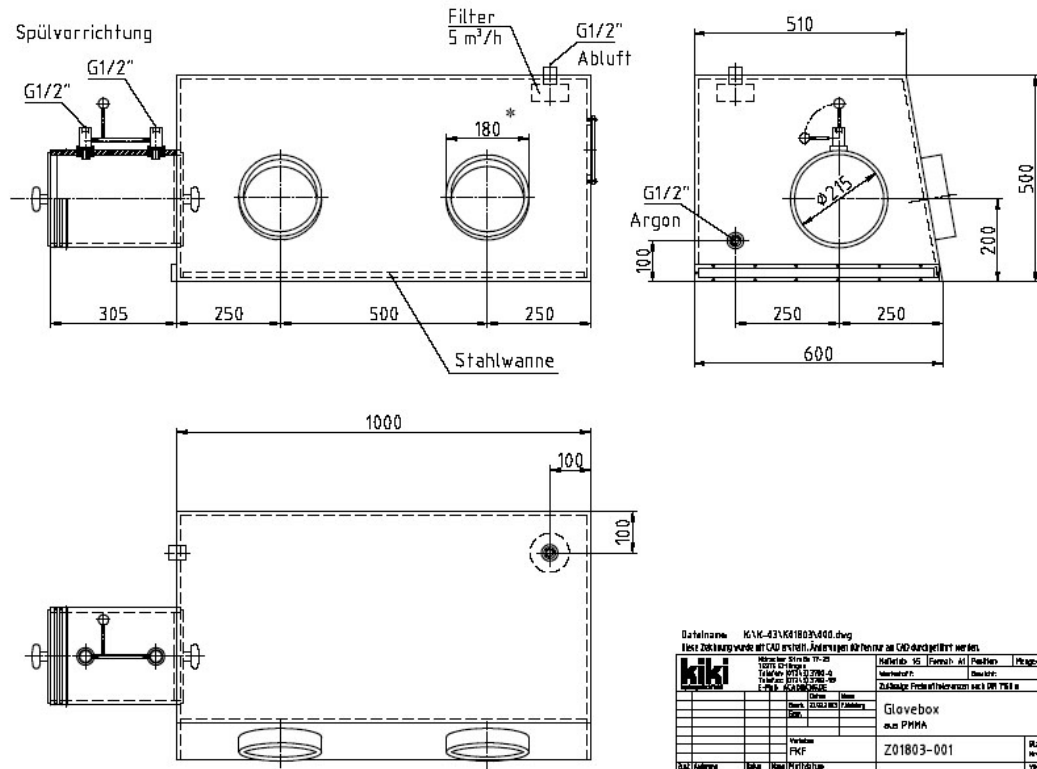
- [Quantachrome01] Quantachrome instruments, *Autosorb-1 Gas sorption system manual*, **2001**
- [Quirke96] Quirke N. and Tennison S.R.R., *Carbon* 34(**1996**): 1281
- [Radovic83] Radovic L.R., Walker P.L. Jr. and Jenkins R.G., *Fuel* 62(**1983**): 849,
- [Radovic99] Radovic L.R., in “*Surfaces of nanoparticles and porous materials*” eds. Schwarz J.A. and Contescu C.I., Marcel Dekker, New York, **1999**: 529
- [Ramsteiner87] Ramsteiner M, Wagner J. Resonant, *Appl Phys Lett.* 51(**1987**):1355
- [Ratner97] Ratner B.D. and Gastner D.G., in “*Surface Analysis The Principal Techniques*”, eds. Vickerman J.C., John Wiley & Sons, **1997**: 54
- [Robertson86] Robertson J., *Adv Phys.* 35(**1986**): 317
- [Rositani87] Rositani F., Antonucci P.L., Ciordano N. and Villari A., *Carbon* 25(**1987**): 325
- [Ross60] Ross S.D., Finkelstein M. and Petersen R.C., *J. Am. Chem. Soc.* 82 (**1960**): 1582
- [Ross70] Ross S.D., Finkelstein M., Petersen R.C., *J. Am. Chem. Soc.* 92(**1970**): 6003
- [Rousseau72] Rousseau K., Farrington G.C. and Dolphin D., *J. Org. Chem.* 37(**1972**): 3968
- [Rozhkov70] Rozhkov I.V., Bukhtiarov A.V., kuleshova N.D. and Kudryavtseu R.V., *Dokl Akad Nauk SSR* 193(**1970**): 1322, (Chem Abstr 74:70878u, 1971)
- [Rudge94] Rudge A., Davey J., Raistrick I. and Gottesfeld S., *J. Power Sources* 47(**1994**): 89
- [Rudge94] Rudge A., Raistrick I., Gottesfeld S. and Ferraris J. P., *Electrochim. Acta* 39 (**1994**): 273
- [Sadezky05] Sadezky A., Muckenhuber H., Grothe H., Niessner R. and Poeschl U., *Carbon* 43(**2005**): 1731
- [Salitra00] Salitra G., Soffer A., Eliad L., Cohen Y. and Aurbach D., *J. Electrochem. Soc.* 147(**2000**): 2486
- [Seaton89] Seaton N.A., Walton J.P.R.B. and Quirke N., *Carbon* 27(**1989**): 853
- [Sellitti90] Sellitti C., Koenig J.L. and Ishida H., *Carbon* 28(**1990**): 221
- [Shi95] Shi H., *Electrochim. Acta* 41(**1996**): 1633
- [Shin97] Shin S., Jang J., Yoon S.-H. and Mochida I., *Carbon* 35(**1997**): 1739
- [Shiraishi02] Shiraishi S., Kurihara H., Shi L., Nakayama T. and Oya A., *J. Electrochem. Soc.* 149(**2002**): A855
- [Siemens01] Siemens report CTEN1/DA1049, Erlangen, **2001**

- [Simonet77] Simonet J., Lund H., *J. Electroanal. Chem.* 75 (1977): 719
- [Simonet98] Simonet J., Astier Y., Dano C., *J. Electroanal. Chem.* 451(1998): 5
- [Sing85] Sing K.S.W, Everett D.H., Haul R.A.W., Moscou L., Pierotti R.A., Rouquerol J. and Siemieniewska T., *Pure Appl. Chem.* 57(1985): 603
- [Sinha90] Sinha K. and Menendez J., *Phys. Rev. B* 41(1990): 10845.
- [Socrates00] Socrates, G. “*Infrared Characteristic Group Frequencies*”, 3rd ed.; Wiley & Sons: Chichester, England, 2000.
- [Sood98] Sood A.K., Gupta R., Munro C.H., and Asher S.A., in “*Proceedings of the XVI International Conference on Raman Spectroscopy*”, eds. Heyns A.M., Wiley-VCH, Berlin, 1998: 62
- [Stańczyk95] Stańczyk K., Dziembaj R., Piwowarska Z. and Witkowski S., *Carbon* 33(1995): 1383
- [Starsinic83] Starsinic M., Taylor R.L., Walter P.L. Jr., Painter P.C., *carbon* 21(1983):69
- [Stoeckli90] Stoeckli H.F., *Carbon*, vol. 28(1990): 1
- [Stoehr90] Stoehr S., Boehm H.P. and Schloegl R., *Carbon* 29(1990): 707
- [Sullivan00] Sullivan, M.G., Schnyder B., Baertsch M., Alliata D., Barbero C., Inhof R., and Koetz R., *J. Electrochem. Soc.* 147(2000): 2636
- [Svetlicic86] Svetlicic V. and Kariv-Miller E., *J. Electroanal. Chem.* 209(1986): 91
- [Swenson83] Swenson K.E., Zemach D., Nanjundiah C. and Kariv-Miller E., *J. Org. Chem.* 48(1983): 1777
- [Sze01] Sze S.K., Siddique N, Sloan J.J. and Escribano R., *Atmos. Environ.* 35(2001): 561
- [Takahagi84] Takahagi T. and Ishitani A., *Carobn*, 22(1984): 43
- [Takamura05] Takamura T., “*Carbon Material in Power Sources*”, presented at the University of Ulm, Germany, Sept. 2005
- [Tamai03] Tamai H., Kouzu M., Morita M. and Yasuda H., *Electrochem. Solid-State Lett.*, 6(2003): A214
- [Tamail05] Tamai H., Kunihiro M., Morita M. and Yasuda H., *J. Mater. Sci.* 40(2005): 3703
- [Tan01] Tan P.H., Ph. D. Dissertation “*Raman Scattering of Single-Walled Carbon Nanotube and its Related Materials*”, Institute of Semiconductor, Chinese Academy of Sciences, Beijing, 2001

- [Thomas65] Thomas J.M., in “*Chemistry and Physics of Carbon*”, vol. 1, eds. Walker P. L. Jr., Marcel Dekker, New York, **1965**: 121
- [Thomsen00] Thomsen C. and Reich S., *Phy. Rev. Lett.* 85(**2000**): 5214
- [Tourillon79] Tourillon G., Lacaze P.C. and Dubois J.E., *J. Electroanal. Chem.* 100(**1979**): 247
- [Tuinstra70] Tuinstra F. and Koenig J.L., *J. Chem. Phys.* 53(**1970**):1126
- [Ue94] Ue M., Ida K. and Mori S., *J. Electrochem. Soc.* 141(**1994**): 2989
- [Valente04] Valente N.J.M., Carrott P.J.M., Ribeiro Carrott M.M.L. and Menéndez J.A. *Carbon* 42(**2004**): 1315
- [Krevelen81] Krevelen D.W., “*Coal: Typology, Chemistry, Physics, Constitution*”, Elsevier, **1981**
- [Vidano81] Vidano P.P., Fischbach D.B., Willis L.J., and Loehr T.M., *Solid State Commun.* 39(**1981**): 341.
- [Wade04] Wade L.G., Jr., “*Organic chemistry*”, 6th ed. Perrson Educaton, Inc., **2004**
- [Wagner89] Wagner J, Ramsteiner M, Wild C, Koidl P. *Phys. Rev. B* 40(**1989**):1817
- [Wang90] Wang Y., Aolsmeyer D.C. and McCreery R.L., *Chem. Mater.* 2(**1990**): 557
- [Wilson01] Wilson D.J., Williams R.L. and Pond R.C., *Surf. Interface Anal.* 31(**2001**): 385
- [Wu01] Wu S.Y., Kang E.T. and Neoh K.G., *Appl. Surf. Sci.* 174(**2001**): 296
- [Yang95] Yang, C.Q. and Simms, J.R., *Fuel* 74(**1995**), 543.
- [Yang05] Yang, Y.A., Zhu M.X., Waibel H.F. and Bittner A.M., in preparation.
- [Yoshihara02] Yoshihara K. and Tanaka A. *Surf. Interface Anal.* 33(**2002**): 252
- [Zawadzki03] Zawadzki J. and Wisniewski M., *Carbon* 41(**2003**): 2257
- [Zawadzki78] Zawadzki J., *Carbon* 16(**1978**): 491
- [Zawadzki81] Zawadzki J., *Carbon* 19(**1981**): 19
- [Zawadzki89] Zawadzki J., in “*Chemistry and Physics of Carbon*”, Vol. 21, eds. Thrower P.A., Marcel Dekker, New York, **1989**: 147
- [Zhuang94] Zhuang Q.-L., Kyotani T. and Tomita A., *Energy Fuels* 8(**1994**): 714
- [Zielke96] Zielke U., Huettinger K.J. and Hoffman W.P., *Carbon* 34(**1996**): 999
- [Zyat'kova93] Zyat'kova L.A. et.al, *Elektrokhimiza* 29(**1993**): 946

Appendix

I. Specifications of the argon flowbox



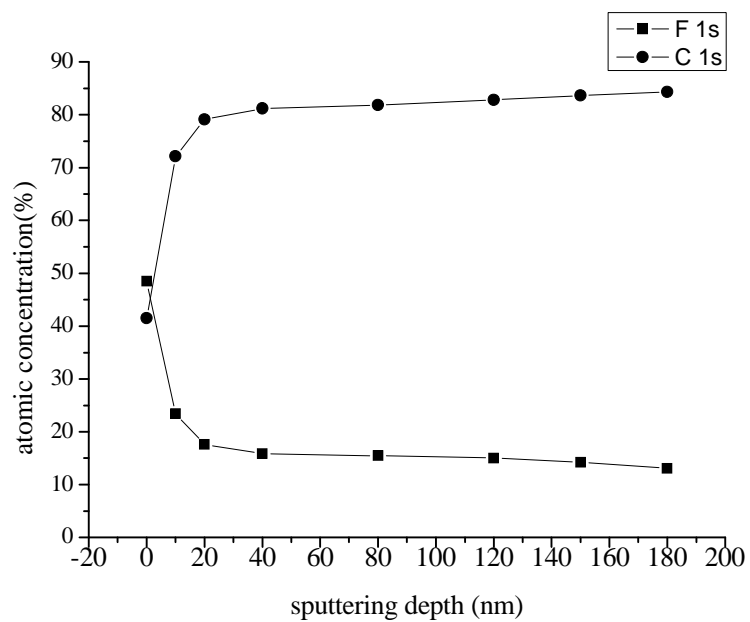
Gloves with the diameter of 17cm are applied in our case to seal the box better.

II. Measurement parameters for Infrared spectroscopy

Optics	
Source Setting	MIR Source (middle infrared)
Beamsplitter	KBr
Optical filter setting	Open
Iris Aperture (micron)	7000
Measurement channel	Front
Background measurement channel	Front
Scanner velocity	6; 10.0 kHz
Acquisition	
Low pass filter	1, 16 kHz
Acquisition mode	Double sided, forward-backward
Correlation Mode	No
FT	
Phase resolution	32
Phase correction mode	Power spectrum
Apodization Function	Blackman-Harris 3-Team
Zerofilling factor	2
Interferogram size	4740 points

III. Converging of the XPS results with sputtering

After first sputtering with the depth of approximate 10 nm, the spectra show obvious changes especially for the content of elements. The converging is observed when the sputtering depth reaches appr. 20 nm.



List of Publication:

1. Bittner A.M., Waibel H.F., **Zhu M.X.**, Kern K., Yang Y., Weber C.J.

“Neue Trockungsverfahren für elektrochemische Doppelsichtkondensatoren” (Patent, in preparation)

2. **Zhu M.X.**, Bittner A.M., Waibel H.F., Kern K., Yang Y., Weber C.J.

“Modifizierte Kohlenstoffe für elektrochemische Doppelschichtkondensatoren”, (Patent, in preparation)

Curriculum Vitae

Name: Manxi Zhu

Date of birth: Nov. 5, 1972

Nationality: People's Republic of China

1983 – 1989 High School at the First High School, Bengbu, Anhui, P. R. China

1989 – 1993 Bachelor of engineering in polymer science at Tianjin Institute of Science and Technology, Tianjin, P. R. China

1993 – 1996 Engineer at the First Institute of Project Planning & Research, Ministry of Machine Building Industry, Anhui, P. R. China

1996 – 1999 Master of engineering in applied chemistry at Beijing Institute of Technology, Beijing, P. R. China

1999 – 2001 Research assistant at the Institute of Chemistry, Chinese Academy of Science, Beijing, P. R. China

2002 – 2006 Ph. D student in the Nanoscale Science Department (Prof. Dr. K. Kern) at Max-Planck-Institute for Solid State Research, Stuttgart, Germany

Acknowledgements

I would like to acknowledge Prof. Klaus Kern for giving me the opportunity to work in his group in the Max-Planck-Institute for Solid State Research, one of the leading scientific institutions of the world, and for his continuous support in the Ph.D program. His enthusiasm for science, open mind and broad sight has made our department a perfect place to get access to various topics of science.

I acknowledge Dr. Alexander Bitter, my major advisor, for his devotion to the work, his scientific guidance and his suggestions as a mentor and a friend.

I would like to give my gratitude to more people for their contributions in this thesis, in particular:

Dr. Christoph Weber in Epcos Heidenheim, for his time and effort to support this project.

Dr. Hans-Fabian Waibel and Dr. Yongan Yang, who used to work as my collaborators in this project, for all their help for my work.

Dr. Mitsuharu Konuma and Dr. Ulrich Starke in the interface analysis service group in our institute, for the XPS training and instrument support for my research.

Dr. Shengfa Ye and Ms. B. Foertsch in the University of Stuttgart, for the help to do the elemental analysis for me.

Wolfgang Heinz and Wolfgang Stiepany in technology service group, for their help to develop the electrochemical cells and all other assemblies I need for the experiments.

Dr. Kannan Balasubramanian, Dr. Peter Wahl, Dr. Christian Ast and Christian Michaelis, for their help at the last stage of my thesis writing and other support for my work.

My dear friends in the group, for their support, collaboration and a very pleasant time in the institute.

Last but not least, I would like to give my thanks to my family, for all their love and support.